Investigation of Control Methods for Segmented Long Stator Linear Drives

Vom Fachbereich 18
Elektrotechnik und Informationstechnik
der Technischen Universität Darmstadt
zur Erlangung des akademischen Grades eines
Doktor-Ingenieurs (Dr.-Ing.)
genehmigte Dissertation

von
Dipl.-Ing. Rodrigo Benavides Oswald
geboren am 24. November 1975 in Osorno, Chile

Referent:	Prof. Dr.-Ing. Peter Mutschler
Korreferent:	Prof. Dr. -Ing. Ralph Kennel
Tag der Einreichung:	15. April 2008
Tag der mündlichen Prüfung:	21. August 2008

D17
Darmstadt 2008

Preface

This PhD thesis is the result of a 5-years work at the Department of Power Electronics and Control of Drives, Darmstadt University of Technology. Throughout my project many people contributed to my research in various ways, some directly, others indirectly related to the work presented in this thesis, but all were very helpful.

First I wish to express my gratitude to Prof. Dr.-Ing. Peter Mutschler, my supervisor and head of the Department, for his guidance, encouragement, inspiration, and valuable arrangements during this research. I greatly appreciate his patience in scrutinizing this thesis.

To Prof. Dr.-Ing. Ralph Kennel, I thank for his interest and for acting as co-advisor.

I thank the DFG Deutsche Forschungsgemeinschaft for financially supporting my projects MU 1109/12-1 and MU 1109/12-3.

I would like to thank all my colleagues at the Department for their support and comments, a good working atmosphere, and many useful discussions.

Many non-scientific issues are important for an experimental project. I appreciate the work and advice of the Department’s technical and administrative staff.

I thank the students who did their diploma theses in my topic and whose results have been used in this thesis. Even those who only found out that and why their issue did not work helped the project considerably.

Finally, I am very grateful to my wife for her encouragement, support and interest during my study and PhD time.

Darmstadt, 15.04.2008

Abstract

Nowadays, linear motors are widely used in machine tools to eliminate the gear related problems of rotative drives with lead-screw transmission. With linear motors the performance increases considerably since mechanical transmission elements are removed. This leads to a better precision, a higher acceleration and a higher speed of the moving part. Therefore, direct drives with linear motors are increasingly used in industrial applications although these solutions often need higher investment costs.

In industrial processing plants, raw materials are transferred into the production process, typically then they pass several processing stations and finally, the processed article is removed from the processing chain. In today's production plants, different equipment is used for transportation and processing materials. Advantages can be expected by using the same system of linear drives for transportation as well as for processing materials. Hence, this dissertation discusses a proposal for process-integrated material handling based on linear drives. The integration of linear drives into the production plant calls for a new view of the production process. The integrative viewpoint where a co-design of drive and plant is introduced should be developed for future applications.

To fulfill the demand of a material handling system, two alternatives are compared. The first one is based on active vehicles and passive tracks and the second one is based in passive vehicles and active tracks. Advantages and disadvantages of both alternatives are discussed, considering aspects of the power supply system as well as control and communication demands.

The control of Long Stator PM Linear Synchronous motors with passive, lightweight transportation units is investigated in detail. Hard- and software for an experimental setup is developed for a sectioned Long Stator Linear Motor and used to validate the proposed system. Finite Element tools are applied to introduce information into the control loop about section's transition and thrust force ripple. Field oriented control, direct flux control and resonant control are supported by the Finite Element information to suppress detent forces and achieve a smooth movement overall the track. A control method for soft transition between separately fed sections of the track without affecting the dynamic are implemented. Experimental results validate the proposed system and it opens a new application area for the linear drives in future.

Kurzfassung

Heutzutage werden Linearmotoren in Werkzeugmaschinen eingesetzt, um mechanische Probleme des Antriebsstranges (Kugelgewindespindel, Zahnstange, Riemen/Ritzel) auszuschließen und hohe Dynamik und Präzision zu erreichen. Linearmotoren haben den großen Vorteil, dass es keine weiteren mechanischen Übertragungselemente im Antriebsstrang gibt. Dies führt zu einer höheren Genauigkeit, Beschleunigung und Geschwindigkeit des beweglichen Teiles. Obwohl diese Antriebslösungen oftmals teurer sind, werden Direktantriebe mit Linearmotoren in industriellen Anlagen zunehmend eingesetzt.

In industriellen Verarbeitungsanlagen müssen die zu bearbeitenden Gegenstände innerhalb des Produktionsprozesses zwischen verschiedenen Bearbeitungsstationen transportiert und nach Fertigstellung aus der Verarbeitungskette ausgeschleust werden. Verarbeitungsanlagen werden oft so entworfen, dass zum Transport und zur Bearbeitung von Gegenständen unterschiedliche Einrichtungen eingesetzt werden. Vorteile sind zu erwarten, wenn für Transport und für Bearbeitung das selbe Linear- Antriebssystem verwendet wird. In der vorliegenden Arbeit werden derartige Linearantriebe untersucht. Dabei werden zwei Varianten verglichen. Die erste basiert auf aktiven Fahrzeugen und passiven Fahrwegen, die zweite auf passiven Fahrzeugen und aktiven Fahrwegen. Vorteile und Nachteile beider Alternativen werden dargestellt sowie Aspekte der Regelung und Informationsverarbeitung untersucht.

In der Arbeit wird die Steuerung und Regelung für die Variante des Langstator-PM-Linear-Synchronmotors mit passiven, leichten Transporteinheiten detailliert unersucht. Hard- und Software einer Versuchsanlage auf Basis eines segmentierten Langstator-Linear-Motors wird realisiert. Damit werden Regelungs- und Steuerverfahren untersucht und erprobt. Finite-Element-Verfahren werden eingesetzt, um Informationen zur Regelung der Übergänge zwischen den Statorabschnitten und zur Unterdrückung der Kraftwelligkeit in die Regelung einzubringen. Feldorientierte Regelung, direkte Flussregelung und resonante Regelung werden mit Hilfe des Finite Element-Modells verbessert, um eine glatte Bewegung über den ganzen Fahrweg zu erreichen.

Experimentelle Ergebnisse bestätigen das vorgeschlagene System, es öffnet ein weiteres, neues Anwendungsgebiet für Linearenantriebe.

Contents

List of symbols

a_i	: Denominator coefficients of a continuous-time transfer function
$\vec{A}$	: Magnetic vector potential
b_i	: Numerator coefficients of a continuous-time transfer function
$\vec{B}$	: Magnetic field density
d	: Damping factor
$D(s)$	: Denominator of a continuous-time transfer function
D_i	: Double ratios
e_d, e_q	: Induced phase voltages in *dq*-coordinate system
e_a, e_b, e_c	: Measured induced phase voltages
F	: Thrust force
F_{Rel}	: Reluctance force
F_M	: Mutual force
$F_{max\text{-}trans}$	: Maximal force in the transition area
$H(s)$	: Transfer function in Laplace domain
$H_{close}(s)$	: Close loop transfer function
i_a, i_b, i_c, $\vec{i}_{abc}$	: Phase currents on the motor in standard *acb*-coordinate system. Scalar/Vectorial
i_α, i_β, $\vec{i}_{\alpha\beta}$	: Phase currents oriented in stator two axes $\alpha\beta$-coordinate system. Scalar/Vectorial
i_d, i_q, $\vec{i}_{dq}$	: Phase currents oriented in rotor two axes *dq*-coordinate system. Scalar/Vectorial
$\vec{J}$	: Current density
j	: Imaginary unit
k_p	: gain of the PI controller
k_c	: Inverter gain
k_{elec}	: Gain of the current loop
k_f	: constant force-current ratio
k_Ψ	: Constant force-flux ratio
k_{r0}, k_{r1}, k_{r2}	: Resonant controller gains
L_{dd}, L_{dq}, L_{qd}, L_{qq}, $\mathbf{L_{dq}}$	: Self and mutual inductances in rotor *dq*-coordinate system. Scalar/matrix
$L_{\alpha\alpha}$, $L_{\alpha\beta}$, $L_{\beta\alpha}$, $L_{\beta\beta}$, $\mathbf{L_{\alpha\beta}}$	: Self and mutual inductances in stator $\alpha\beta$-coordinate system. Scalar/matrix
$\mathbf{L_{dq}}^{\mathbf{diff}}$	: Differential inductance in rotor *dq*-coordinate system. Matrix
$N(s)$	: Numerator of a continuous-time transfer function
P_{el}	: Electrical input power
P_{mech}	: Mechanical power
P_c	: copper loses
P_m	: Power used to store energy in the magnetic field
P_{mc}	: Number of poles of the magnet carrier
R_a, R_b, R_c, $\mathbf{R_{abc}}$	: Stator winding resistance. Scalar/Matrix

R_α, R_β, $\mathbf{R}_{\alpha\beta}$	: Stator winding resistance in stator $\alpha\beta$-coordinate system. Scalar/Matrix
R_d, R_q, $\mathbf{R}_{\mathbf{dq}}$	: Stator winding resistance in roto dq-coordinate system. Scalar/Matrix
r_i	: coefficient ratios
$\mathbf{T}_{\mathbf{abc}\rightarrow\alpha\beta}$	: Transformation matrix from abc to $\alpha\beta$ coordinate system
$\mathbf{T}_{\alpha\beta\rightarrow\mathbf{abc}}$	: Transformation matrix from $\alpha\beta$ to abc coordinate system
$\mathbf{T}_{\alpha\beta\rightarrow\mathbf{dq}}$	: Transformation matrix from $\alpha\beta$ to dq coordinate system
T_i	: Integral time of the PI controller
T_D	: Control delay time
T_{elec}	: Time constant of the current loop
T_{eq}	: Equivalent time constant
$T_{eq\text{-}flux}$	: Time constant of the flux control loop
u_a, u_b, u_c, $\vec{u}_{abc}$	: Phase voltages on the motor in standard acb-coordinate system. Scalar/Vectorial
u_α, u_β, $\vec{u}_{\alpha\beta}$	: Phase voltages oriented in stator two axes $\alpha\beta$-coordinate system. Scalar/Vectorial
u_d, u_q, $\vec{u}_{dq}$	: Phase voltages oriented in rotor two axes dq-coordinate system. Scalar/Vectorial
u_{dc}	: DC-Link voltage
v	: Speed
W_c	: Magnetic co-energy
W_m	: Magnetic energy
x	: Position
X^{FEM}	: Table obtained by FEM
X^*	: Reference value
β_m	: Electric angle
ϕ	: Magnetic flux
Ψ_a, Ψ_b, Ψ_c, $\vec{\Psi}_{abc}$	: Stator flux linkage in standard acb-coordinate system. Scalar/Vectorial
Ψ_α, Ψ_β, $\vec{\Psi}_{\alpha\beta}$	: Stator flux linkage oriented in stator two axes $\alpha\beta$-coordinate system. Scalar/Vectorial
Ψ_d, Ψ_q, $\vec{\Psi}_{dq}$	: Stator flux linkage oriented in rotor two axes dq-coordinate system. Scalar/Vectorial
$\Psi_{\alpha PM}$, $\Psi_{\beta PM}$, $\vec{\Psi}_{\alpha\beta PM}$	: Flux linkage produced by the magnets. Scalar/Vectorial
τ_p	: Pole pitch
ω_{res}	: Resonance frequency
μ_r	: Relative permeability
μ_0	: Permeability of the free space

Abbreviations

IM : Induction Motor
SM : Synchronous Motor
DCM : DC Motor
EMF : Electro motive force
MMF : Magneto Motive Force
BLDC : Brushless DC motor
LSM : Linear Synchronous Motor
LPMSM : Linear Permanent Magnet Synchronous Motor
PM : Permanent Magnet
IPM : Intelligent Power Module
HF-Signal : High Frequency Signal
FPGA : Field Programmable Gate Array
CPLD : Complex Programmable Logic Device
VCI : Vehicle Controller Interface
PCI : Peripheral Component Interconnect Bus
ISA : Industry Standard Architecture Bus
CLK : Clock
ADDR : Address / Data
WR : Write
RD : Read
RTAI : Real Time Application Interface
GUI : Graphic User Interface
FEM : Finite Element Method
2D : two dimensional

1. Introduction

1.1. Linear motors

Nowadays, linear motors are widely used in machine tools to eliminate the gear related problems of rotative drives with lead-screw transmission. With linear motors the performances increases considerably since the mechanical limitations are eliminated. This leads to a better precision, a higher acceleration and a higher speed of the moving part. Therefore, direct drives with linear motors are increasingly used in industrial applications although these solutions need often more investment costs.

Different linear motor structures and technologies exist. They can be either induction or synchronous motors with a transverse or a longitudinal flux [21][22]. Furthermore, linear motors may have several topologies. They can be either short or long stator and single or double sided. All these variants may be combined to give numerous possibilities to perform a linear motion. Typically linear motors are used for straight-line motion of a single vehicle along a limited distance. The range of distances to be traveled and the thrust force covers a wide range. The range of traveling distance starts from some millimeters for piezoelectric actuators [23] to many kilometers for maglev high-speed trains (e.g. Transrapid, Maglev) [2]. Similarly, a wide range of forces is covered by linear motors, which can reach from less than 1 N to more than 20 kN up to date.

1.1.1. Linear motor topologies

This section gives a brief classification of linear motors in order to present an overview of the various possibilities to perform a linear motion. Figure 1.1 introduces possible topologies. A main topological distinction is due to their structural geometry which can be either tubular or flat. These two geometries can be build in a long stator or in a short stator topology. For flat geometry, motors can be either single sided or assembled in opposite to constitute a double sided motor.

The definition of short stator and long stator can be described as follow:

Short stator: the electrically supplied part (primary, windings) is shorter (or equal) than the secondary part. In most of the cases, the electrically supplied part is moving. Main applications are machine tools.

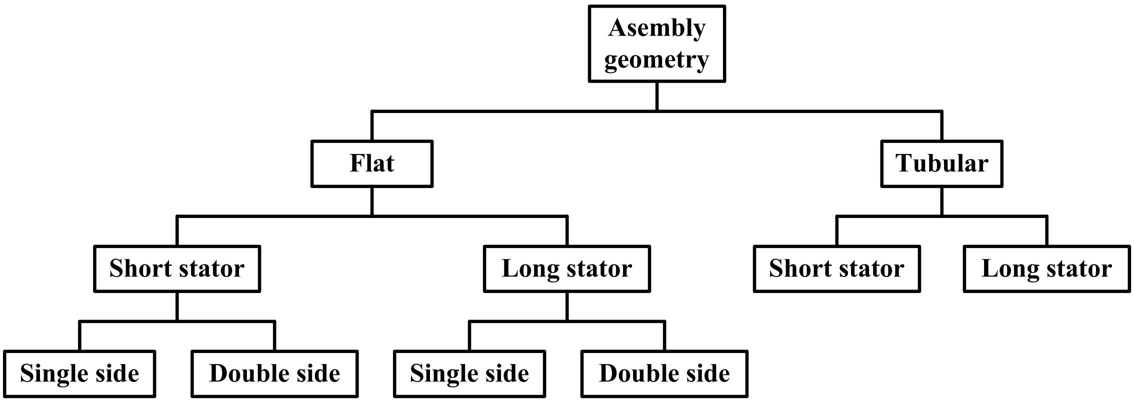

Figure 1.1: Geometric topologies of linear motors

Long stator: the length of the electrically supplied part (primary, windings) is longer than the secondary part, in most cases the secondary part is moving. Main applications are high speed trains (Transrapid, Maglev) and transportation systems.

Each linear motor finds its equivalent in rotative motion. Linear motors can be divided in to three main groups; induction motors (IM), synchronous motors (SM) including reluctance motors and DC motors (DCM), but the latter are of no interest here. The main difference between IM and SM is the excitation mode. In the IM, the winding arrangement in the primary produces a traveling field in the air gap, which induces voltages in the secondary part if there is a speed difference (slip) between the traveling field and the secondary. These voltages generate currents in the conductive plane of the secondary part. The interaction between the primary field and the secondary currents produces the force. To achieve good performances in terms of efficiency, induction motors should have a rather small air gap (about 1 mm). Moreover, compared to a linear SM with permanent magnets, this motor needs more energy to produce the same force [21].

For the SM, excitation is generated by an independent source preferably by permanent magnets for small and medium size motors. For very large SMs, electrical excitation is used too. Synchronous motors with (nearly) sinusoidal and with trapezoidal induced voltage (*EMF*) can be distinguished. The latter are called brushless DC motors (BLDC), they are fed by a nearly rectangular phase current (120° current blocks). The amplitude of the current blocks is controlled like the armature current of a DCM with brushes, and a position sensor is used for commutating currents in the stator winding, based on the position of the magnetic poles. But BLDC motors typically suffer from a higher torque ripple due to commutation, therefore the SM with (nearly) sinusoidal *EMF* is preferred for high quality motion control.

1.2. Process integrated material handling by linear drives

In industrial processing plants, articles (materials) must be transported between different locations. Raw materials are transferred into the production process, typically then they pass several processing stations and finally, the processed article is removed from the processing chain. The processing of the articles requires typically high precision as well as a high throughput throughout the manufacturing plant.

Today's material handling systems are designed to transport the articles between the individual processing stations only. Within a processing station, the article is adjusted and fastened with high precision on a mobile mechanism belonging to the processing station. In this setting, the article is processed. Subsequently, the setting is released and the article is transported to the next processing station, where similar procedures are repeated.

Hence, this dissertation discusses a proposal for process-integrated material handling based on linear drives. One key feature is, that materials are attached and fastened with high precision to the work piece carrier (vehicle) only once. Then, the materials are processed and transported in the plant without releasing frequently the high precision clamping of the work piece.

There is an increasing demand on flexible production plants, which can be adapted quickly to produce different products. In order to cover the demands of flexibility, the functional range of linear drives has to be extended in several directions:

- On a carriage way, several vehicles (work piece carriers) should be able to travel with a high degree of independency. Each vehicle has to be controlled very precisely when the vehicle operates within a processing station.
- The carriage way must allow for curves and for closed paths. In order to increase flexibility also switches shall be included in a future step.

The integration of linear drives into the production plant calls for a new view of the production process. The integrative viewpoint where a co-design of drive and plant is introduced should be developed for future applications. But to do so, tools must be developed e.g. to optimize the structure and the whole design process for such multi-vehicle, multi-track linear drive systems [1].

1.2.1. State of the art

Lorenz et al [24][25] proposed a circulating linear transport system for concatenation of machine tools. In this proposal already the possibility for curves and shunting switches were included. But the transverse flux induction machine which was designed for this project, needed rather close air gap tolerances which in turn posed high demands on the precision of the carriage way. Additionally the reactive power of the inverter had to be very large and thus the system became rather expensive.

A further project on material handling systems was developed in [26]. In this project an induction motor was used too, but with the stator (primary) on the moving part. Due to this, all the necessary electric power had to be transferred to the vehicle and the power conversion was located on the vehicle too. From this, the acceleration and speed were restricted.

A new machine design is presented in [27], where clips are moved forward by linear motors, increasing the quality, productivity and flexibility of biaxial orientation of plastic films. Simultaneous orientation technology comprising the stretching of the film in both directions at the same time results in high quality film features. Multiple passive carriers with a segmented stator is proposed.

In [3] a Linear Motor Transfer Technology is proposed for a horizontal transport of heavy goods as a link between container bridges and intermediate storage areas. A considerable saving in space, operating and service cost are achieved.

Some years ago, Translift company introduced and commercialized the “Magne-Trak”. The transport system (Figure 1.2) is based on LSM (linear SM) with passive vehicles [28]. In this approach, the vehicle moves on wheels, avoiding the effort in the mechanical guidance. Instead of it, the vehicle uses passive magnetic guidance.

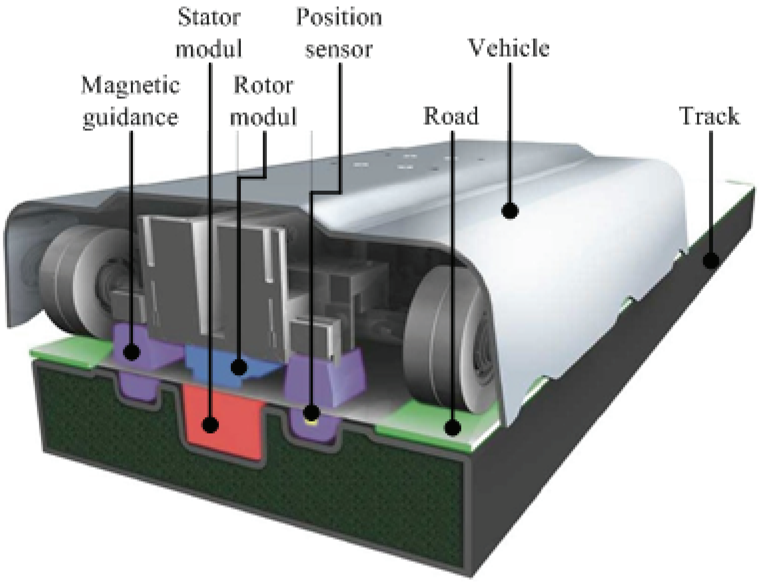

Figure 1.2: MagneTrak vehicle. Product of the company Translift.

1.2.2. Proposed system

Figure 1.3 shows a simple example of combined transportation and processing of materials with a linear drive system. In such an application, the track passes through processing stations (P1….P4). There, typically high precision positioning and high forces are necessary e.g. for machining. For high precision positioning, position sensors cannot be avoided. But outside of the processing stations, typically a lower precision in positioning is sufficient. In these parts of the track, motion control without using sensors for speed or position should be realized.

In order to increase flexibility, in a future step also switches “S” may be included. The vehicles V1 to V5 have to fulfill the following demands:

- high acceleration
- precise positioning when operating within a processing station
- high dynamic load stiffness

To fulfill the demand of the proposed system in Figure 1.3, two alternatives are compared. The first one is based on active vehicles and passive tracks and the second one is based on passive vehicles and active tracks. Advantages and disadvantages of both alternatives are discussed in detail in the next chapter, considering aspects of the power supply system and control and communication demands. An experimental setup is built based on an active track and used to validate the proposed system and it opens a new application area for the linear drives in the future [47].

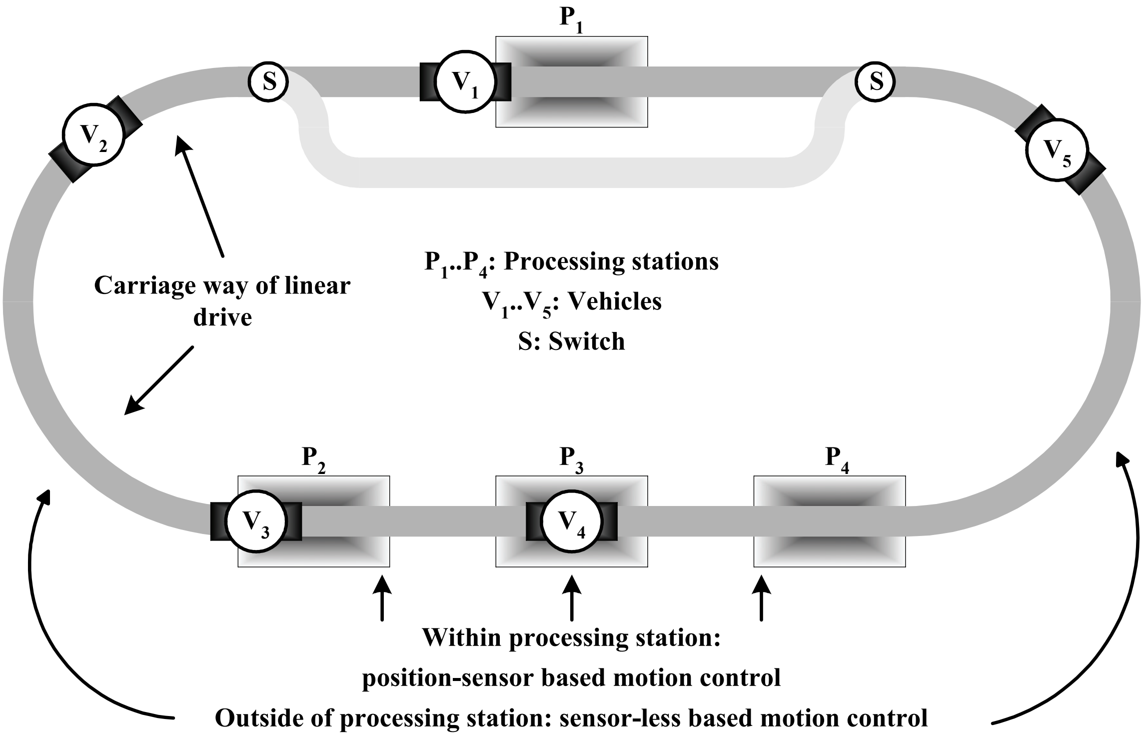

Figure 1.3: Simple example of proposed linear drive system for combined transportation and processing of materials.

2. Linear drives topologies for material handling

The vehicles for the proposed system in Figure 1.3 must fulfill some characteristics. Inside of the processing stations, high precision positioning (some µm) as well as high thrust force is necessary. Under these conditions, a Linear Permanent Magnet Synchronous Motor (LPMSM) offers the best solution, with high thrust force density [1]. Outside of the processing station sensor-less operation is desired to avoid expensive position sensors. But sensor-less operation is not the topic of this thesis.

2.1. Active vehicle and passive track

Active vehicles have the main disadvantage that the energy must be transferred to the moving part. In machine tool applications this is done typically by a drag-chain, where the converter and the controller are in a stationary cabinet. The motor is fed by a cable in the drag-chain, but also the cable for the feedback of the position sensor uses the drag chain. For water cooled motors, flexible tubes are mounted too. Drag-chains are not suitable for the proposed system of Figure 1.3, where vehicles must move freely along a closed path.

An alternative solution to the limitation of the drag-chain is to mount the power converter and the controller on board of the vehicle and feed it by a contact-less energy transmission system [29]. Figure 2.1 shows two vehicles fed by a (big) middle frequency converter. This topology has some interesting advantages, but also drawbacks, in comparison with passive vehicles. The number of converters and control units necessary is equal to the number of vehicles plus a (big) converter for the contact-less energy transmission. Additionally, the position sensing is completely done on board of the vehicle, and only the position reference value should be transmitted to the vehicle controller. To coordinate the motion of all the vehicles in the system, a stationary coordinating controller that generates the position references for all the vehicles is necessary too. A wire-less communication system can be used to fulfill this demand of communication between vehicles and stationary controller.

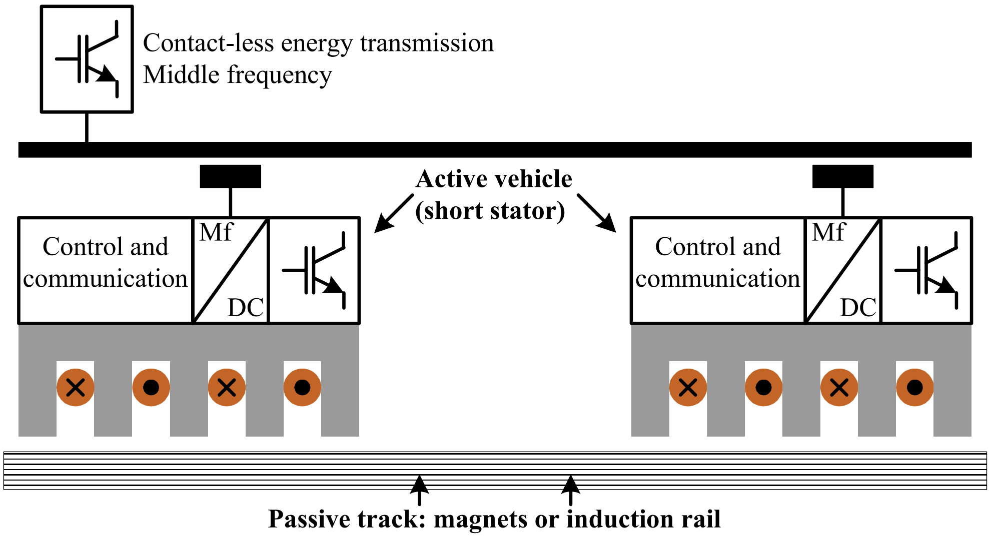

Figure 2.1: Active vehicles with contact-less energy transmission and passive track.

If along some segments of the track only a low thrust force is necessary, then the operation of the motor can be changed from synchronous machine to induction machine, saving the magnets along the low-force segments of the track.

The limitations of this topology are given mainly by the power supply system and the high weight of the vehicle, which reduce the dynamics (acceleration). Energy storage (super cap) on-board can improve this disadvantage, but this increases the weight, volume and the complexity.

The solution of active vehicles can be applied for systems with low acceleration demand and low density of vehicles [29].

2.2. Passive vehicle and active track

Long stator PM linear synchronous motor with passive, lightweight transportation units, which do not need any energy or information transferred to the vehicles, offers interesting advantages for the proposed system. Due to the permanent magnet excitation, relative large air gaps are acceptable for the carriageway, reducing the effort for the mechanical guidance. For several reasons the long stator must be divided into segments, each of them will be fed individually:

- In order to enable individual control of the vehicle motion, each vehicle must reside on an individually fed segment of the carriageway.

- The higher the number and the desired independence in motion of the individual vehicles, the more independently fed stator segments and inverters are necessary.
- Long segments require high reactive power. In order to keep the reactive power low, shorter segments are preferred. Stator segments not carrying a vehicle will be switched off.

For the individual control of vehicles there are mainly two alternatives to feed the segments:

- A segment-switch-gear connects an inverter with a stator segment which is occupied by a vehicle. This is an attempt to reduce the number of inverters. The minimum number of inverters is twice the number of vehicles. But with such a low number of inverters, many restrictions concerning the independency of motion have to be accepted. Two inverters are necessary to feed one vehicle during the transition between two consecutive segments to achieve a smooth motion and force. In the worst case all vehicles may be in a transition state simultaneously.
- Each segment will be fed by a dedicated inverter. Again, two inverters must feed one vehicle when it moves between two segments.

Both alternatives to supply the track have advantages and drawbacks from the point of view of the control and communication effort, and this will be discussed in the next section.

Figure 2.2 shows five segments of a long stator linear motor and two vehicles on it. The vehicle controller requires a high bandwidth communication channel with both inverters that feed the segment which is occupied by the same vehicle. In addition, the

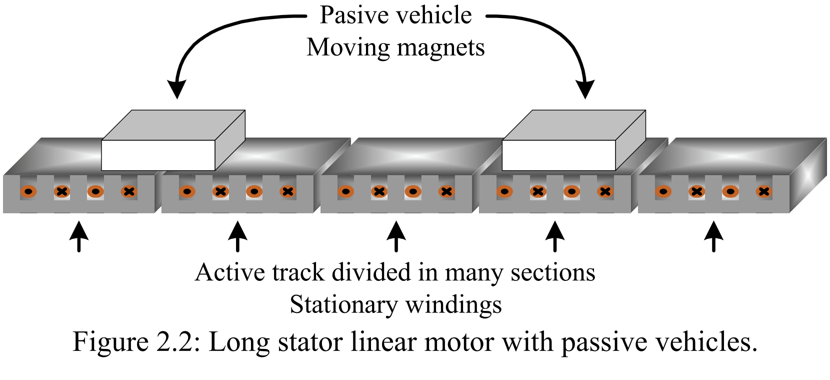

Figure 2.2: Long stator linear motor with passive vehicles.

controller has to determine which segment to feed and command the segment-switch-gear (if any). The position measurement is complex because the vehicle is completely passive, and -when using an optical position sensing system- only the scale can be mounted at the vehicle. For position acquisition, stationary sensor processing electronic is used, but depending on the length to be measured, this will become complex. A superimposed controller is necessary to coordinate the motion in the entire system.

Table I shows a comparison between active and passive vehicle topologies. The application will determine which topology should be used. For high dynamics requirements, only passive vehicles are possible, independent of the drawbacks in communication and control effort.

Table I: Active and passive vehicle topologies comparison.

	Active vehicle		Passive vehicle	
	Advantages	Drawbacks	Advantages	Drawbacks
Power supply	✓ One inverter per vehicle ✓ Simple position measurement ✓ Low cost track	× Limited by contact-less energy transmission × Heavy vehicles	✓ Light vehicles	× At least 2 inverter per vehicle × Expensive active track
Control	✓ One controller per vehicle ✓ Easy position measurement	× Low dynamic	✓ One controller per vehicle (depend on topology) ✓ High dynamic	× One controller per inverter (depend of topology) × Complex position measurement
Communication	✓ Controller→ inverter: easy	× Controller→Superimposed motion controller complex		× High bandwidth demand in all levels

2.2.1. Segment-switch-gear (multiplexed inverters)

Strategies for the control of segment-switch-gear were developed mainly for high speed maglev transportation systems. A well known maglev transportation system is the Transrapid, which has found it first application in Shanghai. The Transrapid is made up by two parallel long stator linear motors which uses an active track with segments from 300m to 2080m long. The length of the segments depends of the thrust force demand in the respective position (acceleration, constant speed, uphill, downhill, etc). Three strategies were developed to switch the inverters and the respective segments [1][2]:

- Leap-frog strategy

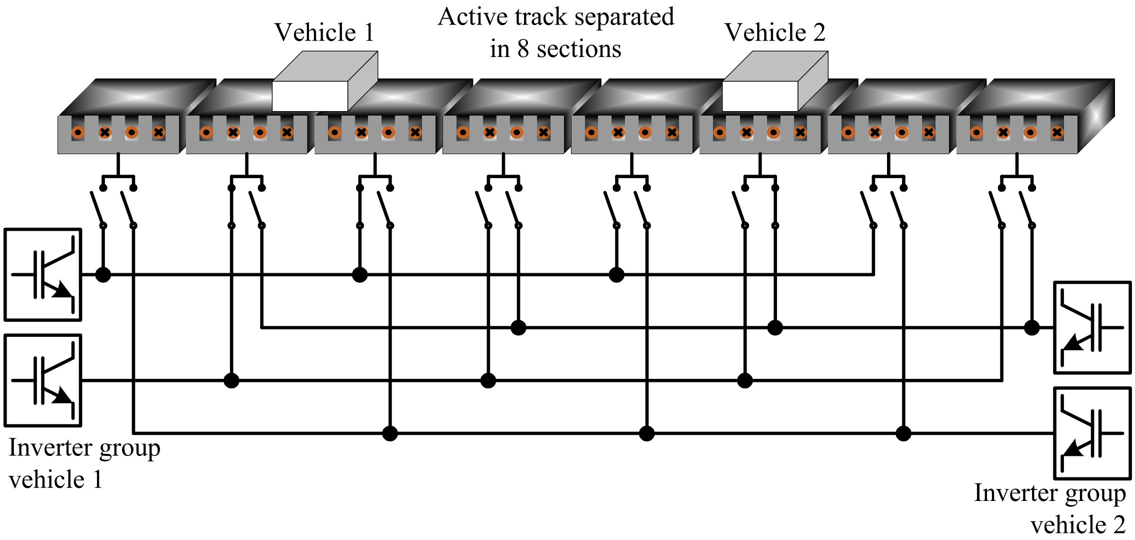

Figure 2.3: Long stator linear motor: 2 vehicles, 8 segments, 2 inverters per vehicle.

- Two step strategy
- Three step strategy

The requirements for industrial material handling are quite different, especially in acceleration and thrust force profile. One of the main demands is a smooth thrust force along the whole carriage way. Switching between segments must be done in such a way that it does not affect the dynamics. Therefore, before a vehicle enters into a new segment, the segment must be fed with the same current as the previous one. The force-current-position dependence will determine the control strategy to be used to achieve a smooth motion.

In the simple example of Figure 2.3 with 2 vehicles, 4 inverters and 8 segments, a lot of restrictions can be seen concerning the independent motion of the two vehicles. A higher degree of independency is achieved, if more segments, inverters and switches are added, but complexity and cost will grow tremendously. Mechanical switches have a limited life time and switching speed. The realization of electronic switches is a problem as well. It is questionable weather anti-parallel thyristors can withstand the high *dv*/*dt* generated by the IGBTs in the inverters. Alternatively the multiplexer may use 2 IGBTs per phase. But this would end up with a much higher number of IGBTs than using dedicated inverters [1][29].

From the control and information point of view, for multiplexed inverters the vehicle controller must command always the same two inverters and the segment-switch-gear. The major effort is made by the position measurement.

2.2.2. Dedicated inverters

Passive, lightweight vehicles, using an active track with one inverter per segment, are an interesting solution in applications where very high acceleration and dynamic are mandatory. To reduce reactive power and loses, only those segments, where a vehicle is located are energized, all other inverters are turned off.

For small segments, the cost of the inverter can be drastically reduced using IPM's (Intelligent Power Modules) and shunt resistance for the current measurement [30]. Figure 2.4 shows a system with 8 inverters, 8 segments and 2 vehicles.

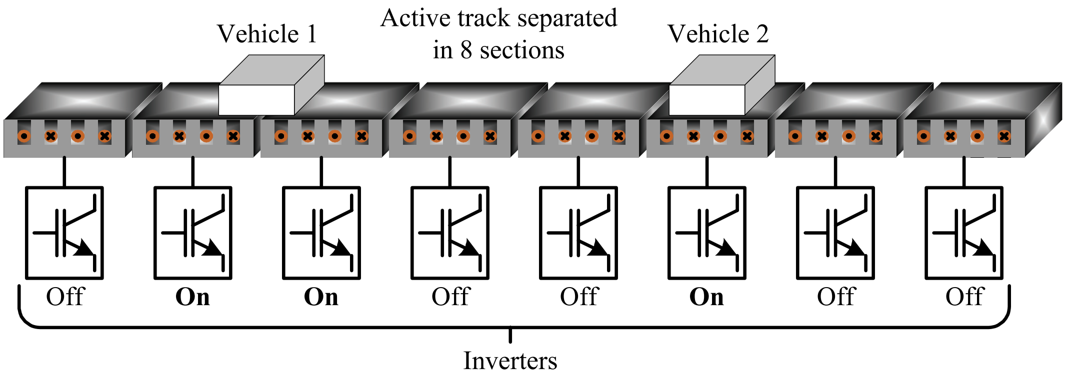

Figure 2.4: Dedicated inverter topology: 8 inverters, 8 segments, 2 vehicles

For dedicated inverters there are two alternatives for the physical distribution of the components. The inverters can be placed in a cabinet, together with all auxiliary equipment. In this case, each inverter must be wired to the respective segment by a shielded motor cable. This results in an expensive wiring with some hundred meters of cable for a large system (more as 20 segments). The second alternative is to distribute the inverters along the track [29]. Then, a DC-Link distribution along the segments is enough to feed the system. This reduces the wiring and cost, but other aspects like the control and especially communication structure must be considered.

Table II shows a comparison between multiplexed and dedicated inverters to feed the segments of a linear motor for material handling.

Table II: Multiplexed and dedicated inverters, Advantages and drawbacks.

	Multiplexed inverters	Dedicated inverters
Advantages	✓ Two inverters per vehicle	✕ High freedom of mobility ✕ High acceleration and dynamic ✕ Good for high density of vehicles
Drawbacks	✓ Expensive electronic segment-switch-gear ✓ Dynamic limited by the segment-switch-gear ✓ Low density of vehicles possible ✓ Limited lifetime with mechanical switches ✓ Electronic switches need more power semiconductors than Dedicated Inverters	✕ High number of inverters necessary ✕ Complex communication and control structure

2.3. Control and communication layer

Typically, the number of vehicles may be in the range of 30% of the number of stator-segments. This is a motivation to assign one controller to one vehicle, in order to have the lowest number of controllers. Actually, field oriented control for 2 inverters and sensor-less positioning using HF-signal injection demands a high computing power. Therefore, the cost for a controller can be higher than a IPM-based inverter.

We have to distinguish between two aspects: One controller for each vehicle and alternatively one controller for each stator segment. The first alternative will be discussed in section “Centralized vehicle controller” and the second one in section “Distributed vehicle controller”

2.3.1. Centralized vehicle controller

In this alternative, each vehicle is assigned to one controller, i.e. a vehicle controller. From the control point of view, the vehicle controller must receive the feedback information for the current control loop from the inverter which is feeding the vehicle, execute the control algorithm, and send the modulation information back to that inverter. To reach the dynamic quality of a servo-drive, the sampling time for the control loop should be smaller than 125µs [14]. In case that the data exchange takes 10% of the control cycle time, then it is possible to handle up to 10 vehicle controllers using the same physical communication bus. A reduction of the time necessary for data exchange implies an increased bandwidth of the communication channel. The bandwidth will limit the maximum number of vehicle controllers that can be handled.

A communication system with multiple star topologies, i.e. a physical connection between the vehicle controller and each inverter is not applicable because then the inverters must have as many communication interfaces as vehicles in the system, and the vehicle controller as many interfaces as inverters.

Figure 2.5 shows a system for 2 vehicles, 8 segments and 8 inverters. The “vehicle coordination” block receives the position of both vehicles and generates the desired position reference values. Then the “vehicle controller” executes all control algorithms. Physically, the “vehicle controllers” shown in Figure 2.5 are realized in one PC or several PCs, which are equipped with an FPGA-based Vehicle Controller Interface (VCI) board serving for time critical communication between vehicle controllers and inverters via the Inverter Bus [31].

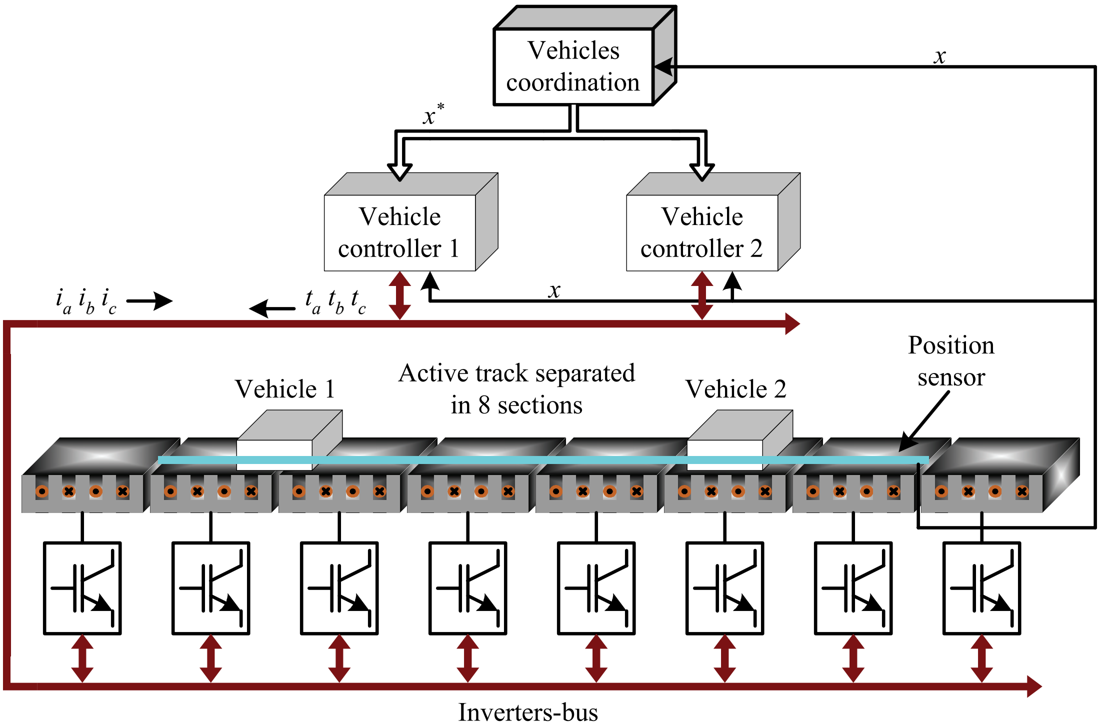

Figure 2.5: Structure with one controller per vehicle. Communication structure between inverters and vehicle controller redefined as “Inverter-Bus”.

2.3.1.1. Inverter-Bus

The topology with one controller per vehicle demands a high bandwidth communication system. A special Inverter Bus was developed to fulfill the demand for up to 10 vehicles with a cycle time of 100µs, operating on a carriageway consisting of up to 32 members (inverters + vehicle controllers). The Inverter Bus is an extension of a masterslave system, as there are two levels of masters. There is one bus master, which calls sequentially the vehicle controllers. Then, the called vehicle controller acquires master functionality and starts to communicate with (one or two) inverters where the vehicle presently is traveling. The sequential logic (state machine) of the Inverter-Bus protocol is implemented in firmware in a FPGA located at a Vehicle Controller Interface (VCI) board inserted in a PC. Due to the high capacity of a FPGA, the VCI allows to implement more than one vehicle controller. The Bus Master is also implemented in one of the VCIs. The VCI-board is attached to the internal PCI bus of the PC.

The inverters consist of the power-section (IGBTs, drivers etc) and a CPLD-based Inverter Interface board handling the bus-protocol. Physically, the Inverter Bus is a 16 bit parallel bus (flat ribbon cable) based on RS 485 electrical specification.

Figure 2.6 shows the overall timing of the Inverter-Bus [31]. The basic cycle time is set to 100 μs. This corresponds to a 10 kHz control frequency for each vehicle controller and a 5 kHz switching frequency for each active inverter.

In Figure 2.6, at $t = 0$ μs, the Inverter-Bus Master issues a call for the Vehicle Controller “0”. Prior to this event, the Vehicle Controller “0” must have written the following information into local registers:

- The address of the inverter, which presently supplies the vehicle “0”. In the example of Figure 2.6, this is the inverter #24.
- The time when switching in the three inverter phases will take place (3∗12bit). This time is measured from the instant when all three phases completely received their timing information.
- Next (commanded) “Switching State” of each inverter phase.

As the Bus Master transmits a clock signal across the bus, all VCIs and all Inverter Interfaces operate synchronously to this clock. When a VCI sees its own address on the bus, it issues immediately (clock synchronously) the address of the inverter, which supplies the vehicle. Without any gap in between, the address is followed by the “Switching State” and the timing information for the next switching event is coded in 12 bits.

When an Inverter Interface sees its own address on the bus, it starts the A/D-conversion for the 3 stator currents and stores internally the received timing and switch-

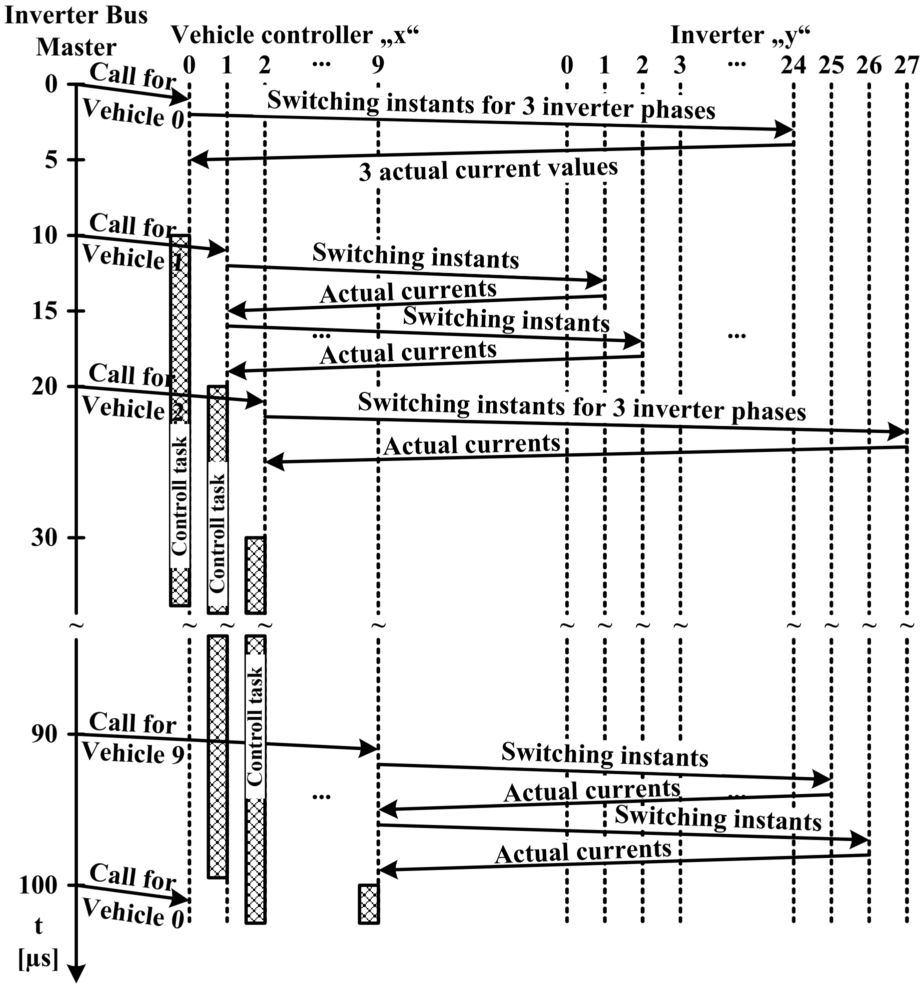

Figure 2.6: Overall timing of the inverter-bus

ing state for the next switching phase. When the reception of this information is completed without any gap, the Inverter Interface starts the transmission of the actual currents (3*12bit). This is completed at *t* = 5 µs in Figure 2.6. When the time window for the VCI “0” ends (after 10µs), the control task for vehicle “0” starts in the vehicle controller.

The sequential logic of the Inverter Interface is implemented in a CPLD. In the CPLD, timers and comparators are implemented. With these functions, the pulse pattern of a Space Vector Modulator is generated and fed to the IGBT-drivers directly. Additional protections like over current and over temperature protections are included too.

In the example of Figure 2.6, there is no bus activity between *t* = 5 µs and *t* = 10 µs. At *t* = 10 µs the procedure which was described for vehicle “0” is started for vehicle “1”. But now, it is assumed that vehicle “1” is actually located between stator “1” and

"2". In this situation the Vehicle Controller 1 has to control inverter 1 as well as inverter 2 simultaneously is such a way, that the commanded force is generated by both stators together. This is a challenging control task, as the force of each stator heavily depends on the position of the vehicle. In the time between *t* = 15 µs and *t* = 20 µs, the information on switching instants and actual current is exchanged between VCI "1" and Inverter Interface 2 and no idle bus time is left.

If there are less than 10 vehicles, idle time is allocated for the non-existing VCIs, but the timing for the controllers in operation remains unchanged. The Inverter Bus protocol is implemented on a RS-485 based 16-bit parallel bus. A standard, unshielded ribbon cable is used to link all components [31].

The Bus Master always drives four control signals, CLK (clock), ADDR (address/data), WR (write) and RD (read) as shown in Figure 2.7. All members connected to the Bus are synchronized to these signals. Each VCI needs one CLK cycle to write the inverter address and the switching state on the bus, three CLK cycles to write the switching time information of each phase and three CLK cycles to read the actual currents. A total of 2x7 CLK cycles are necessary to control two inverters. Additionally, the bus master needs one CLK cycle at the beginning in order to call the vehicle con-

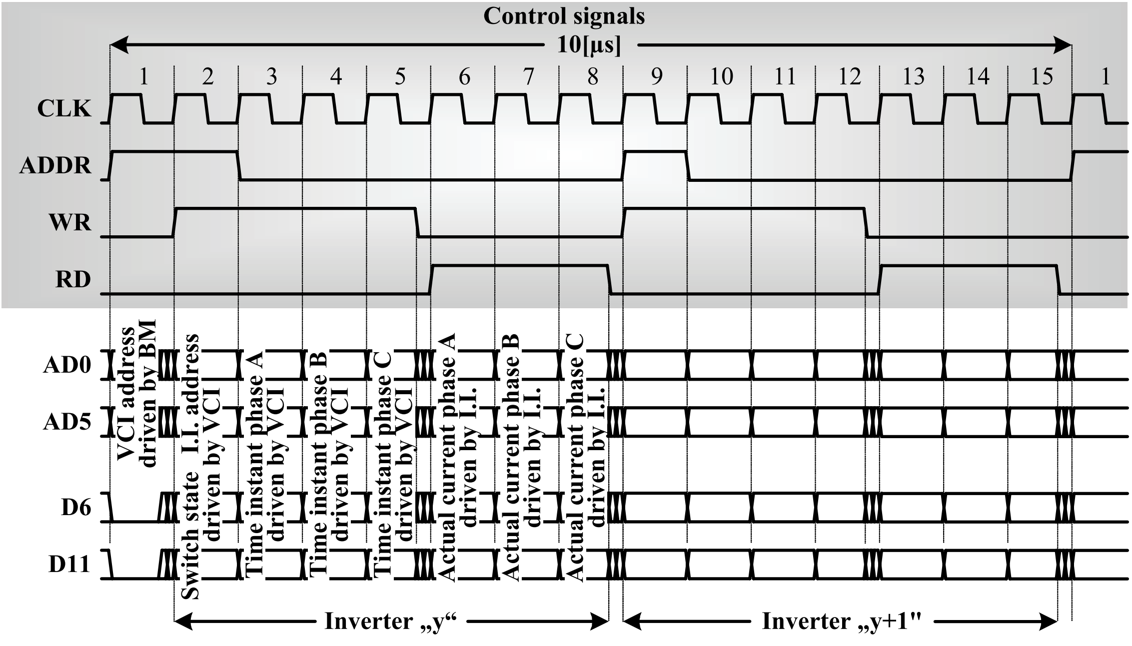

Figure 2.7: Inverter-Bus protocol. VCI: Vehicle controller interface. BM: Bus master. I.I.: Inverter interface

troller. To serve 10 vehicle controllers in 100 µs, a total of 15 CLK cycles in 10 µs are necessary, i.e. a CLK frequency of 1,5 MHz. Figure 2.7 shows the timing for the 16-bit signals in a time slot of 10 µs.

The RS-485 Standard specifies electrical properties of the differential signals used by bus- transmitters and receivers. Up to 32 members can be connected to a RS-485 bus (unit load, 12 kΩ), but there are transceivers with 1/2, 1/4 and up to 1/8 unit load allowing to connect up to 256 members [32].

2.3.2. Distributed vehicle controller

The bandwidth of the inverter-bus will be always a limiting factor to scale the system to an arbitrarily large, even if future busses with higher bandwidth will be available. The bottleneck of an inverter-bus that has to enable communication between each controller and each inverter within a time slot of 100 µs, can be overcome with the alternative of a totally distributed system for control and power-processing. Figure 2.8 shows a system with 2 vehicles, 8 segments and 8 inverters, where one controller is assigned to each inverter and the actual and reference position is transmitted via a real-time Ethernet. Additional high speed point-to-point communication (not shown in Figure 2.8) between two neighboring controllers is necessary in the time interval when a vehicle passes from one stator segment to the next one [29]. But this topology is not part of this dissertation.

Table III resume the main advantages and draw backs of centralized and distributed controllers.

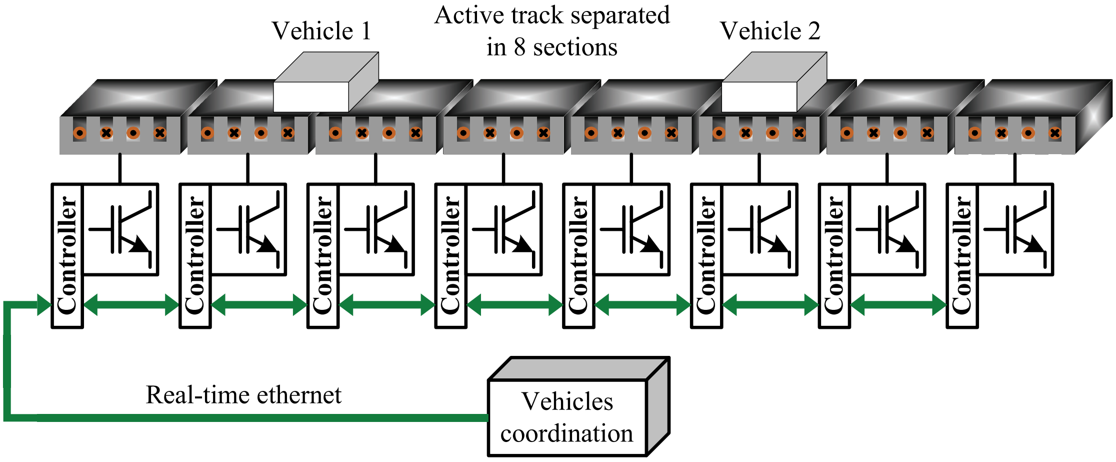

Figure 2.8: Distributed communication and control system.

Table III: Comparison of centralized and distributed controllers.

	Centralized vehicle controller	Distributed vehicle controller
Advantages	✓ Only one controller per vehicle	✓ Applicable for large systems
Drawbacks	✗ Limited number of vehicles ✗ High bandwidth necessary	✗ High number of controllers necessary

3. Experimental set-up

3.1. Motor

In laboratory, a simplified set-up is used compared to the one proposed in section 1.2.2. The shortest carriageway forming a closed path is a circle. The experimental set-up for this Dissertation includes a double-sided circular stator permanent magnet linear motor with one vehicle, as shown in Figure 3.1. The experimental machine was a donation from industry, and it does not fulfill all the requirements of a practical application, but it is a highly welcomed donation suitable to study many control problems. The length of the carriageway is 3.12 meters approximately. The circular stator is divided in 8 double-sided segments, each one covering 45° of the annulus. In the center of the linear circular machine, there is a high torque load machine with an encoder at the shaft, which is used as position feedback for the control loop. The load machine can add some load force disturbance to the vehicle in order to develop and test controllers with high dynamic load stiffness.

Figure 3.2a shows the segmental lamination of three poles forming a polygon. Due to this special arrangement of the poles along the approximated arc, every third tooth must be “V-shaped”. This special geometry introduces some additional harmonics in the air

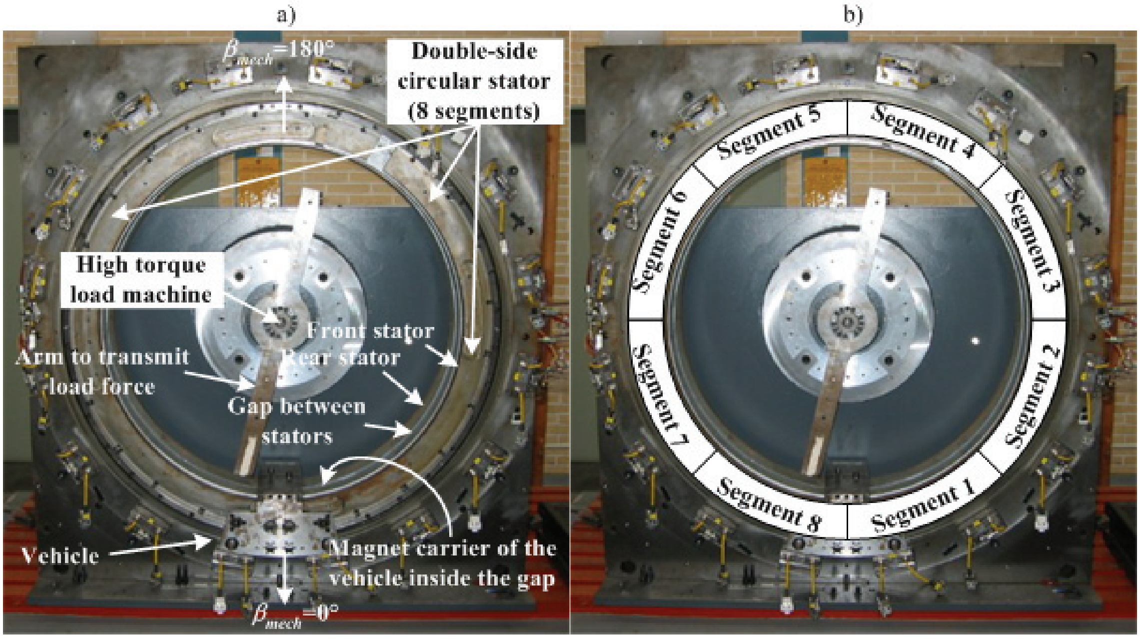

Figure 3.1: Experimental set-up motor (a) and its segmentation (b).

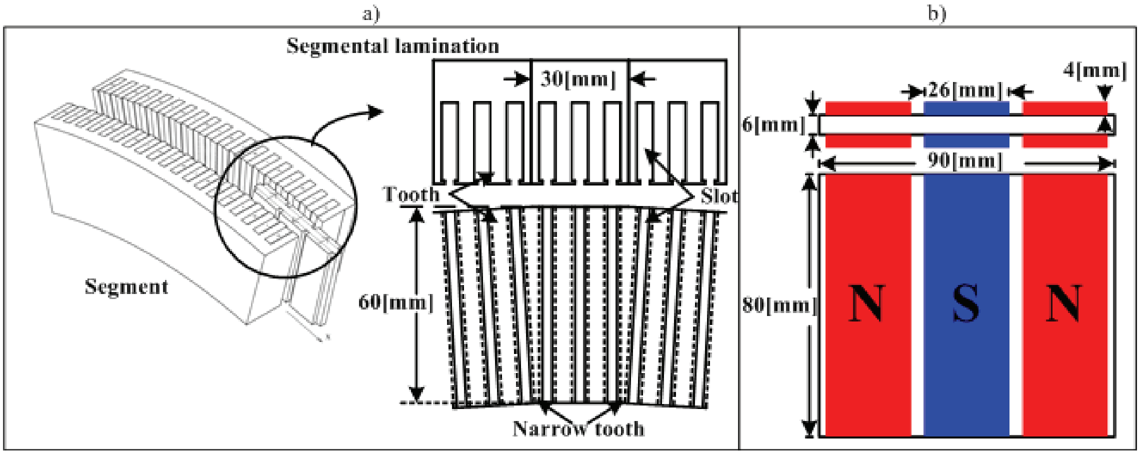

Figure 3.2: Segmented long stator linear motor. a) Segmental lamination of the stator, b) magnet carrier

gap field, i.e. in the induced voltage (*EMF*) of the machine.

The magnet carrier in Figure 3.2b has a straight alignment of the magnets. It causes a considerably high cogging force.

The stator segments of the experimental machine are provided with distributed three phase windings, although other winding systems like tooth-windings may be more interesting for a real application. Each 45° segment has 13 poles and the vehicle has 3 poles (3 magnets) at each side. Figure 3.3 shows the partial winding scheme for two consecutive stator segments, taking only the last four poles of one segment and the first four poles of the next segment into account. Due to the odd number of poles of one stator segment, the electrical angle between two consecutive stator segments must be shifted by 180°. The windings are arranged in 2 layers, spaced by 3 teeth (each 3 slots)

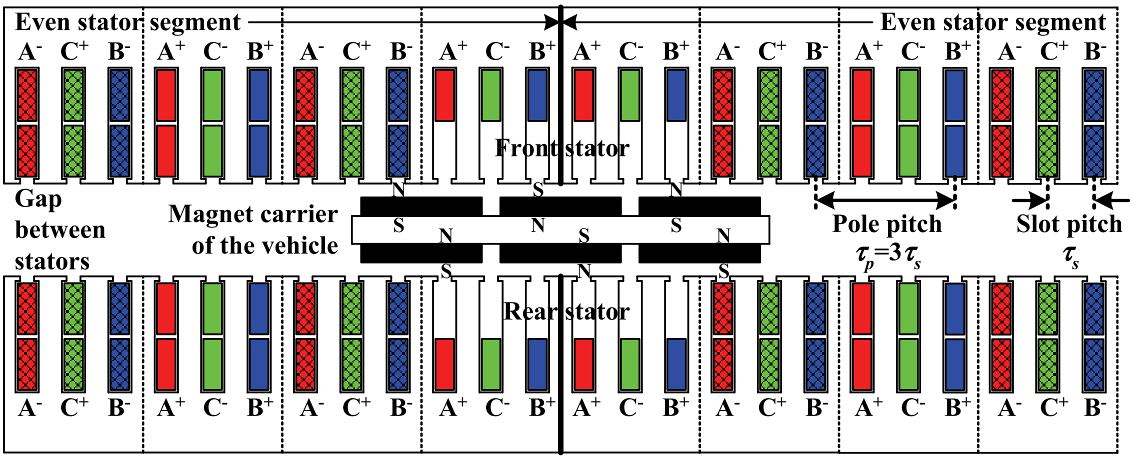

Figure 3.3: Partial winding scheme for two consecutive segments of the double sided linear motor and its magnet carrier.

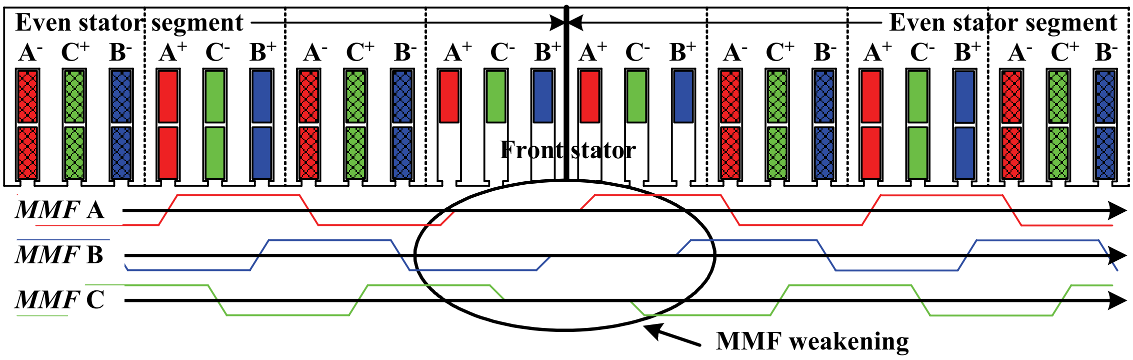

Figure 3.4: Magneto Motive Force (*MMF*) distribution in the region between two segments.

per phase. At the end of a segment, only one layer is covered, producing a magneto motive force (*MMF*) weakening (Figure 3.4).

The winding alignment between the two sides of the double sided stator is made in such a way that the flux linkage is complemented in the same phase (Figure 3.3). Due to the alignment of the winding, the flux lines produced by the magnets and currents go from one side of the stator to the other side, through the vehicle's magnet carrier, and are closed through the neighbor pole or through the circular yoke of the machine. This allows to connect the windings of both sides of one segment in parallel and fed them from one inverter. Compared with series connection, the parallel connection between the front and the rear side reduces the induced voltage at the terminals, allowing a higher speed for a given inverter voltage. As drawback, the inverter must supply the sum of the currents from each side. Mechanical asymmetries (e.g. phase shift between front and rear side) can produce differences in the induced voltages for a phase among front and rear side. Then, through the parallel connection, undesired circulating currents between the sides can flow.

On the other hand, the serial connection between the front and the rear sides would duplicate the induced voltage for a given speed, but reduce the current demand from the inverter. Mechanical asymmetries would not produce current fluctuations among the sides, but introduce additional harmonics in the induced voltage.

The rated values and construction information of the machine are shown in **Table IV**.

The magnet carrier of the machine covers only 23% of the total segment (3 out of 13 poles). This produces a small *EMF*-to-speed ratio of only 7 Vs/m. The maximal speed

Table IV: Motor parameters for a side segment.

Nominal current (one side)	I_N = 26,22 A	Slots per segment	39
Peak current (one side)	I_{MAX} = 52 A	Winding arrangement	distributed
Thrust force (one side)	F_N = 300 N	Winding type	2 layers
Maximal thrust Force (one side)	F_{MAX}= 550 N	Number of coils (per phase)	12
Stator resistance (one side)	R = 0,95 Ω	Number of turns per coil	20
Stator inductance (one side)	L = 6,25 mH	Pole pitch	0.03m
Mover Mass	M = 12.5 Kg	Tooth pitch	0.01m
Segments	8	Poles of the magnet carrier	3
Poles per segment	13	Magnet material	N42 (NdFeB) 1,3T

of the Machine is not specified, but we limited it to 6,24 m/s (two turns of the annulus per second) due to mechanical restrictions.

3.2. Power supply

In the experimental set-up, the front and rear sides of the segments are connected in parallel. The parallel connection demands twice the current of **Table IV**, i.e. a maximum peak current of 104 A. Additionally, in order to reduce the necessary number of inverters, two segments displaced 180° in the annulus are connected in series (for the set-up only).

For the topology, with one controller per vehicle, described in section 2.3.1, the power supply system demands inverters (4 in this case) with access to the control signals of the IGBTs. This characteristic allows to build a dedicated electronic board, called “Inverter Interface”, to implement the modulator, current measurement, “Inverter-Bus” and protections. The Inverter-Bus is a dedicated high speed communication channel between the inverters and the vehicle controller and was described in section 2.3.1.1. Figure 3.5 shows the converters used for the experimental set-up and the motor connections.

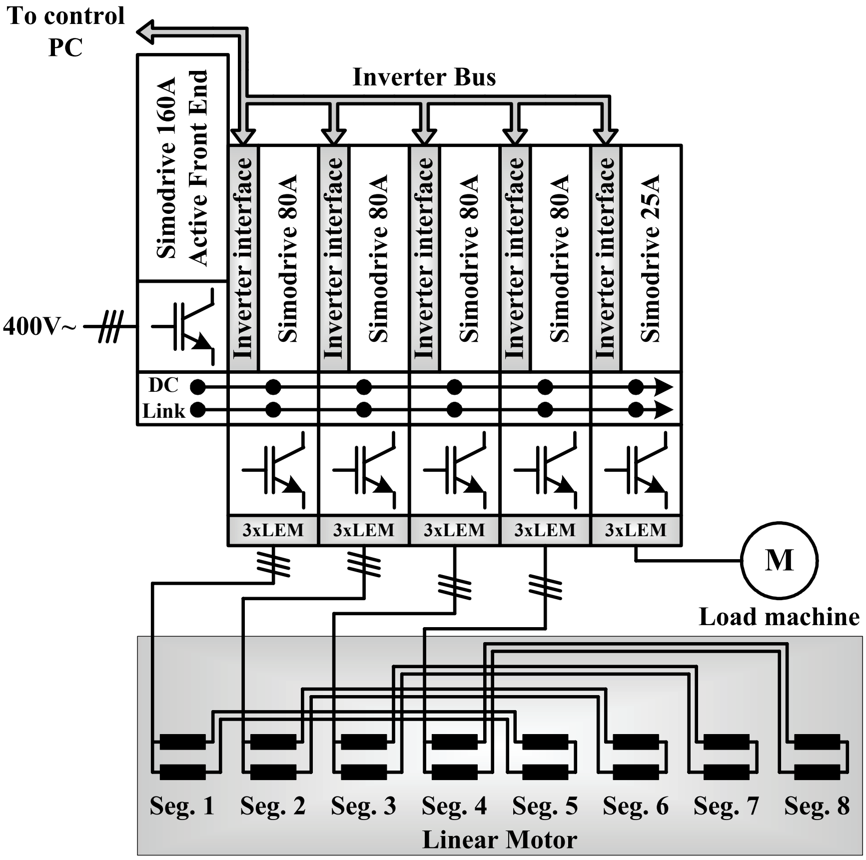

Figure 3.5: Simodrive 611 converter together with the Inverter Interface electronic developed in this work for the experimental set-up, and the motor segment connections.

The converter Siemens Simodrive 611 fulfills the above mentioned characteristics. The Simodrive 611 offers inverter power modules from 8 A to 400 A. For the set-up, four inverter modules of 80 A are mounted together to feed the linear motor. An additional inverter module of 25 A is used to feed the load machine. The inverter modules are fed through an Active Front End by a common DC-Link of 600 V [33].

3.3. Inverter interface

There is no commercial equipment to fulfill the flexibility required for the control of the linear drive proposed in chapter 2. Dedicated electronic must be designed and realized in order to achieve a desired thrust force profile overall the carriage way. The development and construction of hardware is a challenging work, specially where high frequency digital signals must coexist with analog signals at the same PCB, located close to fast switching power IGBTs.

The inverter interface must perform 4 main tasks, summarized as follows:

- Communication for data transport from and to the vehicle controller under the protocol described in section 2.3.1.1.
- Acquisition of the phase currents i_a, i_b and i_c.
- Gate signals generation
- Over current and over temperature protection.

To perform the above mentioned tasks, the Inverter Interface board was designed with a power full CPLD EPM9320 from Altera. When the CPLD decodes its own address from the Inverter Bus, the communication process starts. At first, the CPLD captures the next switching state for the IGBT's and switching times for each phase from the Inverter Bus. In between the CPLD starts the A/D converters. After the CPLD has received the switching times, the transceivers of the Inverter Interface take over the control of the bus, i.e. the Inverter Interface acts as Bus-Master for a short time slot. In this time slot, the A/D converters of the Inverter Interface board write sequentially the actual currents onto the Inverter Bus. Figure 3.6 shows the block diagram of the Inverter Interface board. The CPLD uses a 40 MHz clock which allows to count 4000 increments in 100 µs. In this way, the time resolution provided by 12 bit data ($2^{12} = 4096$) are well utilized.

The currents i_a, i_b and i_c are measured by the transducers LAH 25-P from LEM. The acquisition is done by the 12 bit A/D converters LTC1410 from Linear Technology. The A/D conversion must be ready before the CPLD starts transmitting the data to the vehicle controller. The LTC1410 has a conversion time of 800 ns. This allows the CPLD, to start the A/D converter 1,5 Bus-clocks before beginning the transmission. The modulator is synchronized with the current acquisition in such a way that there is practically no delay between the middle of the zero vector and the sampling of the actual phase currents.

In case that the VCI does not need to address a Inverter Interface, the CPLD is excluded from the communication and automatically disables the gate signals. Additional safety tasks are included too. The over current protection is based on comparators. Their binary output is passed through to the CPLD. The over temperature signal is available from the inverter.

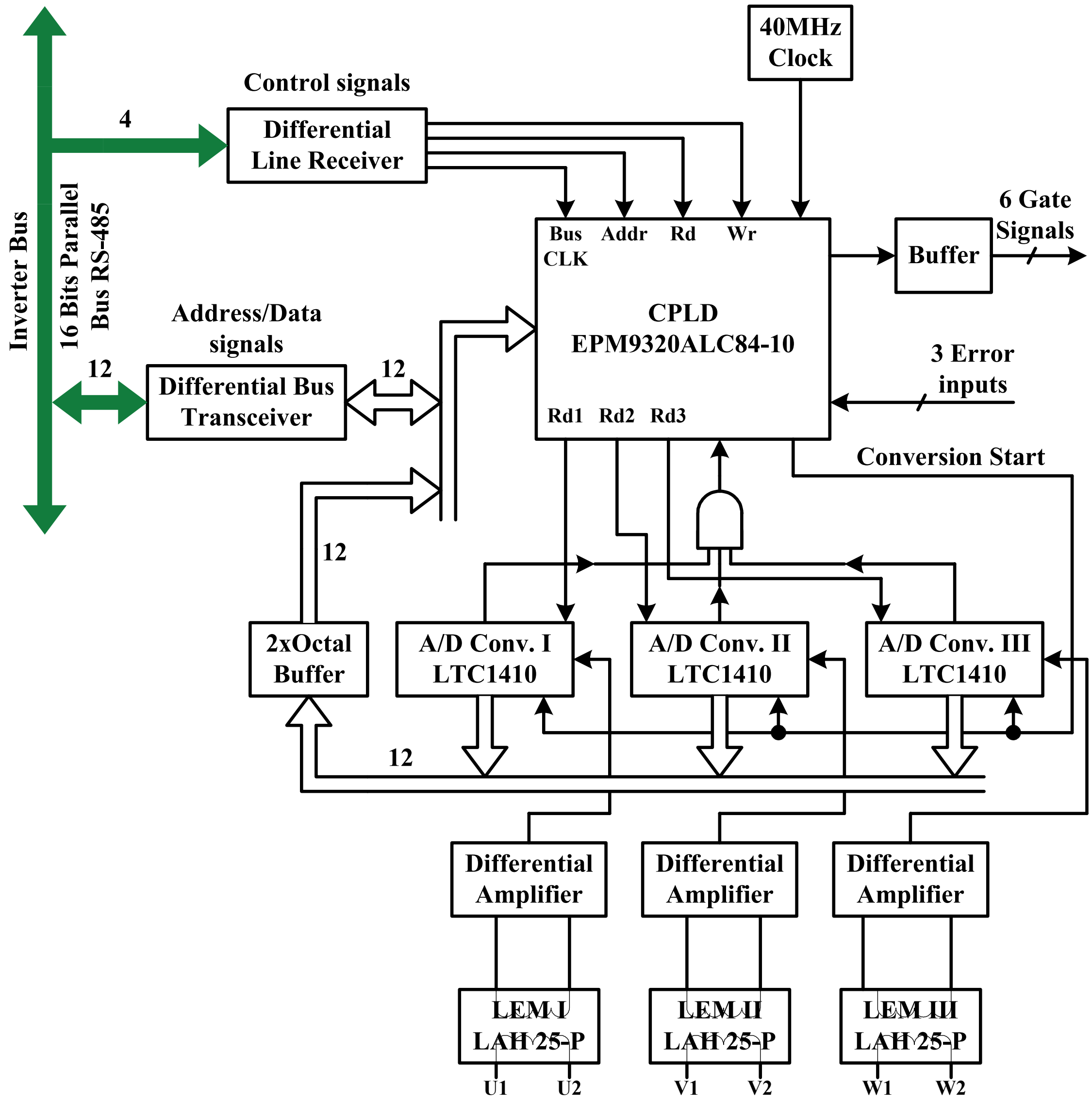

Figure 3.6: Block diagram of the Inverter Interface board.

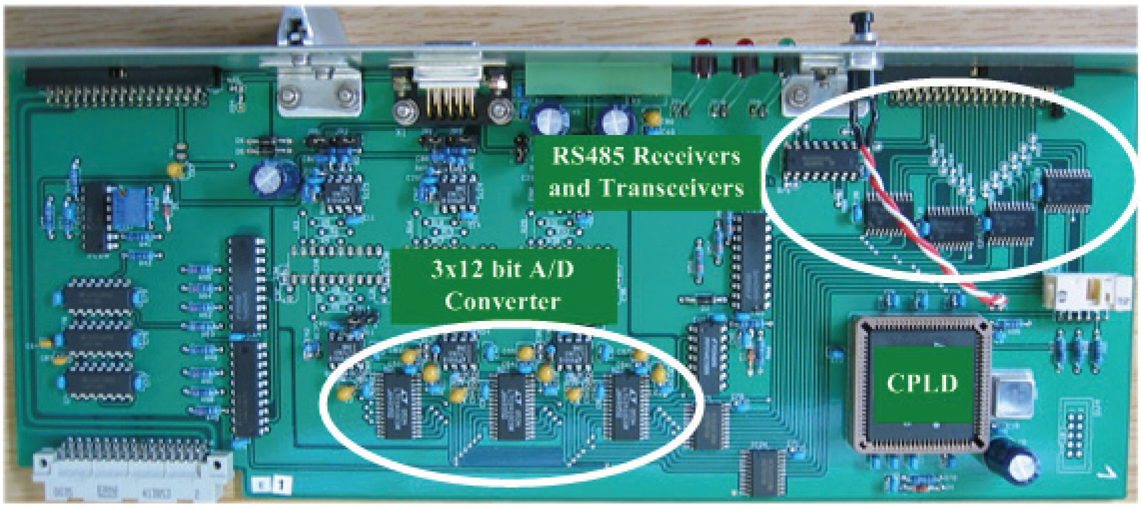

Figure 3.7: Inverter Interface board implemented in a four layer PCB.

The Inverter Interface board is mounted inside of the inverter Simodrive 611. Additionally, at the PCB analog and digital signals must coexist without interference. A four layer PCB design is necessary to fulfill the EMC-requirements. Figure 3.7 shows the Inverter Interface board used in the experimental setup.

3.4. Position Detection

For a real application, stations where materials are processed will be located at straight segments of the carriageway. To achieve a high positioning accuracy (few µm), linear measuring systems will be used within the processing stations. For motion outside processing stations, less accuracy may be sufficient and sensor-less motion control methods will be preferred in order to save sensor costs.

In the experimental set-up an incremental encoder, attached to the load machine for position detection of the vehicle, is used. The incremental encoder generates 2048 periods of sine and cosine signals per turn, and also one reference pulse per turn. Using only the zero-crossings of the encoder’s signals, a resolution of 400µm in the vehicle positioning is possible. Interpolation based on the arc-tangent evaluation of the sine/ cosine-signals with 12-bit AD-converters can increase the resolution up to 4µm. But there is a lot of elasticity and backlash between the rotary encoder of the load machine and the vehicle, which strongly reduces the quality of the position and speed measurement.

A separate board connected to the ISA bus in the PC is used to evaluate the sine and cosine signals. The evaluation of the position is triggered by the control interrupt.

3.5. Vehicle controller interface

At the beginning of the work, the vehicle controller interface (VCI) was developed and realized to be attached to the ISA-Bus [31] of the PC. Due to the following reasons the decision for a redesign of the VCI-board was taken:

- The ISA-Bus is slow and represents an old bus system, which is supported less and less. Many new PC-motherboards don’t have any ISA-slots.
- Practical experiences showed that the PC-potential (PC’s signal ground) should be separated from the inverter and sensors potential at least if the system is spread out for several meters in an environment, where fast switching inverters are located.

Therefore, a new VCI-board, PCI based, was developed [62]. Since the PCI-Bus is essentially more complex than the old ISA-Bus, the CPLD has to be changed to a FPGA. Part of the firmware in the FPGA is “intellectual property” of Altera which helps to implement the PCI-Bus protocol. This firmware realizes a bridge within the FPGA between the external PCI-bus and another bus internally in the FPGA, at which the user can add its particular firmware components. In the case of the VCI, this user-firmware is the Inverter Bus protocol.

Figure 3.8 shows a block diagram of the developed VCI-board. The isolation between the Inverter Bus signals and the FPGA is done by optocouplers. The firmware of the FPGA for the bus-master and vehicle controller #0 is made up four parts:

- Bus-master module, which generates the control signals.
- State machine for the communication protocol.
- PCI protocol, that control the transfer between the PC and the VCI-board.
- PCI local side, interface to the specific control of read and write and interrupt management.

Due to the high logic capacity of the FPGA, more than one vehicle controller can be

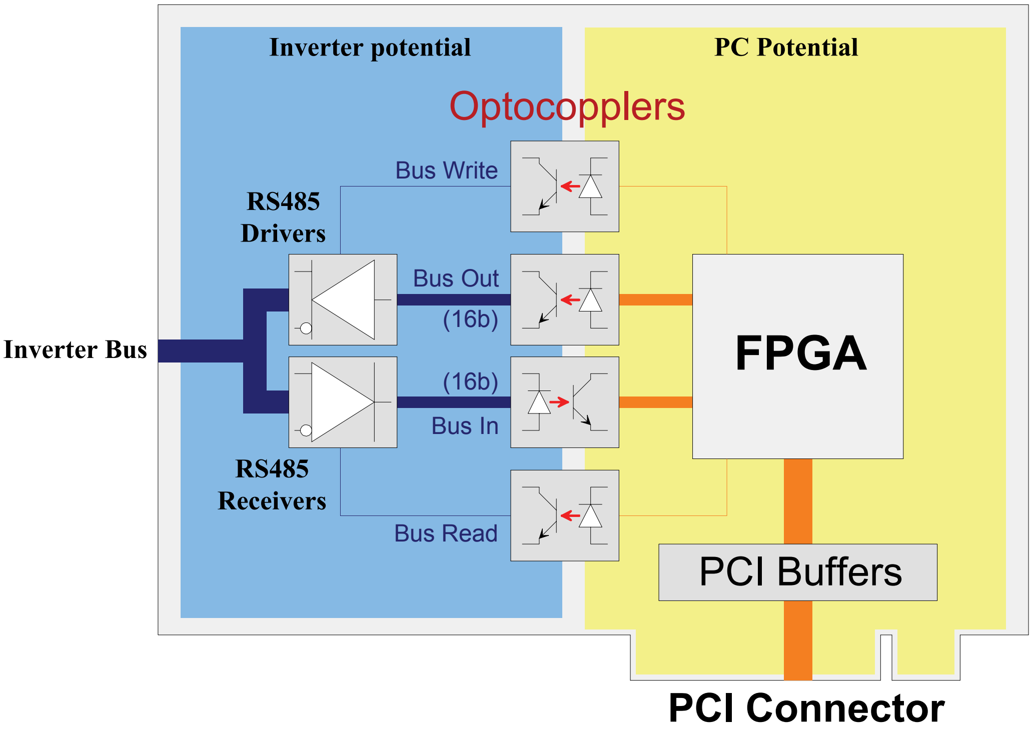

Figure 3.8: Block diagram of the PCI board.

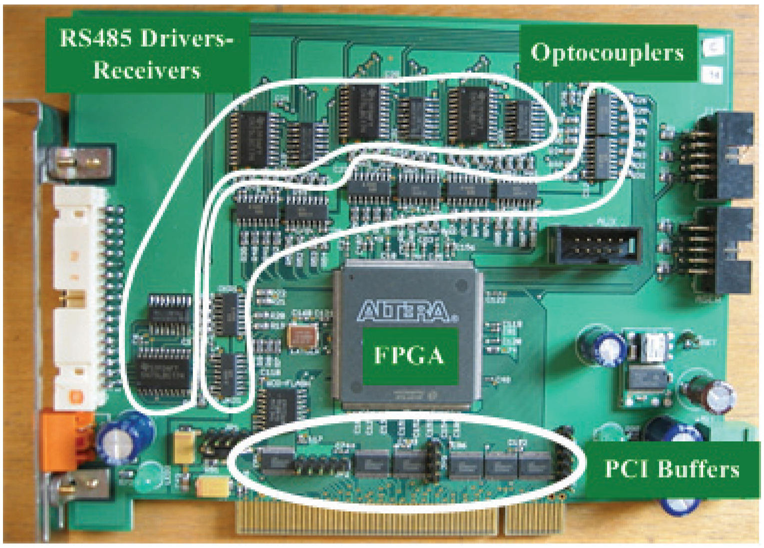

Figure 3.9: Developed VCI-board.

implemented into one VCI-board. Figure 3.9 shows the developed VCI-board.

3.6. Vehicle controller and Real-time control

The Bus Master will synchronize the communication between the vehicle controllers and the inverters, and also will trigger the control task in the PC. After the vehicle controller interface (VCI) has received the actual currents from the Inverter Bus, it triggers an interrupt to the vehicle controller (PC). Then, the PC starts to read the actual currents from the VCI local registers and executes the control task. At the end of this task, the vehicle controller writes back the switching time information to the VCI for the next PWM cycle.

The PC must respond to the interrupt and execute the control task in less than 100µs. To fulfill this demand, the PC must work under a real-time operating system. For the experimental set-up the operating system Linux RTAI (Real Time Application Interface) is used [34]. RTAI was originally founded by Prof. Paolo Mantegazza from Dipartimento di Ingegneria Aerospaziale, Politecnico di Milano, but today offers many variants and is a result of a community effort. RTAI is mainly a kernel patch that adds a real-time-kernel between the hardware and the Linux kernel. Then, the real-time-kernel takes the control over all interrupts (hard- and soft). In this way RTAI can transparently process interrupts while leaving all the other, non real-time process to Linux. The architecture of the real-time operating system Linux RTAI is shown in Figure 3.10 [34].

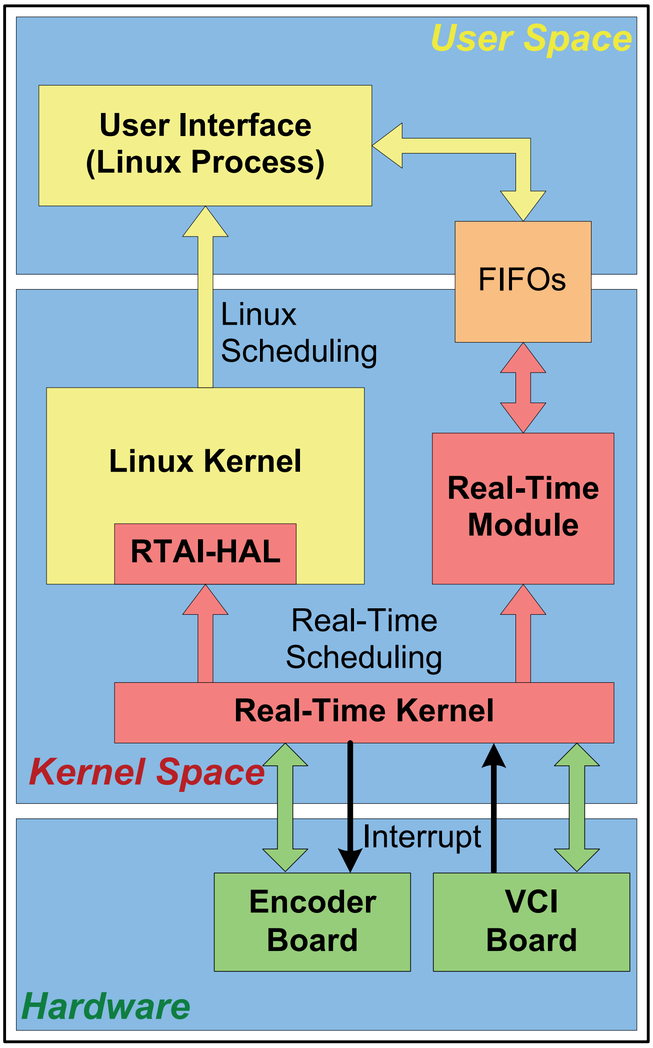

Figure 3.10: Architecture for Linux RTAI.

At the hardware level of Figure 3.10 the VCI board and the encoder evaluation board are found. The real-time kernel (kernel space) is responsible to schedule the control task with the highest priority, triggered by the VCI board. In kernel space the control task (real-time tasks) and the data logging for debug takes place. The data logging allows to analyze the control behavior and debug the algorithms. The control algorithms will be studied in detail in the next chapter. To access the logged data, RTAI offers FIFOs as interface to the user space. Linux offers a wide branch of tools for the user space like: network support, development tools, graphic user interface (GUI) tools and so on. For the experimental set-up, a basic GUI was developed.

The complete set-up structure is shown in Figure 3.11. This set-up is the base for all the experimental verifications for the proposed topology of passive multi-vehicle segmented long stator linear drives.

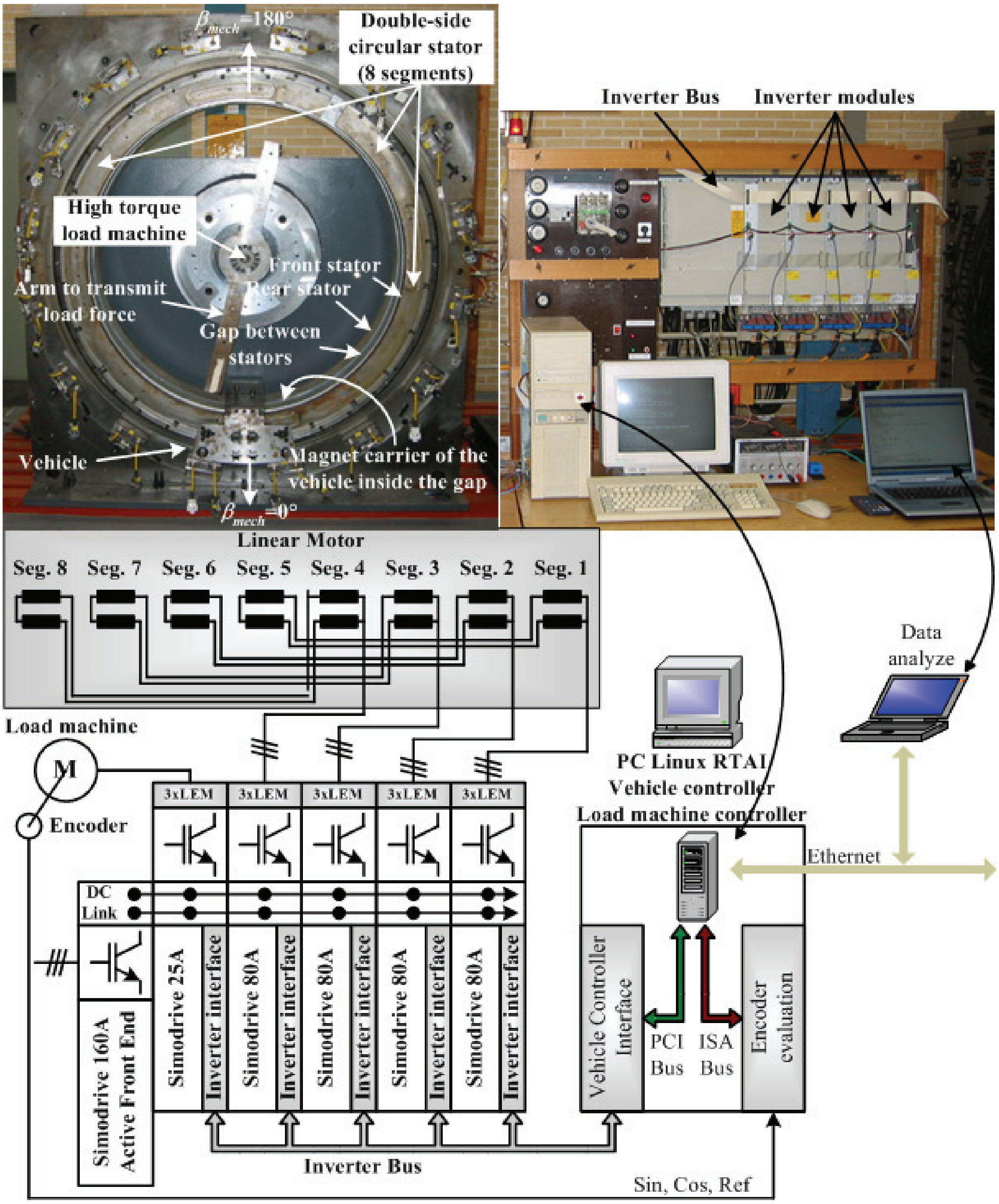

Figure 3.11: Complete structure of the experimental set-up. Motor – power supply system – controller (PC Linux RTAI)

4. Model of the machine

4.1. Electric model

The electric model of a Linear Permanent Magnet Synchronous Motor (LPMSM) is similar to the rotative motor. The main difference is produced by an added phenomena, the longitudinal end effect [12][21]. Longitudinal end effect is classified as static or dynamic. The static effect consists of unbalanced stator three phase currents due to non symmetrical placement of phases with respect to stator core longitudinal ends. The dynamic effect is related to Linear Induction motors in motion as new portions of the mover (vehicle) enter the stator magnetic field zone. With Gauss flux law, it is observed that additional currents are induced in the mover by the so-called entry and exit end effect field [12]. But, the dynamic longitudinal end effect is negligible in LPMSM's.

In the literature, the model of the Permanent Magnet Synchronous Machine (PMSM) (similar to the LPMSM model) is mostly simplified [14][21][43], where the flux in the air gap is mainly produced by the magnet and the stator currents. The joke induced current and its effect are neglected. Harmonics in the flux linkage are produced by the stator slots, static longitudinal end effect, iron saturation and asymmetries in the winding construction. For these reasons, the linked fluxes $\Psi_a(i_a,i_b,i_c,x)$, $\Psi_b(i_a,i_b,i_c,x)$ and $\Psi_c(i_a,i_b,i_c,x)$ are functions dependent of the currents i_a, i_b, i_c and the position x. The voltage equation for the LPMSM in stationary stator *abc*-coordinate system is:

$$\vec{u}_{abc} = \mathbf{R_{abc}} \cdot \vec{i}_{abc} + \frac{d\vec{\Psi}_{abc}}{dt}$$

$$\text{with } \vec{u}_{abc} = \begin{bmatrix} u_a \\ u_b \\ u_c \end{bmatrix}, \mathbf{R_{abc}} = \begin{bmatrix} R_a & 0 & 0 \\ 0 & R_b & 0 \\ 0 & 0 & R_c \end{bmatrix}, \vec{i}_{abc} = \begin{bmatrix} i_a \\ i_b \\ i_c \end{bmatrix}, \vec{\Psi}_{abc} = \begin{bmatrix} \Psi_a \\ \Psi_b \\ \Psi_c \end{bmatrix} \qquad (1)$$

The star connection with isolated neutral point allows to eliminate the zero sequence current i_0. Additional disturbances, like high frequency common mode currents due to capacitive coupling between the stator windings and the stator iron, are neglected. This allows to apply the linear transformation (2) [14][35][36] and rewrite (1) in stationary, two-phase stator α-β coordinate system (3).

$$\vec{u}_{\alpha\beta}=\begin{bmatrix}u_\alpha\\u_\beta\end{bmatrix}=\underbrace{\frac{2}{3}\begin{bmatrix}1 & -\frac{1}{2} & -\frac{1}{2}\\ 0 & \frac{\sqrt{3}}{2} & -\frac{\sqrt{3}}{2}\end{bmatrix}}_{\mathbf{T_{abc\to\alpha\beta}}}\cdot\vec{u}_{abc} \qquad \vec{u}_{abc}=\underbrace{\begin{bmatrix}1 & 0\\ -\frac{1}{2} & \frac{\sqrt{3}}{2}\\ -\frac{1}{2} & -\frac{\sqrt{3}}{2}\end{bmatrix}}_{\mathbf{T_{\alpha\beta\to abc}}}\cdot\vec{u}_{\alpha\beta} \tag{2}$$

Normally, the stator winding of the machine has the same numbers of turns for each phase, i.e. the total resistance for each phase is the same (R_a=R_b=R_c=R). This reduces $\mathbf{R_{\alpha\beta}}$ to a diagonal matrix.

$$\vec{u}_{\alpha\beta}=\underbrace{\mathbf{T_{abc\to\alpha\beta}}\cdot\mathbf{R_{abc}}\cdot\mathbf{T_{\alpha\beta\to abc}}}_{\mathbf{R_{\alpha\beta}}}\cdot\vec{i}_{\alpha\beta}+\frac{d\vec{\Psi}_{\alpha\beta}(\vec{i}_{\alpha\beta},x)}{dt}$$

$$\text{i.e. }\mathbf{R_{\alpha\beta}}=\begin{bmatrix}\frac{1}{3}\left(2R_a+\frac{1}{2}\left(R_b+R_c\right)\right) & \frac{1}{2\sqrt{3}}\left(R_c-R_b\right)\\ \frac{1}{2\sqrt{3}}\left(R_c-R_b\right) & \frac{1}{2}\left(R_b+R_c\right)\end{bmatrix} \tag{3}$$

The magnetic axis of a LPMSM is fixed at the Secondary (mover) of the machine. The introduction of the mover-fixed *d-q* coordinate system (4) [14][35][36] allows to align the flux of the magnets along the *d* axis (field orientation), which simplifies the analysis.

$$\vec{u}_{dq}=\begin{bmatrix}u_d\\u_q\end{bmatrix}=\underbrace{\begin{bmatrix}\cos(\beta_m) & \sin(\beta_m)\\ -\sin(\beta_m) & \cos(\beta_m)\end{bmatrix}}_{\mathbf{T_{\alpha\beta\to dq}}}\cdot\vec{u}_{\alpha\beta} \qquad \vec{u}_{\alpha\beta}=\underbrace{\begin{bmatrix}\cos(\beta_m) & -\sin(\beta_m)\\ \sin(\beta_m) & \cos(\beta_m)\end{bmatrix}}_{\mathbf{T^{-1}_{\alpha\beta\to dq}}}\cdot\vec{u}_{dq} \tag{4}$$

with $\beta_m=\frac{\pi}{\tau_p}\cdot x$, and τ_p the pole pitch of the motor

Applying the transformation (4), the voltage equation of the machine (3) is rewritten in mover *d-q* coordinate system as in (5). The detailed mathematical steps are described in the appendix A.1.

$$\vec{u}_{dq}=\mathbf{R_{dq}}\cdot\vec{i}_{dq}+\frac{d\vec{\Psi}_{dq}}{dt}+\frac{\pi}{\tau_p}\cdot\begin{bmatrix}0 & -1\\ 1 & 0\end{bmatrix}\cdot\vec{\Psi}_{dq}\cdot\frac{dx}{dt} \tag{5}$$

The linked flux vector $\vec{\Psi}_{dq}$ is a function that depends on the current $\vec{i}_{dq}$ and position x. Then, the derivative $d\vec{\Psi}_{dq}/dt$ can be rewritten as in (6) [8][36].

$$\frac{d\vec{\Psi}_{dq}}{dt}=\frac{\partial\vec{\Psi}_{dq}}{\partial\vec{i}_{dq}}\cdot\frac{d\vec{i}_{dq}}{dt}+\frac{\partial\vec{\Psi}_{dq}}{\partial x}\cdot\frac{dx}{dt}$$

$$\text{With }\frac{\partial\vec{\Psi}_{dq}}{\partial\vec{i}_{dq}}=\begin{bmatrix}\frac{\partial\Psi_d}{\partial i_d} & \frac{\partial\Psi_d}{\partial i_q}\\ \frac{\partial\Psi_q}{\partial i_d} & \frac{\partial\Psi_q}{\partial i_q}\end{bmatrix}=\mathbf{L}_{\mathbf{dq}}^{\mathbf{diff}} \tag{6}$$

Introducing (6) in (5), the voltage equation of the motor is rewritten as in (7).

$$\vec{u}_{dq}=\mathbf{R}_{\mathbf{dq}}\cdot\vec{i}_{dq}+\mathbf{L}_{\mathbf{dq}}^{\mathbf{diff}}\cdot\frac{d\vec{i}_{dq}}{dt}+\underbrace{\left(\frac{\partial\vec{\Psi}_{dq}}{\partial x}+\frac{\pi}{\tau_p}\cdot\begin{bmatrix}-\Psi_q\\ \Psi_d\end{bmatrix}\right)\cdot\frac{dx}{dt}}_{EMF} \tag{7}$$

From equation (7) is possible to identify different types of voltage drop. It presents a resistive voltage drop $\mathbf{R}_{\mathbf{dq}}\cdot\vec{i}_{dq}$, an inductive voltage drop $\mathbf{L}_{\mathbf{dq}}^{\mathbf{diff}}\cdot d\vec{i}_{dq}/dt$ and a rotational back *EMF*. The flux-position dependence e.g. for non sinusoidal field distribution along the air gap, introduces an additional term in the back *EMF* ($\partial\vec{\Psi}_{dq}/\partial x\cdot dx/dt$), which generates an additional pulsating component on the force [10].

Coming back to the α-β coordinate system, the flux linkage $\vec{\Psi}_{\alpha\beta}$ depends on the currents i_α, i_β, and the position x (8) [35][36].

$$\vec{\Psi}_{\alpha\beta}=\mathbf{L}_{\alpha\beta}(\vec{i}_{\alpha\beta},x)\cdot\vec{i}_{\alpha\beta}+\vec{\Psi}_{\alpha\beta PM}(x)=\begin{bmatrix}L_{\alpha\alpha} & L_{\alpha\beta}\\ L_{\beta\alpha} & L_{\beta\beta}\end{bmatrix}\cdot\begin{bmatrix}i_\alpha\\ i_\beta\end{bmatrix}+\begin{bmatrix}\Psi_{\alpha PM}\\ \Psi_{\beta PM}\end{bmatrix} \tag{8}$$

In (8), the inductance matrix $\mathbf{L}_{\alpha\beta}$ depends on the iron saturation and is a function of the current and the position. The flux linkage $\vec{\Psi}_{\alpha\beta PM}(x)$ represents the flux produced by the magnets. Applying the transformation (4) in (8), we get (9).

$$\vec{\Psi}_{dq}=\underbrace{\mathbf{T}_{\alpha\beta\text{-}\mathbf{dq}}\cdot\mathbf{L}_{\alpha\beta}\cdot\mathbf{T}_{\alpha\beta\text{-}\mathbf{dq}}^{-1}}_{\mathbf{L}_{\mathbf{dq}}}\cdot\vec{i}_{dq}+\vec{\Psi}_{dqPM}(x) \tag{9}$$

In (7) it is necessary to calculate the differential inductance $\mathbf{L}_{\mathbf{dq}}^{\mathbf{diff}}$ and the variation of the flux with respect to the position $\partial\vec{\Psi}_{dq}/\partial x$. In the ideal case, $\partial\vec{\Psi}_{dq}/\partial x$ would be zero. From (9) we obtain (10) and (11) (appendix A.2).

$$\frac{\partial \vec{\Psi}_{dq}}{\partial \vec{i}_{dq}} = \begin{bmatrix} \frac{\partial \Psi_d}{\partial i_d} & \frac{\partial \Psi_d}{\partial i_q} \\ \frac{\partial \Psi_q}{\partial i_d} & \frac{\partial \Psi_q}{\partial i_q} \end{bmatrix} = \underbrace{\begin{bmatrix} \frac{\partial L_{dd}}{\partial i_d} \cdot i_d & \frac{\partial L_{dd}}{\partial i_q} \cdot i_d \\ \frac{\partial L_{qd}}{\partial i_d} \cdot i_d & \frac{\partial L_{qd}}{\partial i_q} \cdot i_d \end{bmatrix} + \begin{bmatrix} \frac{\partial L_{dq}}{\partial i_d} \cdot i_q & \frac{\partial L_{dq}}{\partial i_q} \cdot i_q \\ \frac{\partial L_{qq}}{\partial i_d} \cdot i_q & \frac{\partial L_{qq}}{\partial i_q} \cdot i_q \end{bmatrix} + \begin{bmatrix} L_{dd} & L_{dq} \\ L_{qd} & L_{qq} \end{bmatrix}}_{\mathbf{L}_{\mathbf{dq}}^{\mathbf{diff}}} \tag{10}$$

$$\frac{\partial \vec{\Psi}_{dq}}{\partial x} = \frac{\partial \mathbf{L}_{\mathbf{dq}}}{\partial x} \cdot \vec{i}_{dq} + \frac{\partial \vec{\Psi}_{dqPM}}{\partial x} \tag{11}$$

For a sinusoidal magnetic field distribution, the linked fluxes $\Psi_d(i_d,i_q,x)$ and $\Psi_q(i_d,i_q,x)$ are constant for a given current and for all positions. In a real machine, harmonics appear in the air gap which depend on many factors, like the shape of the magnets, open or semi closed slots, end effect, etc [4][5][21].

To corroborate the above mentioned, the back *EMF* of the linear motor presented in chapter 3 is measured. The linear motor is moved at constant speed by the load machine. Then, the phase voltages (star point available) are sampled together with the position by the control PC. Figure 4.1a shows the normalized back *EMF* of the motor e_a/v, e_b/v and e_c/v. In Figure 4.1b are the normalized induced voltages e_d/v and e_q/v, where e_d and e_q are the transformed voltages with (2) and (4) into *d-q* coordinate system, and $v=dx/dt$ is the speed. The electric angle β_m for the transformation (4) is obtained from synchronous sampling of the position and e_a (appendix A.3). Equations (12) and (13) show the relation between the fluxes and the induced voltages.

$$\frac{e_d}{v} = \frac{\partial \Psi_d}{\partial x} - \frac{\pi \cdot \Psi_q}{\tau_p} \tag{12}$$

$$\frac{e_q}{v} = \frac{\partial \Psi_q}{\partial x} + \frac{\pi \cdot \Psi_d}{\tau_p} \tag{13}$$

The induced voltages of the setup machine are far away from a pure sinusoidal, and presents an important component of the 5th and 7th harmonics (Figure 4.1a).

The thrust force ripple of a LPMSM is mainly produced by two components. The first one is cogging force, which is generated by the interaction of the secondary (mover) magnetic flux and angular variations in the stator magnetic reluctance. By definition, no stator excitation is involved in cogging [44]. Teeth design and magnet arrangement can be optimized to reduce this effect [5][19]. This force is only dependent on the position and can be estimated using analytic calculations (i.e. magnetic equiva-

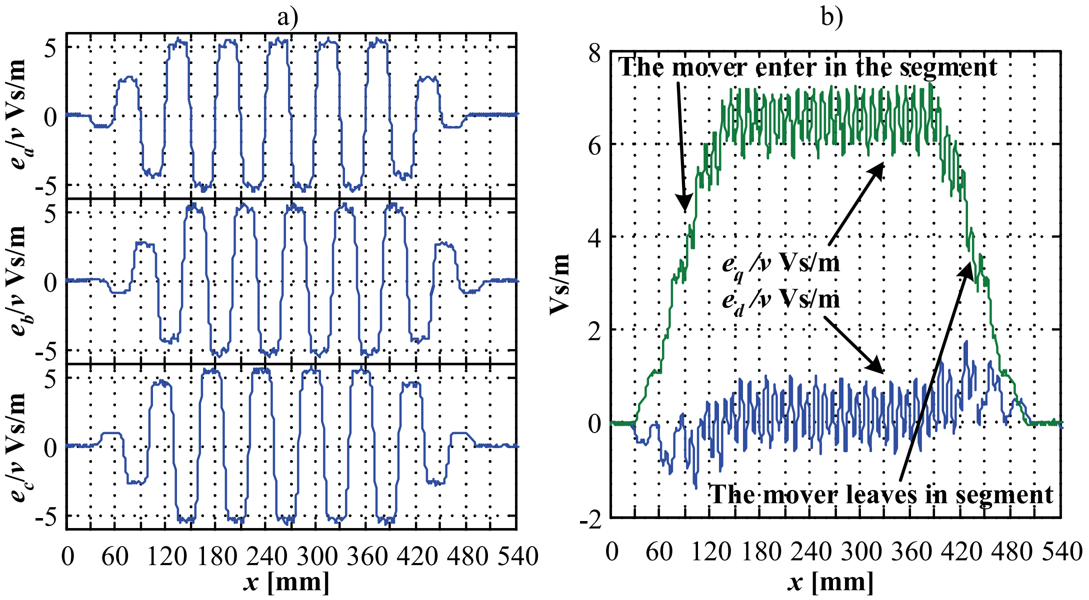

Figure 4.1: Normalized back *EMF* of the setup motor

lent circuits) or Finite Element methods. The second force ripple component is generated by the interaction of stator current magneto-motive forces (mmf's) and the angular variation in the rotor magnetic reluctance. Surface-magnet LPMSM machines generate almost no reluctance force [44].

The electromagnetic force can be controlled with the stator currents. The instantaneous electrical input power is given by:

$$P_{el} = i_a u_a + i_b u_b + i_c u_c = \vec{i}_{abc}^{\,T} \cdot \vec{u}_{abc} = \frac{3}{2} \vec{i}_{dq}^{\,T} \cdot \vec{u}_{dq} \tag{14}$$

By substituting (7) into (14) we get (15):

$$P_{el} = \frac{3}{2} \left(\underbrace{\vec{i}_{dq}^{\,T} \cdot \mathbf{R_{dq}} \cdot \vec{i}_{dq}}_{P_c} + \underbrace{\vec{i}_{dq}^{\,T} \cdot \mathbf{L_{dq}^{diff}} \cdot \frac{d\vec{i}_{dq}}{dt}}_{P_m} + \underbrace{\vec{i}_{dq}^{\,T} \cdot \left(\frac{\partial \vec{\Psi}_{dq}}{\partial x} + \frac{\pi}{\tau_p} \begin{bmatrix} -\Psi_q \\ \Psi_d \end{bmatrix} \right) \cdot \frac{dx}{dt}}_{P_{mech}} \right) \tag{15}$$

In equation (15), the input power is split into P_c ohmic power losses, P_m which is used to store Energy in the magnetic field, and P_{mech} which is the transferred mechanical power. The mechanical power for a linear motion is described by (16). Then it's possible to identify the electromagnetic force produced by a LPMSM (17).

$$P_{mech} = F \cdot \frac{dx}{dt} \tag{16}$$

$$\begin{aligned} P_{mech} &= F \cdot \frac{dx}{dt} = \frac{3}{2} \cdot \vec{i}_{dq}^{\,T} \cdot \left(\frac{\partial \vec{\Psi}_{dq}}{\partial x} + \frac{\pi}{\tau_p} \begin{bmatrix} -\Psi_q \\ \Psi_d \end{bmatrix} \right) \cdot \frac{dx}{dt} \\ &\Rightarrow F = \frac{3}{2} \cdot \vec{i}_{dq}^{\,T} \cdot \left(\frac{\partial \vec{\Psi}_{dq}}{\partial x} + \frac{\pi}{\tau_p} \begin{bmatrix} -\Psi_q \\ \Psi_d \end{bmatrix} \right) \end{aligned} \tag{17}$$

Introducing (11) in (17), the force equation (18) is obtained.

$$\begin{aligned} F &= \frac{3}{2} \cdot \vec{i}_{dq}^{\,T} \cdot \left(\frac{\partial \mathbf{L_{dq}}}{\partial x} \cdot \vec{i}_{dq} + \frac{\partial \vec{\Psi}_{dqPM}}{\partial x} + \frac{\pi}{\tau_p} \begin{bmatrix} -\Psi_q \\ \Psi_d \end{bmatrix} \right) \\ \Rightarrow F &= \frac{3}{2} \cdot \left(\underbrace{\vec{i}_{dq}^{\,T} \cdot \frac{\partial \mathbf{L_{dq}}}{\partial x} \cdot \vec{i}_{dq}}_{F_{Rel}} + \underbrace{\vec{i}_{dq}^{\,T} \cdot \frac{\partial \vec{\Psi}_{dqPM}}{\partial x} + \frac{\pi}{\tau_p} \cdot \vec{i}_{dq}^{\,T} \cdot \begin{bmatrix} -\Psi_q \\ \Psi_d \end{bmatrix}}_{F_M} \right) \end{aligned} \tag{18}$$

From (18) is possible to identify two types of forces, the reluctance force F_{Rel} and the mutual force F_M. The reluctance force F_{Rel} results from the interaction of the current *MMF* with the position variation in the secondary magnetic reluctance. Surface-magnet PMSM generate almost no reluctance force. The mutual force F_M results from the interaction of the current *MMF* with the secondary magnet flux distribution. This is the main force production in PMSM's. The mutual force F_M can also introduce force ripple [18][44]. The cogging force, which is independent on currents, is not represented in (18). Also, the reduction of *MMF* when the mover travels between two segments causing a weakening of force is not represented in (18).

Figure 4.2 shows the block diagram of a LPMSM according to (7). Inputs are the voltages $\vec{u}_{dq}$, the position x and the speed v, and outputs the stator current $\vec{i}_{dq}$ and the stator flux $\vec{\Psi}_{dq}$.

4.2. Finite Element Model

The Finite element method (FEM) is a mathematic tool to solve differential equations approximately. The method divides a (n-dimensional) surface in several elements and solves the differential equations on it. The border results of one element are used as initial conditions for the next element and so on. The definition of the boundary conditions are essential for convergence and to solve the problem. Smaller elements (finer grid) increases the accuracy but also the calculation effort. This method is very useful to

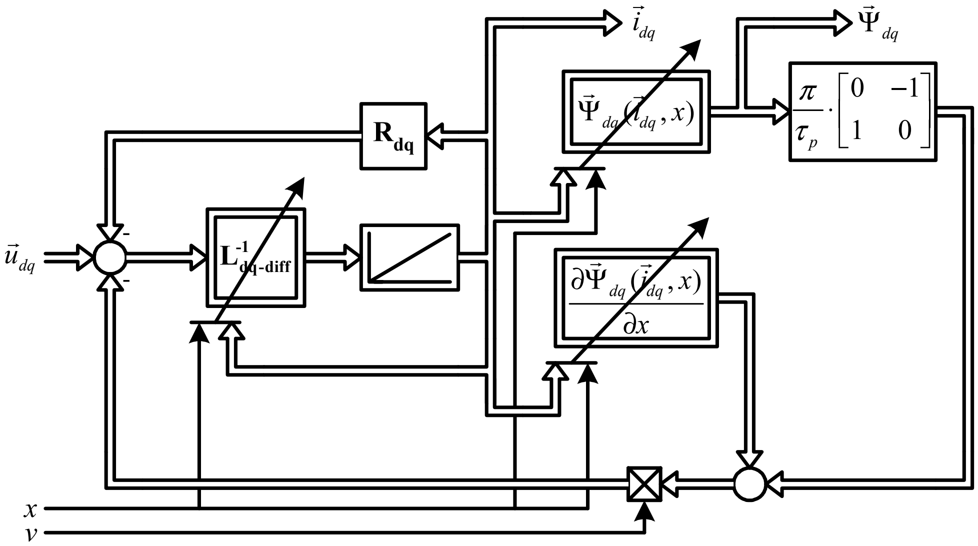

Figure 4.2: Block diagram of the LPMSM considering magnetic saturation and harmonics in the air gap magnetic field.

solve electromagnetic problems. The Maxwell equations find here a way to be solved on surfaces where different materials and excitations conditions can coexist. The boundary condition between two different materials, where the magnetic permeability changes, requires typically a high number of elements (fine grid) to reduce the error. From this, it is clear that the meshing of a surface is decisive for the quality of the results and the calculation time [38][45][46].

The non linear parameters of (7) can be obtained experimentally [11][37] or through a FEM of the machine. Sometimes it is difficult and expensive to do the necessary measurements. In some cases Finite Element calculations is a reasonable alternative. To achieve a good approximation of the non linear parameters, the geometry and also the material properties of the machine must be well known. A 2D model simplifies the problem and reduces considerably the calculation time, but the influence of the overhang and the “V” shape teeth (only for the special geometry of the motor of the setup) in the stack (Figure 4.3), is not considered. If eddy currents can be considered to be small due to the lamination, then 2D magneto static FE calculations can be used.

The mesh of the model and the material information determine the accuracy off the results. Therefore, it is important to understand how the software, which will be used, works. There are software programs that use adaptive meshing, which refine the mesh in areas, where the error between iterations exceed a predefined value (Figure 4.4).

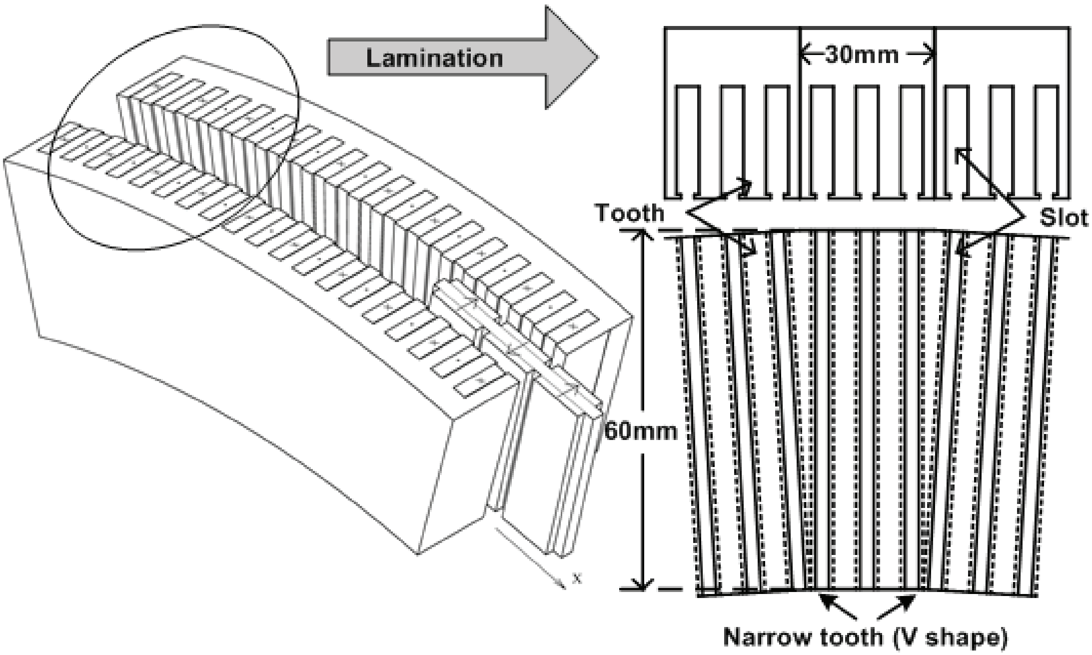

Figure 4.3: Outline of one segment and its stack. Each third tooth is "V-shaped" to approximate an arc.

Normally those areas are between two different materials or where, there are a large changes in the variables (Flux density, Field strength, etc).

Maxwell 2D from Ansoft was used in this work [48]. In spite of its huge materials library, it is necessary to add the properties of the steel sheets (*B*-*H* characteristic) of the stator and the properties of the magnets of the machine. The stator stack of the motor is

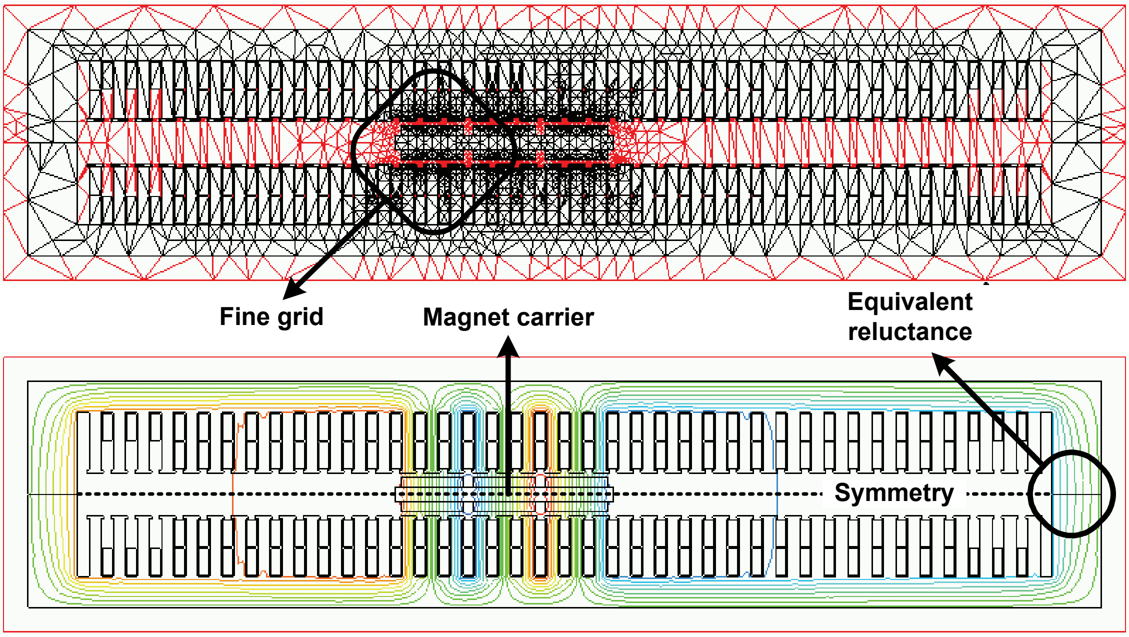

Figure 4.4: Mesh and Flux tubes of a segment without stator currents. The border conditions are according to an equivalent reluctance of the complete annulus

made from non oriented steel sheets, material type M470-50A with a thickness of 0,5 mm. The magnets are made up of Neodymium Iron Boron (NdFeB) N42, 1,33 T.

4.2.1. Linked flux

The 2-D magneto-static field simulator computes static magnetic field arising from DC currents and other sources like permanent magnets and external magnetic fields. Magnetic fields in both linear and nonlinear materials can be simulated. The simulator solves (19) for the magnetic vector potential, $\vec{A}(x,y)=\left(0,0,A_z(x,y)\right)$. Equation (19) is derived from the Ampere's law (appendix A.7).

$$\vec{J}(x,y)=\nabla\times\left(\frac{1}{\mu_r\mu_0}\left(\nabla\times\vec{A}(x,y)\right)\right) \tag{19}$$

In (19) $\vec{J}$ is the DC current density field flowing perpendicular to the *x-y* plane, $\vec{A}(x,y)$ is the magnetic vector potential, μ_r is the relative permeability of each material and μ_0 the permeability of vacuum. In general, both $\vec{J}$ and $\vec{A}$ are vectors. However, $\vec{J}$ is assumed to only have a *z*-component. A consequence of this is that $\vec{A}$ only has a *z*-component as well (appendix A.7) [48].

After $A_z(x,y)$ is computed, the magnetic flux density $\vec{B}$ and the magnetic field $\vec{H}$ can be computed using (20) and (21).

$$\vec{B}=\nabla\times\vec{A} \tag{20}$$

$$\vec{H}=\frac{\vec{B}}{\mu_r\mu_0} \tag{21}$$

The flux linkage Ψ for a winding is obtained from (22) and (23), where *s* is the area inside of the winding, ϕ is the flux and *N* is the number of turns.

$$\phi=\oint\vec{B}\cdot ds \tag{22}$$

$$\Psi=N\cdot\phi \tag{23}$$

In the motor of the set-up, the winding alignment between the double sided stator is made in the way that the flux linkage is complemented in the same phase and the phases are aligned (Figure 4.5). This allows connecting the windings of both sides of one segment electrically in parallel and fed them from one inverter. Due to this alignment of the winding, the flux tubes go from one side of the stator to the other side through the vehicle's magnet carrier (Figure 4.4), and close through the neighbor pole or through the

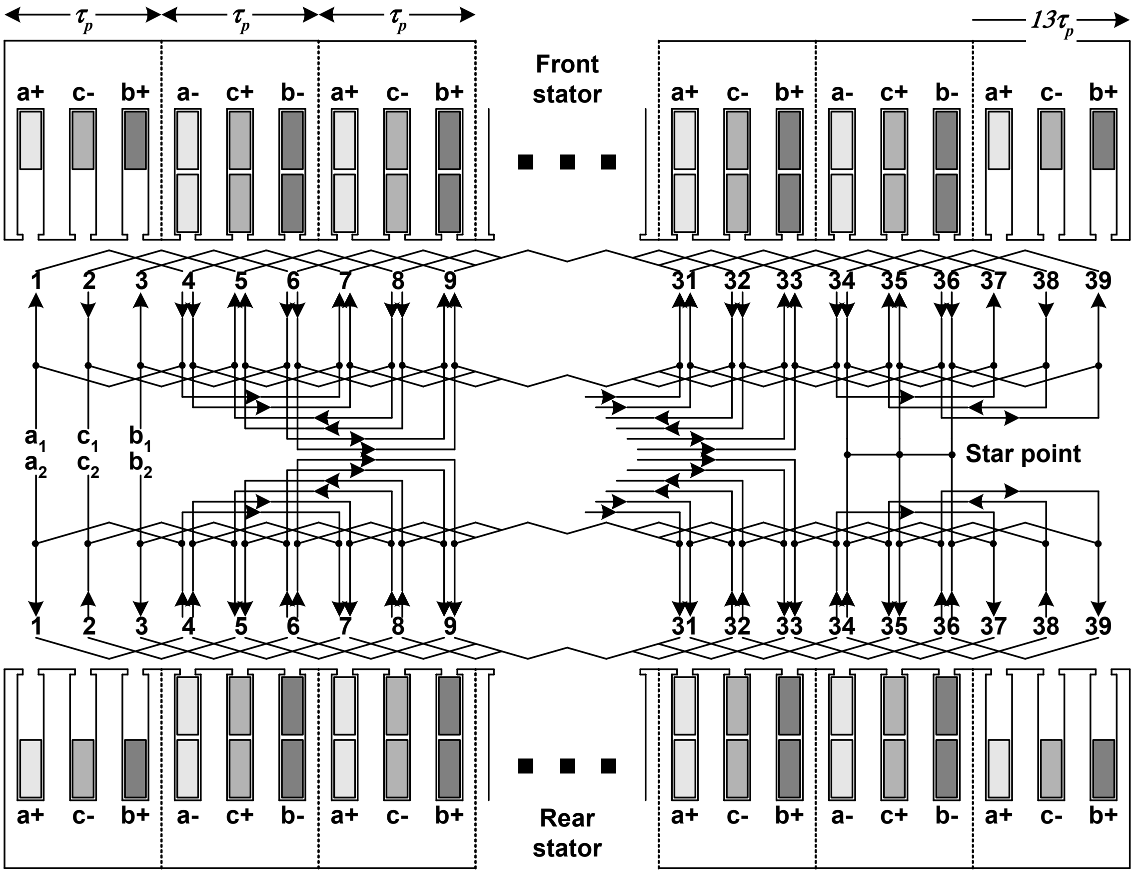

Figure 4.5: Windings distribution and connection for a double side segment

circular yoke of the machine. Due to the odd number of magnet poles at one side, the flux of one magnet will close through the large gap all around the annulus. But the field calculation can not be extended all over the annulus (length 3,1 m) due to computation complexity and time. Therefore, the inactive segments are simplified to an equivalent reluctance [49].

The simulation for the motor of the setup was done for a total of 7 pole pitches. Five poles are for positions when the magnet carrier travels between two consecutive segments. The other two poles are for positions when the magnet carrier is inside of a segment. At each pole, 50 different positions are calculated (i.e. 3,6°elec.), and for each position a total of 21 different currents i_q are used, covering the whole operation range. The current i_d is kept zero to reduce the number of static calculations. For each of these i_d-i_q values, the set of 3 stator currents i_a, i_b and i_c are calculated. A total of 21*50*7=7350 static 2D FEM calculations are necessary. The computing time of those simulations can take more than one week on a PC, depending of the computing power and the mesh.

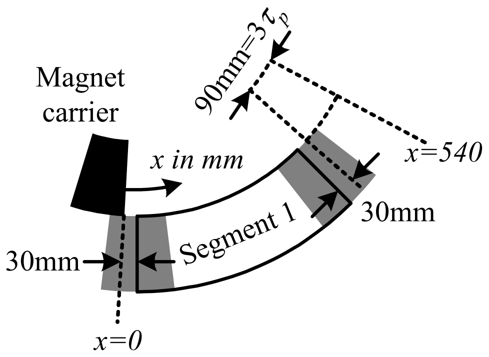

Figure 4.6: Position reference for a segment respect to the magnet carrier.

The FEM calculations delivers the linked fluxes and the inductances in three phase *abc* coordinate system as functions of the current $i_d=0$, i_q and the position x. All the calculations are transformed using (2) and (4) in *d-q* mover fixed coordinate system.

The periodicity property of the linked flux versus position allows to extrapolate it for the entire segment. At the position $x = 0$, the magnet carrier is completely outside of the segment, located one pole pitch (30 mm) in front of it (Figure 4.6). the extrapolation is extended to one pole pitch after the magnet carrier leaves the segment, at position $x = 540$ mm.

Figure 4.7 shows the fluxes Ψ_d^{FEM} and Ψ_q^{FEM} as function of the currents $i_d = 0$, i_q and the position x. Figure 4.7a shows the linked flux $\Psi_d^{FEM}(i_d = 0, i_q, x)$. Figure 4.7b shows

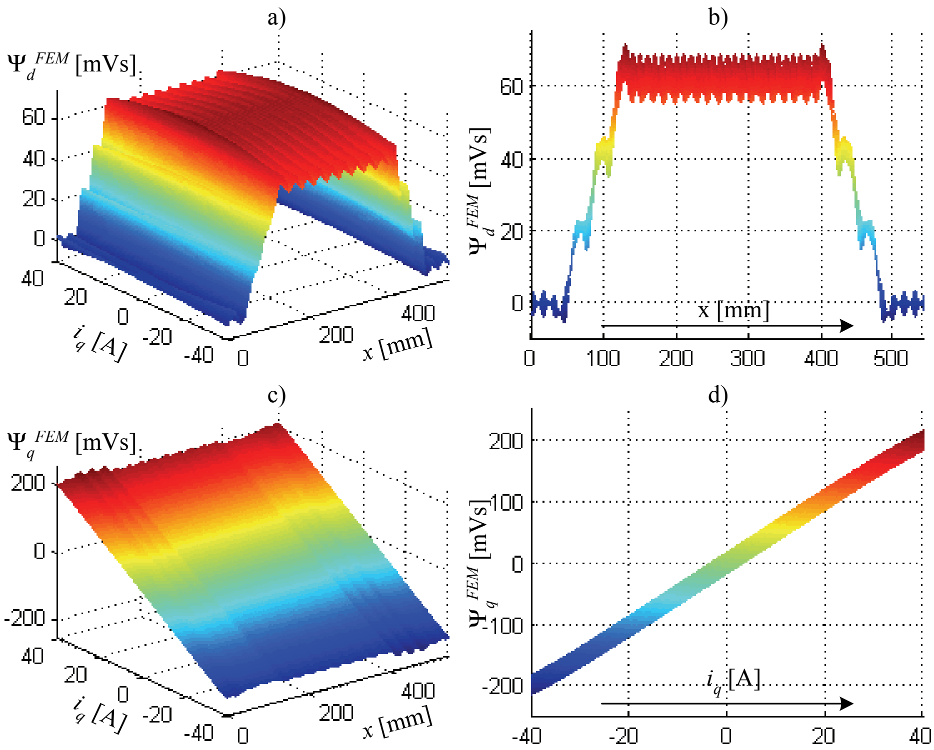

Figure 4.7: Fluxes $\Psi_d^{FEM}(i_d = 0, i_q, x)$ and $\Psi_q^{FEM}(i_d = 0, i_q, x)$ obtained with Maxwell 2D for a entire segment of the motor in the setup. a) flux $\Psi_d^{FEM}(i_d = 0, i_q, x)$, b) flux $\Psi_d^{FEM}(i_d = 0, i_q, x)$ in *x*-*z*-coordinate, c) flux $\Psi_q^{FEM}(i_d = 0, i_q, x)$ and d) $\Psi_q^{FEM}(i_d = 0, i_q, x)$ in *y*-*z*-coordinate.

the rising and falling of the flux Ψ_d^{FEM} in the x-z-coordinate (i.e. the position dependence) when the magnet carrier enters or leaves a segment. The flux Ψ_d^{FEM} is mainly dependent on the position x. Additionally position dependent harmonics can be observed too. Figure 4.7c shows the flux $\Psi_q^{FEM}(i_d = 0, i_q, x)$. it depends mainly on the current i_q (Figure 4.7d). Some position dependent harmonics can be observed too, specially when the magnet carrier enters or leaves a segment.

The case $i_d = 0$, $i_q = 0$ allows to verify the results of the FEM experimentally. In this way it is possible to calculate the speed normalized *EMF*, (12) and (13), and compare it with Figure 4.1. Figure 4.8 shows the comparison of the simulated and the measured *EMF*. The simulation presents more ripple in the d-axis than the measurement, due to many factors. First, the derivative of the linked flux with respect to the position $\partial\Psi_d/\partial x$ is higher than in the q-axis. Second, for each position the simulation forms a new mesh, and not necessary with the same number of elements. It produces a different solution

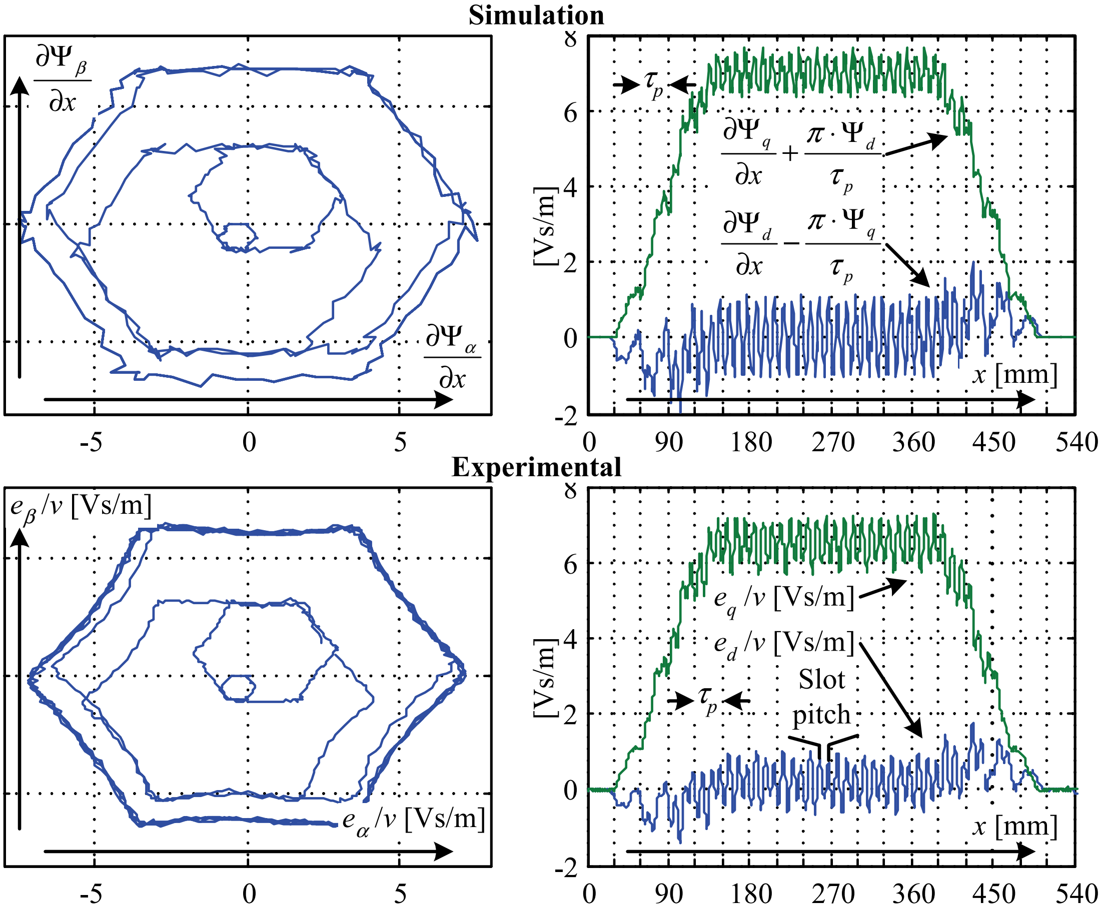

Figure 4.8: Comparison of the simulation for the case $i_d = 0$, $i_q = 0$ and the *EMF* measurement.

and a different accuracy. For other side, the simulation is done for the outer diameter of the annulus. That means the effect of the "V shaped" teeth are not modeled. The amplitude of e_q/v shows a small difference too, but, in general, the approximation of the simulation is very close to the real machine.

4.2.2. Electromagnetic force

To compute the force on an object, the solver uses the principle of virtual work. The force on an object in the direction of the displacement s is given by the relationship [48] (24).

$$F = \left.\frac{dW_c(i,s)}{ds}\right|_{i=const} = \frac{\partial}{\partial s}\left(\int_V \left(\int_0^H \vec{B}\cdot d\vec{H}\right)\cdot dV\right) \tag{24}$$

Where $W_c(i,s)$ is the magnetic co-energy of the system. The current i is held constant.

The simulation was done considering that the consecutive segments are fed with the same current i_q ($i_d = 0$). For the motor of the set-up, the magneto-motive force (*MMF*) weakens during the transition between two consecutive segments, like explained in section 3.1. The weakening in the *MMF* reduces the force of the motor in this region.

Figure 4.9a shows the calculated force $F_x^{FEM}(i_d = 0, i_q, x)$ for a complete segment, including when the magnet carrier goes to the next segment (fed with the same current). The weakening of the force at the end of the segment can be clearly identified. It reduces by 33% of the nominal force (Figure 4.9b). For the given winding distribution (motor of set-up, section 3.1), the reduction of force in the transition area (when the

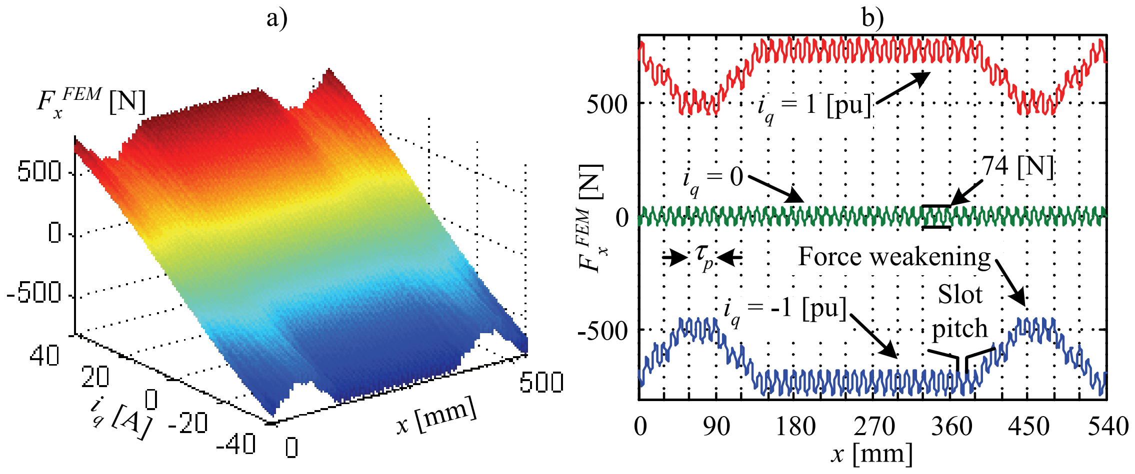

Figure 4.9: Force calculation for the modeled machine. A) $F_{x\text{-}FEM}(i_d = 0, i_q, x)$, b) $F_{x\text{-}FEM}$ for all position and for 3 given currents, 1pu = 40 A.

magnet carrier travels between two consecutive segments) depends on the number of poles of the magnet carrier, like in (25). For the motor of the set-up, the magnet carrier has only three poles, i.e. in the transition area, in the worst case, only one pole is facing the full *MMF* (two layer windings are filled). The other two poles are facing half (one layer winding is filled) of the *MMF*. Figure 4.9b shows the force F_x^{FEM} for three currents i_q = 1 pu, i_q = 0 and i_q = -1 pu. For current i_q = 0 the machine shows a force ripple (Figure 4.9b) with three periods in one pole pitch, i.e. the number of teeth. This force disturbance is cogging force and has a value of around 74 N peak to peak. (i.e. ≈10% of the nominal force).

$$F_{\max-trans} = 100 \cdot \left(1 - \frac{1}{P_{mc}}\right) \tag{25}$$

In (25), P_{mc} is the number of poles of the magnet carrier and $F_{\max\text{-}trans}$ is the maximal force in the transition area (when the vehicle moves across two segments) in percent.

To validate the force calculation from FEM, a static force measurement was done. Therefore, an adjustable screw is used to fix the machine together with the sensor at different positions within one pole pair (appendix A.8). For each position, a sequence of steps in the i_q currents from 0 to the nominal value were fed. Each step was applied for 500ms to guaranty a steady state force measurement.

Figure 4.10 shows the results of the force measurement interpolated with Matlab [17] in comparison with the simulation. Force ripple can be clearly identified, with a period of 1/3 of the pole pitch (i.e. slot pitch). This validates the slot harmonic in the force delivered by the FEM. At rated current, the FEM calculations delivers an average force of 730 N approximately, 50 N higher than the measured value (Figure 4.10b and Figure 4.10d), i.e. an error around 7,4%. The difference can be explained due to the simplifications in the model, especially because iron loses and eddy currents are not considered. The cogging force measured shows an amplitude of 28 N (Figure 4.10b), and the FEM calculation of 37 N. this difference is highly dependent of the air gap considered in the simulation. The cogging force reaches 4,2% of the rated thrust force.

From the comparison, it can be concluded, that the FEM simulation delivers an acceptable estimation of the force, following the shape as well as the magnitude of the thrust force.

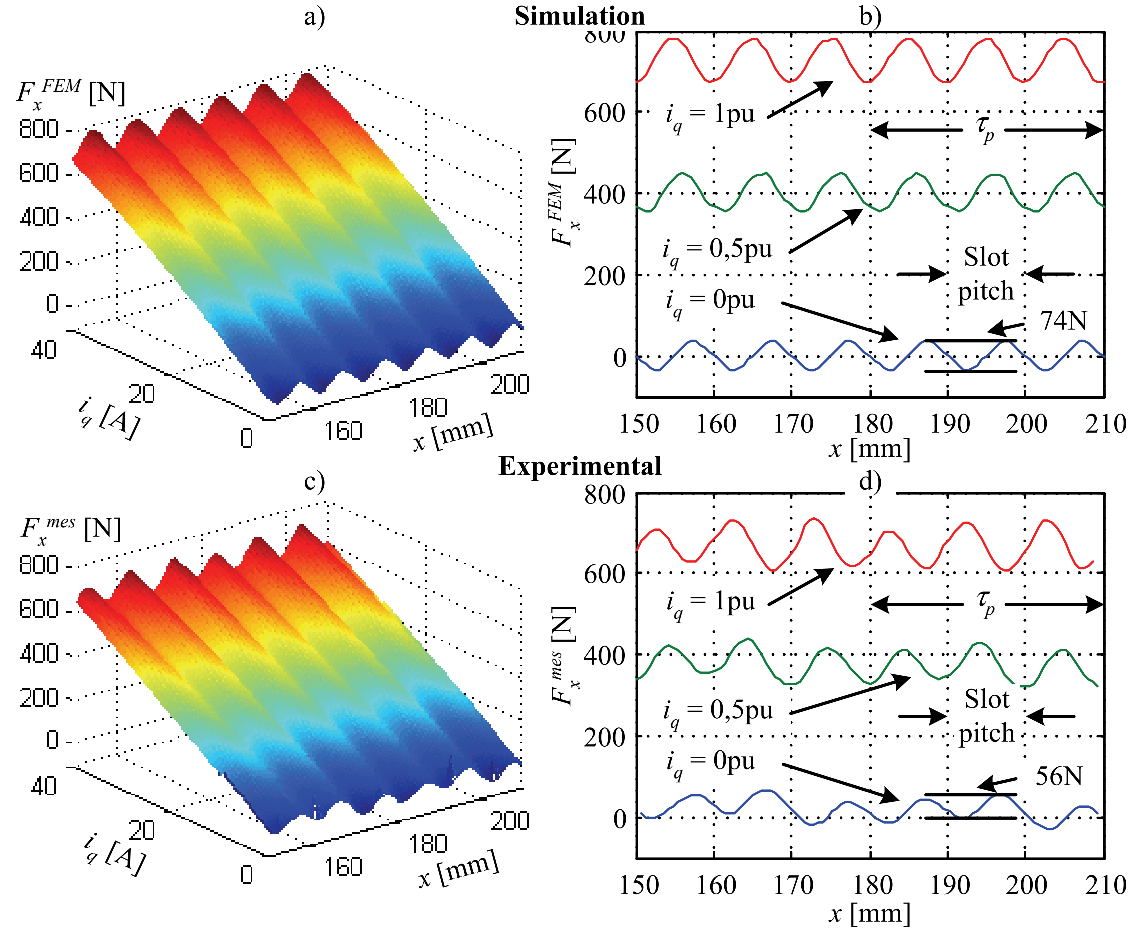

Figure 4.10: Comparison of the FEM calculated force and the static force measurement over one pole pair. a) and b) simulation, c) and d) experimental measurement.

4.2.3. Inductance

At the simplest level, inductance represents how much energy is stored in the magnetic field when current flows (26).

$$W_m = \frac{1}{2} L i^2 \tag{26}$$

In (26), W_m is the energy stored in the magnetic field, L is the inductance and i is the current flowing in the system.

In electric machines, iron is the typical material used to conduct magnetic flux. Iron has a nonlinear *B-H* characteristic. Because of this nonlinear feature, two kinds of inductance must be distinguished: differential and secant inductance. The secant inductance is the ratio of the total flux to current. The differential inductance is the ratio of the flux change and change of the exciting current.

The Maxwell 2D computes secant inductances (27) associated with a structure by simulating the magnetic field which arises when various voltages and currents are applied. Then, by computing the energy stored in those fields, it can then compute the necessary inductances [48].

$$\vec{\Psi}_{abc} = \begin{bmatrix} L_{aa} & L_{ab} & L_{ac} \\ L_{ba} & L_{bb} & L_{bc} \\ L_{ca} & L_{cb} & L_{cc} \end{bmatrix} \cdot \vec{i}_{abc} + \vec{\Psi}_{abc0}(x) \tag{27}$$

To compute inductances using this method, the B-field and H-field associated with the distribution of currents must first be computed. The magneto-static field simulator, which computes the magnetic vector potential at all points in the problem region, performs this task.

To compute an inductance matrix, the software performs a sequence of magneto-static field simulations. In each field simulation, one ampere is allowed to flow in a single conductor (coil). No current flows in any other conductor (coil). For an n-conductor (coils) system, n field simulations are automatically performed. The energy stored in the magnetic field that couples two conductors (coils) is given by (28).

$$W_{jk} = \frac{1}{2} L_{jk} i_j^2 = \frac{1}{2} \int_{\Omega} \vec{B}_j \cdot \vec{H}_k d\Omega \tag{28}$$

In (28), W_{jk} is the energy stored in the magnetic field linking the conductor j and k (coil j and k), i_j is the current in conductor j, $\vec{B}_j$ is the magnetic flux density produced by conductor j (coil j) and $\vec{H}_k$ is the magnetic field to which the conductor k (coil k) is exposed. For a coil with n turns, the total value of the inductance L_{total} is obtained from (29).

$$L_{total} = n^2 \cdot L \tag{29}$$

In segmented Long-stator LPMSM exists the case that the magnet carrier is outside of the segment, i.e. it is equivalent for a rotative machine to have a stator without the rotor. Figure 4.11a shows the inductance $L_{dd}^{FEM}(i_d = 0, i_q, x)$. The inductance increases when the magnet carrier enters in the segment (the reluctance reduces). Then, it reaches the maximum value, and when the magnet carrier leaves the segment, L_{dd}^{FEM} decreases again (Figure 4.11b). The variation of the inductance L_{dd}^{FEM} (magnet carrier outside vs.

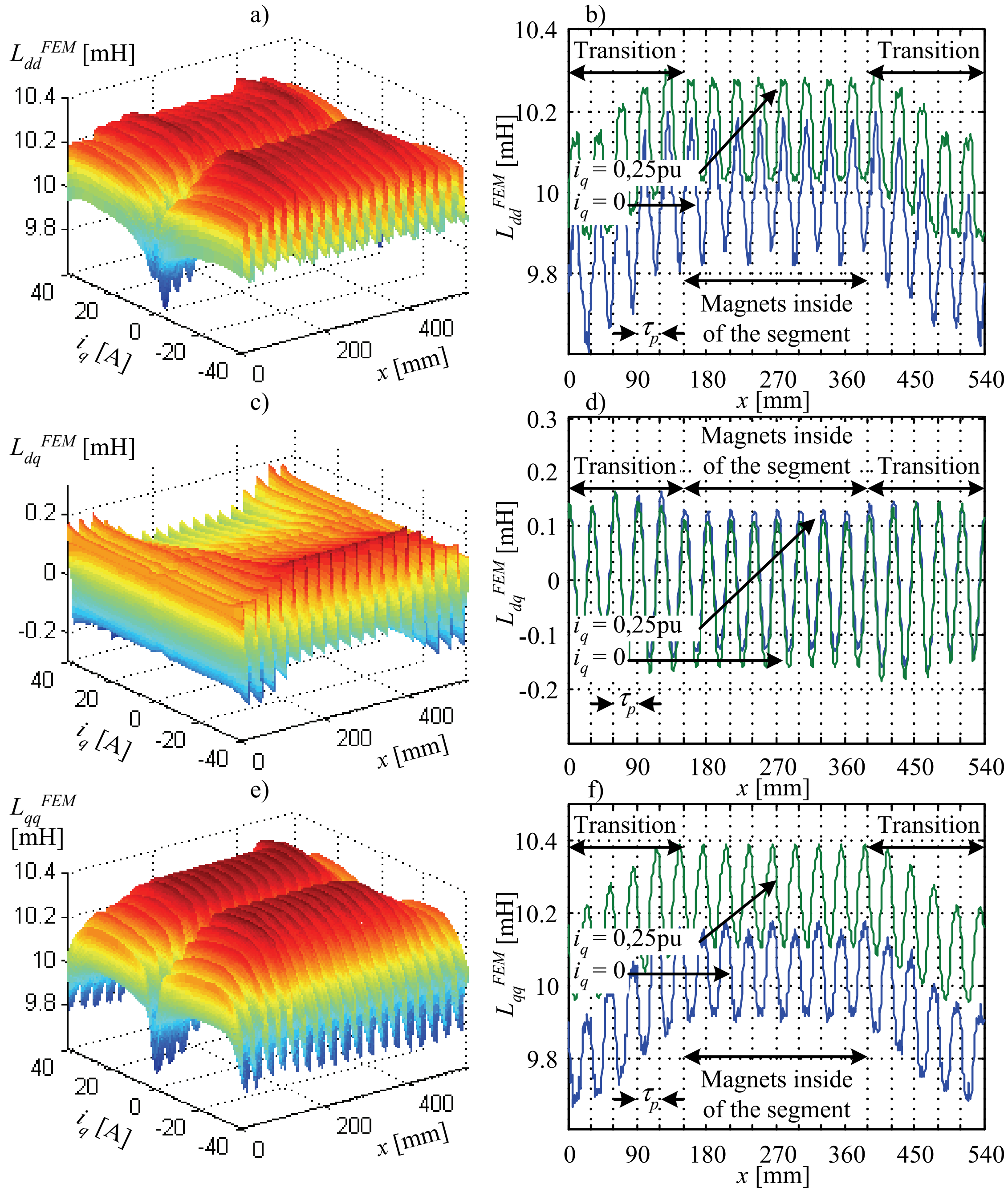

Figure 4.11: Inductances in *d*-*q* coordinate system obtained by FEM. a) $L_{dd}^{FEM}(i_d = 0, i_q, x)$, b) L_{dd}^{FEM} for $i_q = 0$ and $i_q = 0{,}25$ pu, c) $L_{dq}^{FEM}(i_d = 0, i_q, x)$, d) L_{dq}^{FEM} for $i_q = 0$ and $i_q = 0{,}25$ pu, e) $L_{qq}^{FEM}(i_d = 0, i_q, x)$, f) L_{dq}^{FEM} for $i_q = 0$ and $i_q = 0{,}25$ pu.

magnet carrier inside) is not larger then a 2%. The small variation of the inductance is explained by the short length of the magnet carrier and the large air gap of the motor. In the experimental machine, the magnet carrier covers only 23% of the segment's length (3 magnet poles and 13 stator poles in the segment). The air gap of the motor is 2 mm and the height of the magnet is 4mm. Furthermore, the inductance shows a ripple, which is the effect of the magnet motion across the teeth and changing its saturation level, i.e. the total inductance. The inductance shows a period of one pole pitch with a variation of 0,3 mH peak to peak. The inductance L_{dd}^{FEM} is not much affected by saturation produced by the current i_q, the saturation affects mainly its own axis.

In general, a magnet carrier with more poles (shorter as the stator segment to keep the concept of the long stator LPMSM) and a motor with less air gap will produce a higher variation in the inductances.

Figure 4.11c shows the mutual inductance between both axes, *d-q*. For ideal rotative machines, the mutual inductance between phases L_{dq}^{FEM} is zero. Due to the end effect of the windings in a linear motor, the mutual inductance is not zero (Figure 4.11c-d).

The inductance $L_{qq}^{FEM}(i_d = 0, i_q, x)$ shown in Figure 4.11e is more affected by the current i_q than L_{dd}^{FEM}. The current i_q saturates the iron in its own axis direction, which reduces the inductance for high current. Figure 4.11f shows the inductance L_{qq}^{FEM} for 2 cases. For current zero, the inductance L_{qq}^{FEM} presents a value around 10,05 mH. For a 25% of the rated current, the inductance increases to 10,25 mH. This may be explained by an increased permeability of the iron for $i > 0$. The inductance L_{qq}^{FEM} has also a ripple. It has a period of one pole pitch with a variation of 0,25 mH peak to peak.

To validate the inductances, an experiment was carried out. A sequence of voltage steps u_q were applied by the inverter and the current i_q was measured. Then, the time constant and the relation between voltage and current was obtained. This resulted in an inductance L_{qq} of 12,5 mH for one stator segment (rear only). This experiment doesn’t consider saturations and voltage deviations produced by the inverter (reference and actual value). The difference between measured and simulated values (2,25 mH approximately) is mainly due to the winding overhang. The winding overhang adds a constant inductance to the system, but this doesn’t change the shape in Figure 4.11. Additionally, due to the construction of the machine, the magnets length is 80mm and the stator depth covered by the magnets is only 60mm. This produces a leakage inductance due to the overhang.

5. Control

The main goal of the control discussed in this dissertation is to compensate the force oscillations and disturbances in segmented long stator LPMSM to achieve a smooth motion. Three kinds of control structures are tested and compared, field oriented control using feed forward quantities from FEM [50], direct flux control [6][51] using flux tables from FEM as feedback and resonant control method [51]. Field oriented control is today a standard used in electric drives. On the other hand, direct flux control is a variant of direct torque control which offers a better dynamics as field oriented control. The resonant control variant is an alternative to suppress certain ripple frequency, without requiring specific information of the system.

5.1. Field oriented control

Cascade control structure (force/current, speed, position) is the classical method used to control rotative machines [13][22][39][40][43] as well as standard linear motors. For segmented long stator LPMSM the same structure can be used but with some added features, especially in the transition area (i.e. when the vehicle moves across two consecutive segments). In real applications, the cascade control structure presents important advantages in comparison to other methods (state space control, expert control, fuzy control, etc.). In commissioning for example, with the cascade control is possible first to stabilize and tune the inner control loop. The superimposed control loops can be tuned step by step, limiting the reference values for the next inner control loop. Saturation and other nonlinearities can be easily counteract by introducing feed-forward information to the control loop. As disadvantages of the cascade control structure, a reduced dynamic through the superimposing should be mentioned, where the dynamic of the outer loop must be slower as the inner loop.

The control equipment and control block diagram of the experimental setup is presented in chapter 3. All control actions in the experimental setup are performed by a standard PC (Celeron, 700 MHz) running under Linux RTAI. The hardware and physical components were explained in chapter 3. The control software is divided mainly into two interrupt service routines that are triggered by hardware signals from the respective “Vehicle Controller Interface” (VCI). The VCI issues this trigger signal at the cycle of the “Inverter Bus” where it receives the measured currents from the associated inverter interface.

Although the digital controller is used, the design and tuning of the controllers is performed using the theory of linear control system. The controllers are discretized using the bilinear transformation given by (30). The choice of the sampling time is therefore

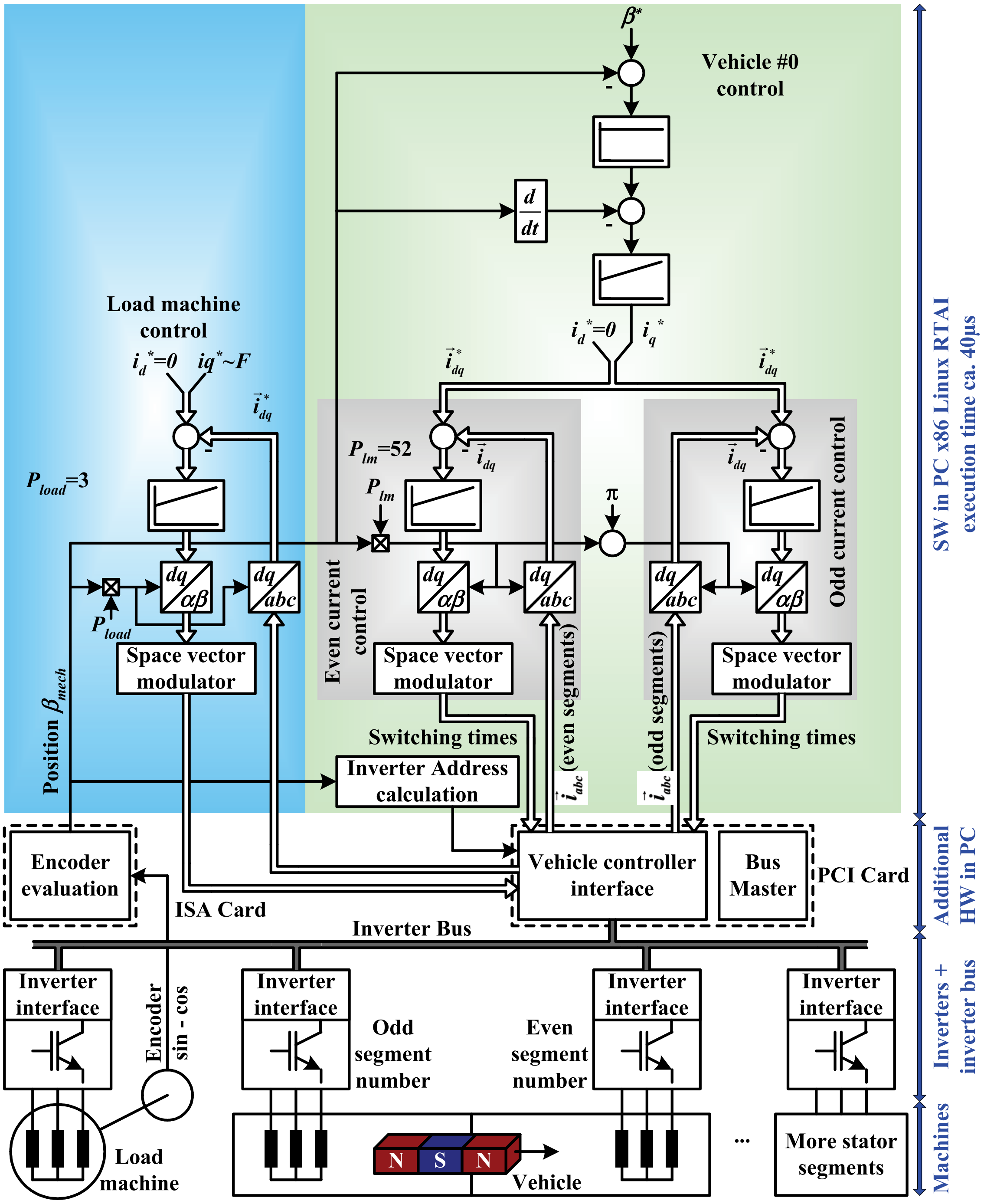

Figure 5.1: Hardware and software block diagram of the setup. Field oriented control structure.

important. In general, transformation of continuous time controller using approximations will lead to quite short sampling periods. In the experimental set-up, the sampling period is 60 times smaller than the electric time constant, i.e. it allows to use the transformation given by (30). Digital design methods, which allows longer sampling times, are not discussed in this dissertation [41].

$$s = \frac{2(z-1)}{T_s(z+1)} \tag{30}$$

As long as the vehicle covers only one stator segment, either the even or the odd current controllers are active exclusively (Figure 5.1). This is decided by the block “inverter address calculation”, depending on the position of the vehicle. Shortly before the vehicle enters the transition area (one pole pair, i.e. 60mm), the current control of the next stator segment is also activated. Then, in both stator segments the same q-axis currents are injected. It produces the thrust force profile like in Figure 4.9. The Phase of the electrical angle for two consecutive segments is shifted by 180° (one pole) to consider the odd number of poles per segment.

The position reference x = 0 in the set-up machine is set one pole pitch τ_p (i.e. 30 mm) before entering segment 1 (Figure 5.2). Two consecutive segments are active

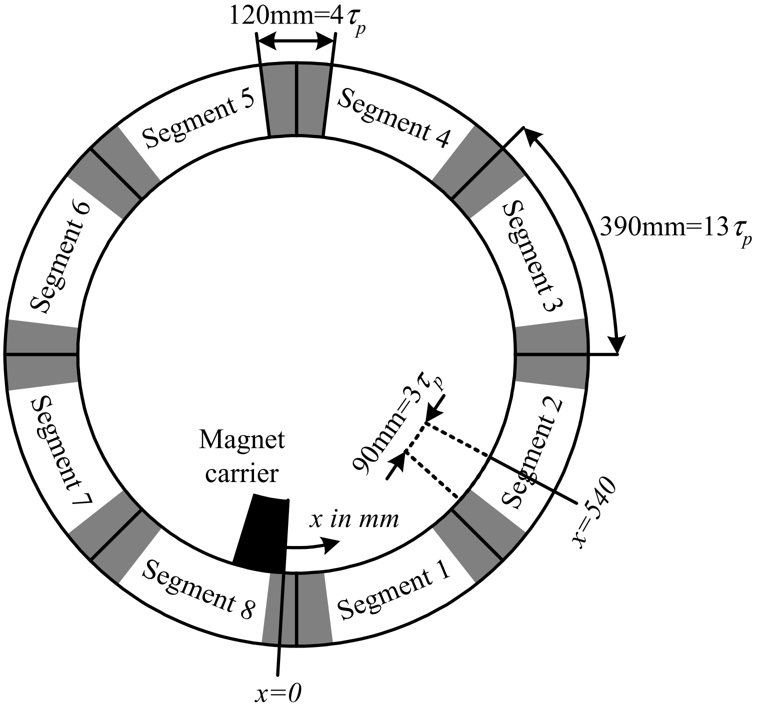

Figure 5.2: Segment activation and position for the set-up machine.

for a total motion of 210 mm.

The cascade control structure for the segmented Long-Stator LPMSM shown in Figure 5.1 is a standard superimposed position-speed-current control loop that is not optimal concerning force disturbances. The force weakening in the transition area, force ripple and cogging force are not well compensated. Experimental results are shown in the next section.

5.1.1. PI current control

Figure 5.3 shows the simplified current control loop of one axis of a PMSM using a PI controller, where the coupling inductances between the *d-q* axis were neglected. The control's time delay (included inverter reaction time) is modeled as a first order lag element with a time constant $T_D = 1{,}5T_s$ where T_s is the sampling time [14]. The converter gain k_c is the relation between the numerical evaluation in the computer (digital controller) and the real output voltage. In this case the resolution scale used was 4000 (12 bits) for the complete line to line voltage (2/3 DC-Link voltage). Then, k_c is obtained from (31). $k_{elec} = 1/R$ and $T_{elec} = L_{qq}/R$ are the electrical gain and the electrical time constant of the motor respectively.

$$k_c = \frac{{}^2\!/_3 \cdot u_{dc}}{4000} = \frac{1}{10} \qquad \text{for } u_{dc}\text{=600 V} \tag{31}$$

The PI controller can be tuned using the criteria of amplitude optimum [13][40]. Then, the controller coefficients are given by (32) and (33) (Appendix A.4).

$$T_i = T_{elec} \tag{32}$$

$$k_p = \frac{L_{qq}}{2 \cdot k_c \cdot T_D} \tag{33}$$

The transfer function of the closed current loop is given by (34). The bandwidth of

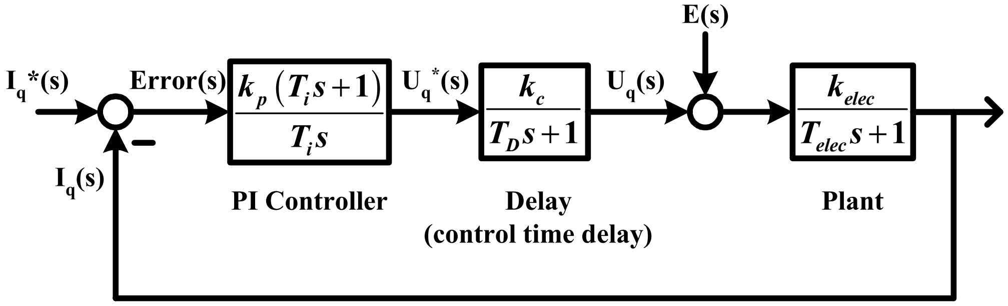

Figure 5.3: Simplified current control loop

the current control loop for small signal, with a sampling time T_s of 100 µs, reaches approximately 750 Hz.

$$Lc(s)=\frac{1}{2T_D^2s^2+2T_Ds+1}\approx\frac{1}{T_{eq}s+1} \qquad \text{with } T_{eq}=2T_D \tag{34}$$

When the mover enters a new segment with some speed, the induced voltage in this segment rises from zero to its final value within 4 pole pitches. Likewise, in the previous segment it decreases. Additionally, during this transition, the *EMF* in the three phases is unbalanced. If the speed is high, the change of the *EMF* magnitude is fast and may be approximated by a ramp. This ramp is a disturbance for the current control loop. A PI current controller cannot completely compensate a ramp type disturbance. Therefore, an alternative to improve the control loop is to use feed forward quantities according the reconstruction of the voltage model of the motor (7) [49], based on the tables obtained by FEM in the previous section.

5.1.2. Feed forward in the current control loop

Figure 5.4 shows the current controller for one segment, including the *EMF* feed forward model based on FEM tables, for the special case of current reference zero.

To avoid instability and large oscillations in the closed loop, the gain of the PI controller must be reduced and also it is recommended to delay the current reference value

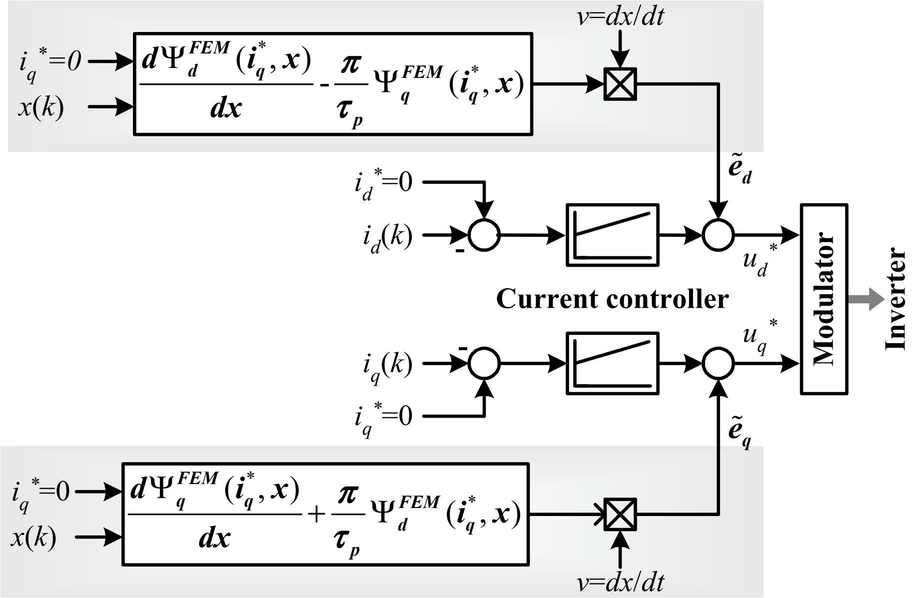

Figure 5.4: Current control loop with feed forward based on FEM. Particular case $i_q^* = 0$.

by one sample time [42][52].

The derivative of the linked flux with respect to the position $d\Psi_d^{FEM}/dx$ and $d\Psi_q^{FEM}/dx$ introduces information about the field harmonics in the air gap. For a pure sinusoidal *EMF* those derivatives are zero. Figure 5.5a shows the derivative of the linked flux with respect to the position Ψ_d^{FEM}/dx for current $i_d = 0$ and for all currents i_q inside of the rated range. It shows an important disturbance for $x < 150$ mm and $x > 390$ mm, i.e. when the magnet carrier enters and leaves the segment. In Figure 5.5b, $d\Psi_d^{FEM}/dx$ can be appreciated for current i_d and i_q zero, which presents disturbances with a peak of more than 1.5 mVs/m. These disturbances represents only a 0.23% of the normalized *EMF* of the motor, but with a higher frequency (Figure 4.1). When the vehicle is completely inside of the segment (150 mm < x < 390 mm), the position derivative of the linked flux oscillates with a period of a slot pitch and shows an amplitude of 0.5 mVs/m in the d-axis. The q-axis shows a smaller amplitude as the d-axis with an

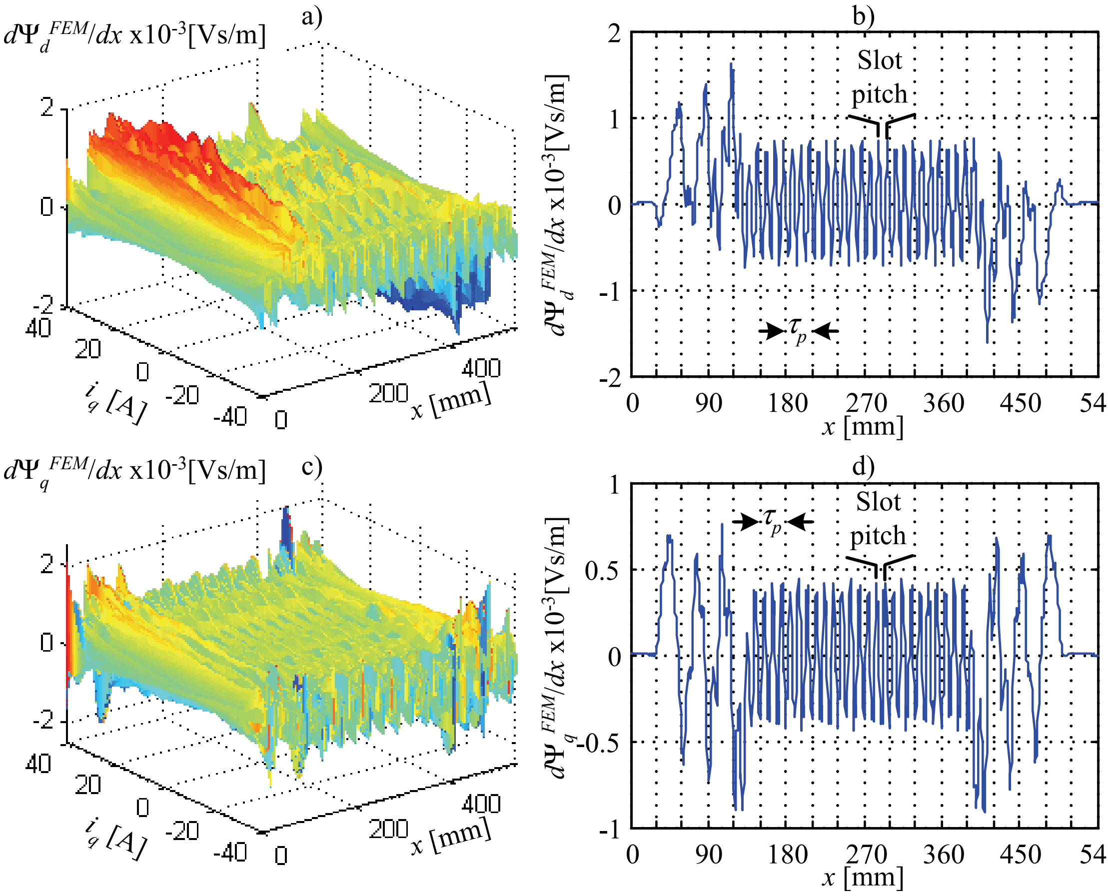

Figure 5.5: Derivative of the linked flux respect to the position. a) $d\Psi_d^{FEM}/dx$, b) $d\Psi_d^{FEM}/dx$ for current i_q zero, c) $d\Psi_q^{FEM}/dx$, and d) $d\Psi_q^{FEM}/dx$ for i_q zero.

amplitude of 0.35 mVs/m. The magnets are aligned with the *d*-axis, which saturates and affects directly its own axis. $d\Psi_d^{FEM}/dx$ and $d\Psi_q^{FEM}/dx$ don't show an important dependence on the currents.

In order to analyze the behavior of the current controller, the linear machine is moved at constant speed $v = 3.12$ m/s (one turn of the annulus per second) by the load machine. This results in 1730 samples in 540 mm, i.e. 9 pole pairs. The reference current i_d^* and i_q^* is set to zero. Then, the controller must only reject the *EMF* disturbance.

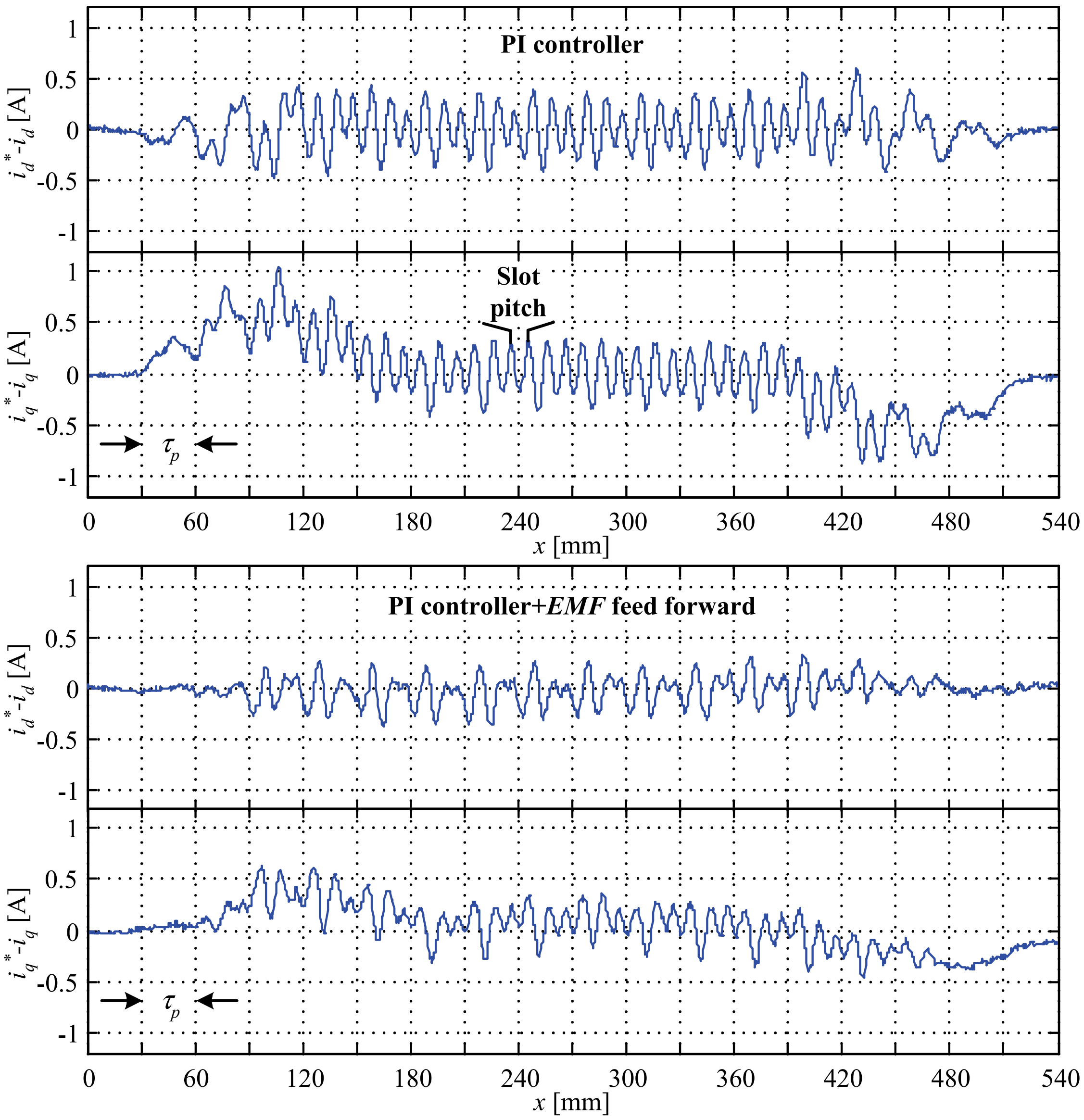

Figure 5.6: Experimental measurement of the sampled current deviation i_d^*-i_d and i_q^*-i_q with PI controller and with PI controller+*EMF* feed-forward. Experiment carried out at reference current i_d and i_q zero and constant speed 3.12 m/s, i.e. a total of 1730 samples in 540 mm (T_s = 100 µs).

For the close loop current control, the PI current controller without feed forward has difficulties to keep the *q*-axis current at its reference value (Figure 5.6), especially when the mover enters the new stator segment and generates a ramp-type *EMF* disturbance (Figure 4.8b-d). When the magnet carrier moves in the middle of the segment, slot harmonics generate disturbances, which also can not be fully compensated by the PI current controller. Figure 5.6 shows the current deviation i_d^*-i_d and i_q^*-i_q using the current control structure of Figure 5.4 (feed forward). In this case, the controller nearly does not counteract against the disturbances. The feed forward calculated by FEM reduces the current deviation when the mover enters the new stator segment as well as the deviations caused by slot harmonics.

The control loop with feed forward does not suppress totally the slot harmonics in the current i_d and i_q (Figure 5.6). In the experimental machine each third tooth is V-shaped in order to approximate the circle by a polygon. From this, each third tooth is very narrow at the inner circumference and will be much higher saturated than in the simulation, where all teeth have identical dimensions. This results in an inaccurate model.

The dynamic response of the current controller can be also improved using differential inductance tables obtained from FEM simulations. For the control loop in Figure 5.7 only L_{dq}^{diff} and L_{qq}^{diff} are necessary, under the assumption that the current i_d is equal to zero. Then the amount of voltage which is necessary to change the currents within one sampling interval to the commanded set-point value can be calculated from (7). L_{dq}^{diff} and L_{qq}^{diff} are calculated from (10), and simplified to (35) and (36) (for current i_d equal to zero).

$$L_{dq}^{diff} = \frac{\partial L_{dq}}{\partial i_q} \cdot i_q + L_{dq} \tag{35}$$

$$L_{qq}^{diff} = \frac{\partial L_{qq}}{\partial i_q} \cdot i_q + L_{qq} \tag{36}$$

Figure 5.8 shows the evaluation of (35) and (36) according the FEM simulations for the inductances L_{dq}^{FEM} and L_{qq}^{FEM}. Now, these tables are used for the control loop as shown Figure 5.7.

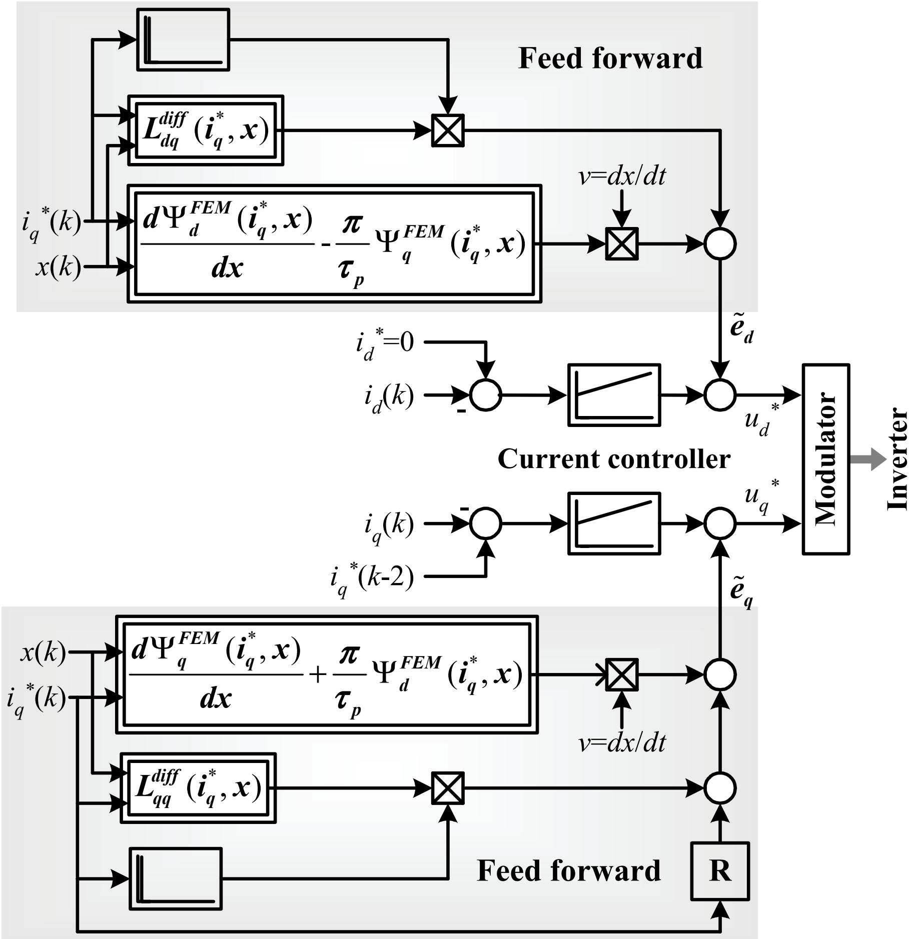

Figure 5.7: Current feed forward control structure based on FEM simulations

The derivative of the current in the voltage model is highly sensitive to the quality of the current measurement. For this reason, a low pass filter is necessary (not shown in Figure 5.7). This will limit the dynamic of the voltage model. The feed forward model uses the current reference value i_q^* and the actual position x as input variables.

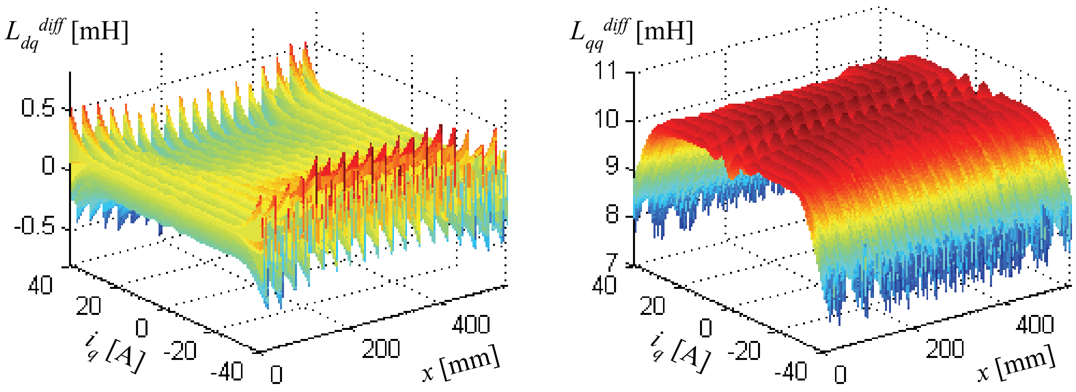

Figure 5.8: Differential inductances calculated from the FEM.

A new experiment is carried out in order to analyze the dynamics of the current controller. The linear machine is moved at constant speed $v = 3.12$ m/s by the load machine. This results in 1730 samples in 540 mm, i.e. 9 pole pairs. Figure 5.9 shows the current deviation for a change of 10 A in the reference current i_q^* at the position $x = 180$ mm. For the PI controller without feed forward, the coupling component L_{dq}^{diff} in the d-axis introduces a disturbance that is not compensated (Figure 5.9a). In this case, a PI controller with feed forward presents an important advantage. In the q-axis, the PI controller with feed forward (Figure 5.9b) presents a better slot-pitch oscillation rejection.

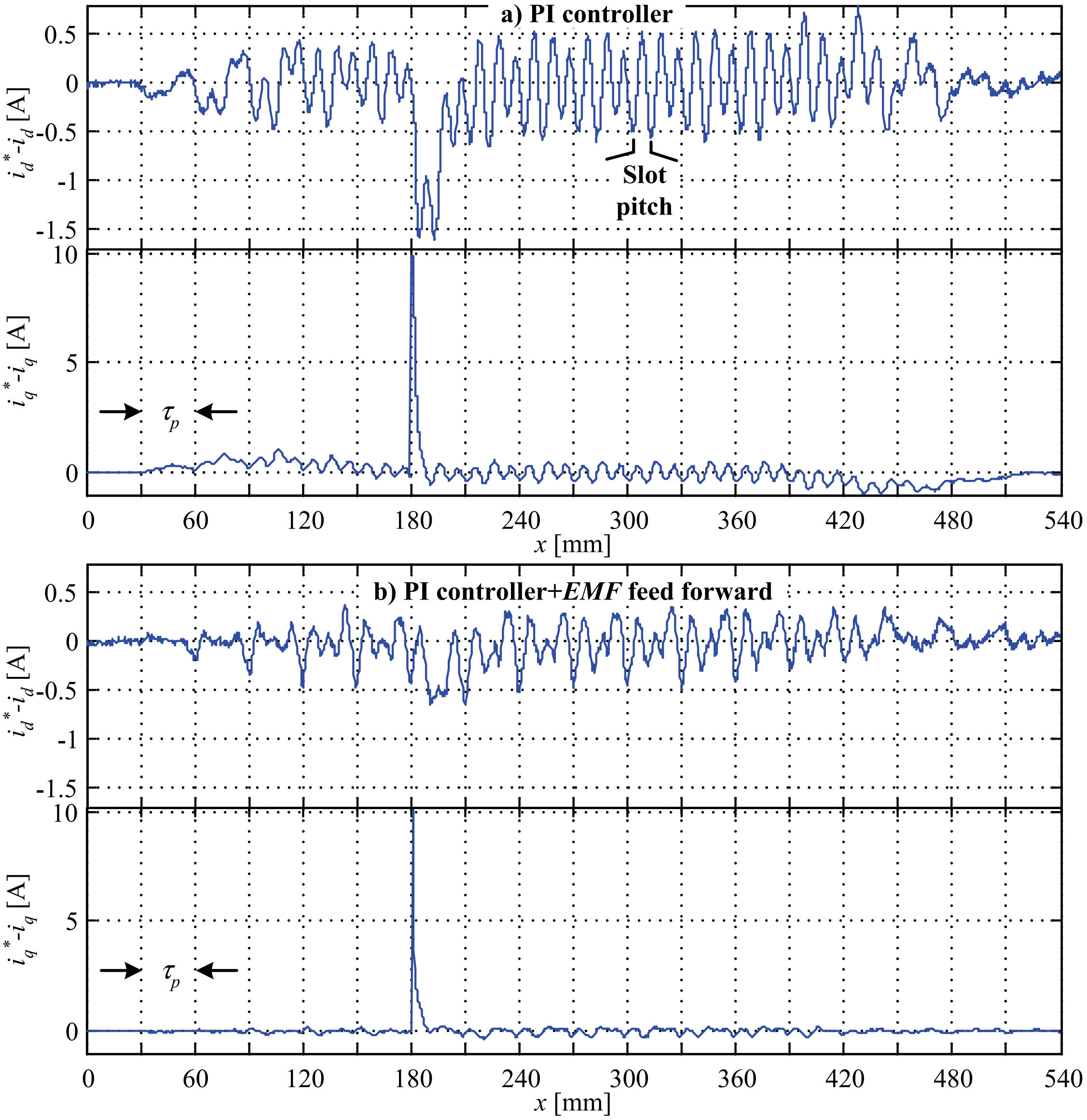

Figure 5.9: Experimental measurement of the sampled current deviation i_d^*-i_d and i_q^*-i_q for a step in i_q^* of 0,125 pu with a) c) PI controller and with b) d) PI controller+*EMF* feed-forward. Experiment carried out at constant speed 3,12 m/s, i.e. a total of 1730 samples in 540 mm.

5.1.3. Force control

Different kinds of force disturbances were identified in the model of the machine in section 4.1, like ripple force (current dependent), cogging force (current independent) and force weakening when the magnet carrier moves between to consecutive segments. Until now, the feed-forward current control introduced in the previous section aims to improve the tracking of the current reference, which is a necessary condition to reject force harmonics (current dependent and independent). The main approach of suppressing undesired force ripple is to inject appropriate currents in the LPMSM by using various techniques.

A PI force (torque) controller which is superimposed to the current controller was analyzed in [39]. The force (torque) feedback is obtained from a model or from tables representing the force-current characteristic of the motor. As an alternative to the PI force controller, a force-current characteristic can be used as feed-forward. This avoids a superimposed force controller that introduces a new dynamics. Figure 5.10 shows both alternatives for the segmented long stator LPMSM. Depending on the position of S_1, a closed loop PI force controller or a feed-forward force-current characteristic can be activated. For the closed loop force control, the force feedback is obtained from the FEM tables (Figure 4.9).

In Figure 5.10, when the vehicle is at the position x = -30 mm, the next segment is activated through the address calculator block, and the force reference F_x^* (current i_q^*) is set to the same value as in the previous segment. This produces a current i_q in the next segment that presently does not produce any force, but the reference value must be reached before the vehicle enters the new segment. For this reason each segment has its own tables in the control structure of Figure 5.10. For positions between –30 mm and 180 mm both segments are active.

The “$F_x^{FEM}(i_q,x)$ table” in Figure 5.10 receives as input the position x and the (actual) current i_q of the even (or odd) segment. The periodicity of the force profile (0-390 mm) for one segment allows to extrapolate the force behavior to the complete annulus using the “relative position” calculator (Figure 5.10). Additionally, the force table F_x^{FEM} was calculated assuming both consecutive segments fed with the same current i_q.

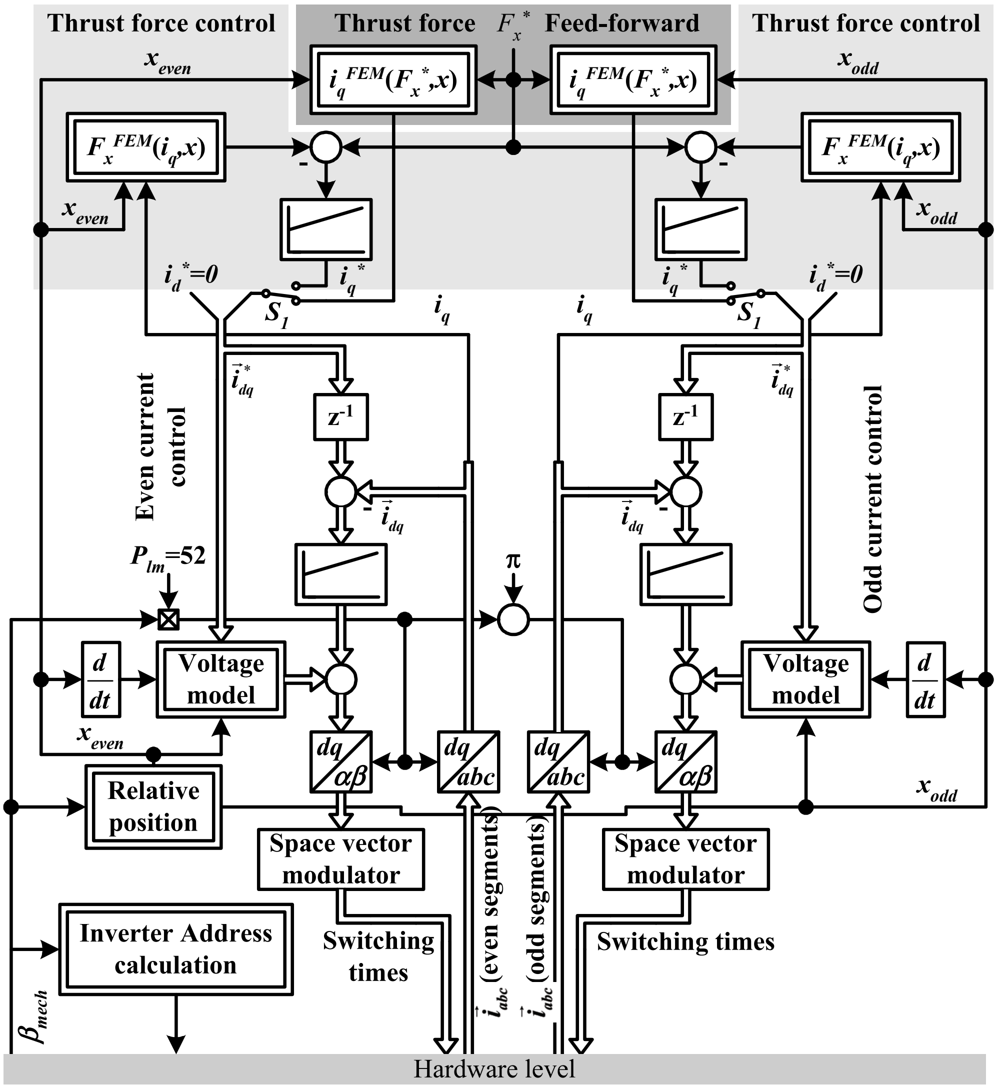

Figure 5.10: Alternatives: Force controller or current feed forward, selected by S_1

The feed-forward function $i_q(F_x^*,x)$ is obtained from the FEM force tables and it is shown in Figure 5.11. The force range for the feed-forward table is restricted from -440 N to 440 N. This range results in a maximum current of $|i_q| = 40$ A in the transition area, without exceeding the rated current of the motor (≈ 40 A). Figure 5.11b shows, that harmonic currents in i_q are necessary in order to generate a constant force. The period of the harmonic currents is one slot pitch. The additional current necessary in the transition area can be observed clearly for positions $0 < x < 150$ mm and $390 \text{ mm} < x < 540$ mm.

The PI force controller is tuned considering the inner current control loop as a first order lag element with an equivalent time constant T_{eq} (34). The force control loop can

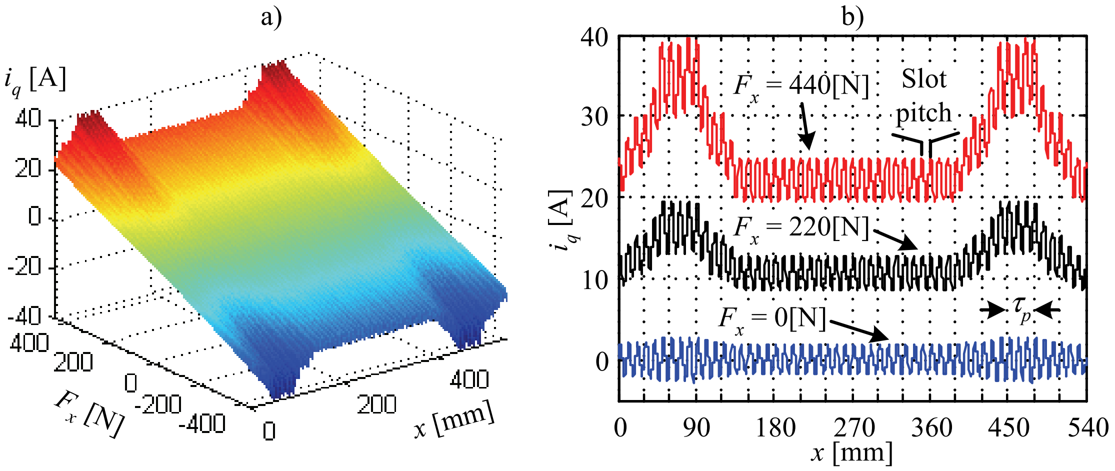

Figure 5.11: Current feed-forward for the segmented linear motor obtained by FEM.

be strongly simplified as shown in Figure 5.12. The amplitude optimum (AO) is used to tune the controller parameters k_p (38) and T_i (37) (appendix A.5).

$$T_i = \frac{\sqrt{2} \cdot T_{eq}\omega_c - 1}{T_{eq}\omega_c^2} \tag{37}$$

$$k_p = \frac{\sqrt{2} \cdot T_{eq}\omega_c - 1}{k_f} \tag{38}$$

In (37) and (38) ω_c is the desired cut-off frequency of the close loop, and it must be smaller as $1/\sqrt{2}T_D$, where $1/\sqrt{2}T_D$ is the cut-off frequency of the current control loop (section 5.1.1).

To analyze the behavior of the force control, the linear machine is moved at constant speed v = 1,56 m/s (half turn to the annulus per second) by the load machine. A force step from 200 N to 240 N (linear region) is applied to the linear motor at position x = 240 mm. Figure 5.13 shows the calculated force $F_x^{FEM}(i_q,x)$ ($F_x^{FEM}(i_q,x)$ is a calculated quantity whereas i_q and x are obtained from measurement) for two different values of ω_c, one with the same bandwidth as the current controller, i.e. $\omega_c = 1/\sqrt{2}T_D$ (Figure

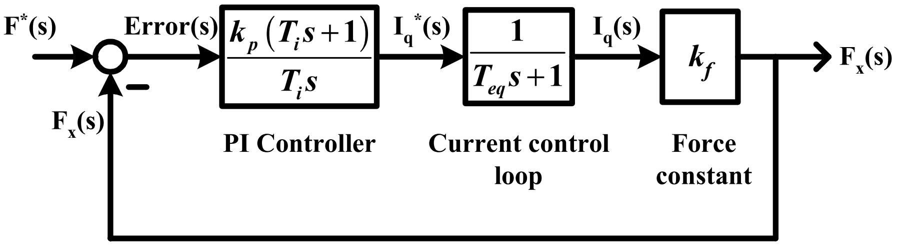

Figure 5.12: Simplified thrust force control loop.

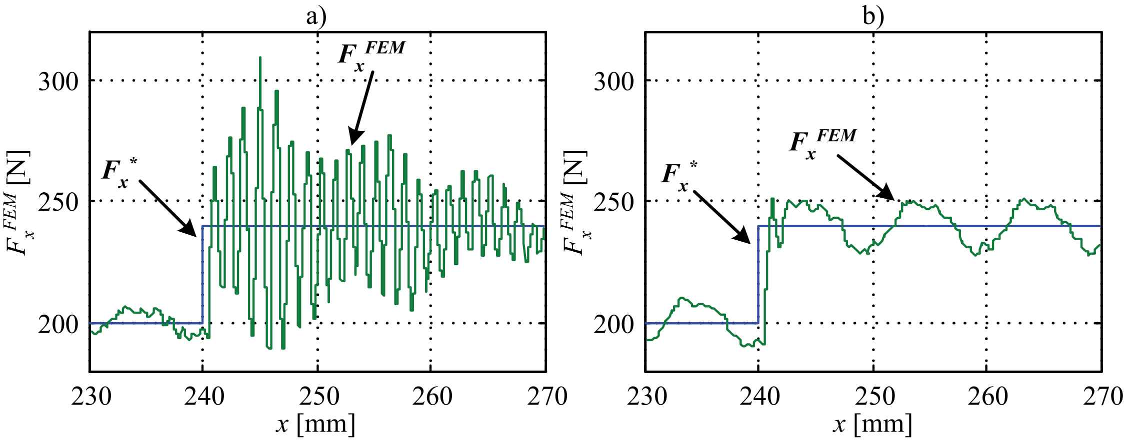

Figure 5.13: Step of 40 N at position $x = 240$ mm for the PI force control. A) Parameters with $\omega = 1/\sqrt{2}T_D$ and b) parameters with $\omega = 1/\left(2\sqrt{2}-1\right)T_D$.

5.13a), and the other with a little reduced bandwidth $\omega_c = 1/\left(2\sqrt{2}-1\right)T_D$ (Figure 5.13b). For the higher ω_c, the controller shows a large overshot with a long settling time. This underlines the well known fact, that the outer controller must have a reduced bandwidth. In this case, the reduction is from around 750 Hz for the current loop to 580 Hz for the force loop, considering a sampling time T_s of 100 µs.

Now, the investigation is focused to the transition area, i.e. $-30\text{ mm} < x < 180\text{ mm}$ (Figure 5.2), as the force disturbance to be analyzed appears in this region. The reference force F_x^* is set to 200 N. For a speed of 1,56 m/s there are a total of 1346 samples in the transition area. The fundamental frequency of the current i_q is 26 Hz and the frequency of the slot harmonics is 156 Hz.

In Figure 5.14 $F_x^{FEM}(i_q,x)$ is a calculated quantity whereas i_q and x are obtained from measurement. Figure 5.14a-b shows the force $F_x^{FEM}(i_q,x)$ without using force control or force feed-forward, and setting a constant reference current i_q^* to 9.7 A, equivalent to 200 N. While the vehicle is inside of a segment, the mean force-current ratio of the machine, obtained by FEM tables, delivers 20.6 N/A.

The force F_x^{FEM} (Figure 5.14a) shows a sag of around 68 N (i.e. ≈ 33% of F_x^*) and a ripple around 74 N peak to peak. Applying the force feed-forward characteristic from Figure 5.11, the sag disappears totally and the ripple reduces to 20 N peak to peak (Figure 5.14c). This improvement in the force characteristic implies an injection of current harmonic with the frequency of 6 time the fundamental (i.e. 156 Hz, Figure 5.14d)

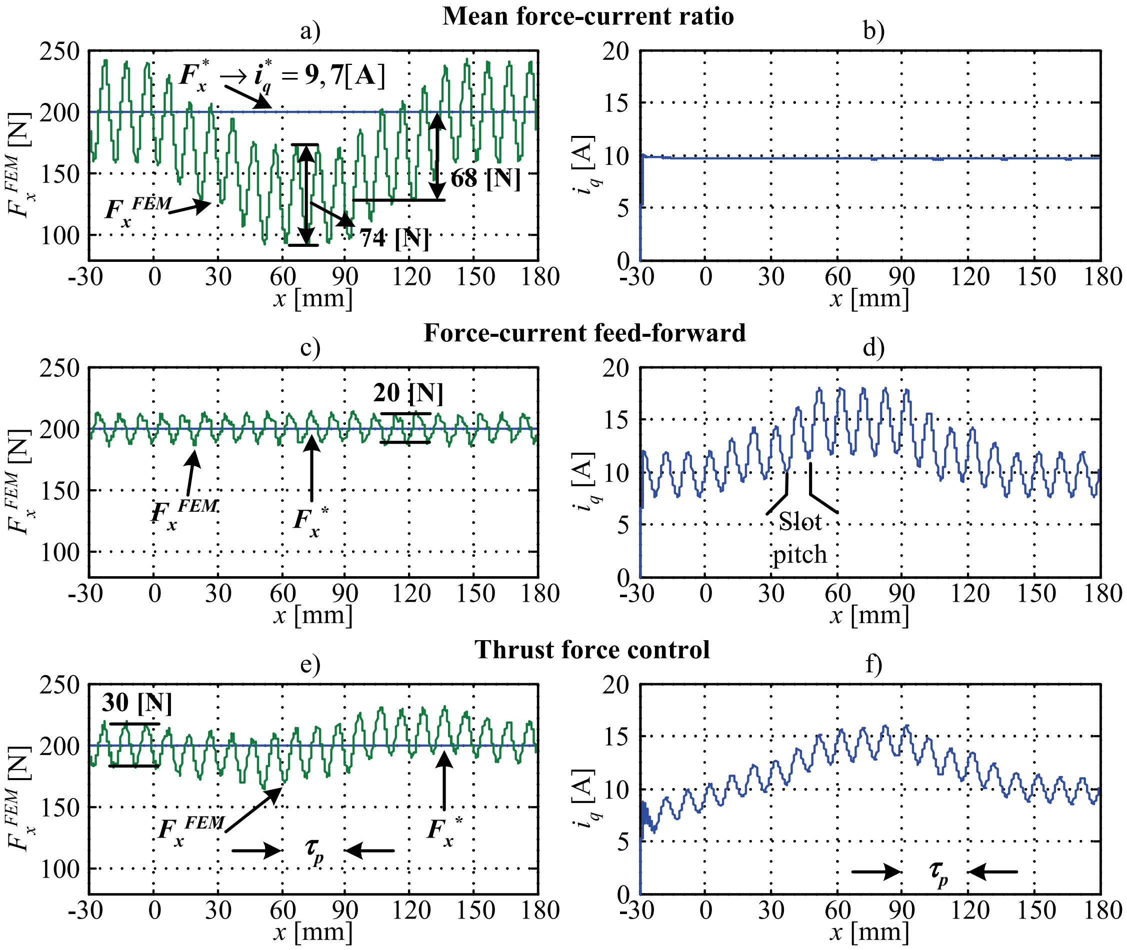

Figure 5.14: Force control measurement. a), c), e): reference and calculated thrust force for the control methods proposed in Figure 5.10. b) d) f): actual current i_q of the entered segment. Experiment carried out at constant speed v = 1,56 m/s and constant reference force F_x^* = 200 N.

(6 slots per pole pair). To compensate the sag, the force feed-forward characteristic may inject a higher current than the rated one, which is only acceptable for short time. Table $i_q(F_x^*,x)$ in Figure 5.11 is limited from –440 N to 440 N, i.e. approximately only 60% of the rated thrust force is available at all positions without exceeding the rated current.

The PI force controller presents a similar behavior in comparison with the force feed-forward control (Figure 5.14e). The force ripple increase a little in the middle of the transition, otherwise the ripple amplitude is 2 N less as the feed-forward variant. The power-up current for the segment in this case shows a large overshot (Figure 5.14f).

The force control reacts to the disturbances read from the table F_x^{FEM}, which not necessary is totally synchronized with the real force ripple in the machine. At this point, the synchronization and the accuracy for the position measurement are mandatory to compensate the real forces disturbances, and not only compensate the disturbances of the table. The synchronization between the position and force ripple are done based in the axis orientation on the simulation and the induced voltage of the motor.

The electric angle β_m is found with a synchronous measurement of the induced voltage e_a (phase a) and the position (appendix A.3). For two consecutive segment, the electric angle β_m is 180° shifted. On the other hand, the cogging force has a period of 60° (Figure 5.15), i.e. the synchronization of the force table F_x^{FEM} in the transition between two segments is not affected by the electric angle β_m.

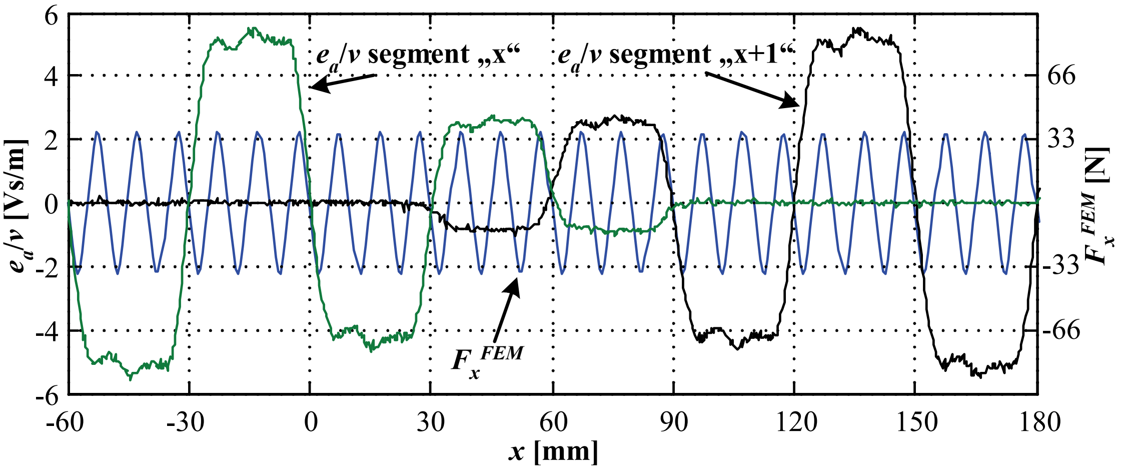

Figure 5.15: Normalized induced voltage for two consecutive segments and force F_x^{FEM} for zero current.

A simple experiment helps to show whether the compensation take effect. The load machine is turned off and the force reference F_x^* for the linear motor is set to zero. Then, the machine is moved by hand and only a marginal cogging force can be sensed by hand.

Figure 5.16a shows the behavior of the force F_x^{FEM} for the power-up of the odd segment by using the force-current feed forward method. The force (current) in the odd segment reaches it reference value in 10 sampling periods. In Figure 5.16b the reference and actual value of the current i_q can be seen. The actual current i_q is delayed by 2 sampling times with respect to the reference value, i.e. the control time delay. The controller saturates to the maximum voltage, which produces the linear growing up of the variables to reach the reference.

One more experiment is carried out to analyze the dynamic behavior of the proposed controller. Again, the linear machine is moved at constant speed v = 1,56 m/s. At posi-

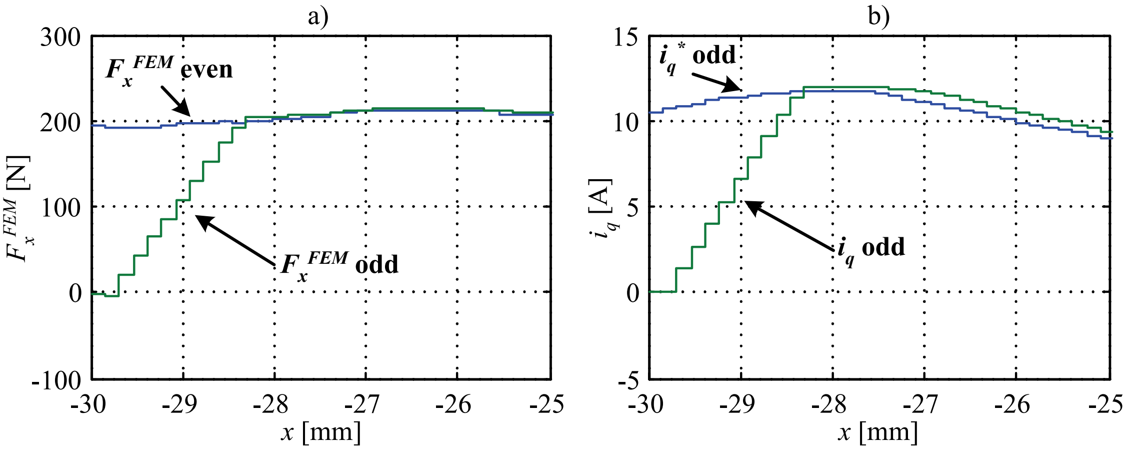

Figure 5.16: Force and current during the power-up of the segment with feed-forward force control. a) measures F_x^{FEM} for even and odd segments, b) reference and actual current i_q for the odd segment. Experiment carried out at constant speed $v = 156$ m/s.

tion $x = 240$ mm a step in the force reference F_x^* from 200 N to 240 N is applied (no saturation of the controller is reached). Figure 5.17a-b shows the measurements for the mean force-current ratio. The dynamics is determined by the current controller, and it reaches the reference after 3-4 sampling periods. For the force-current feed-forward characteristic in Figure 5.17c-d, again the dynamics is determined by the current controller and it reaches the reference after 3-4 sampling periods. The PI force controller involves the dynamics of the current controller and also the PI force controller. It reaches the reference after 4-5 sampling periods and shows a small overshoot.

5.2. Direct flux control

Direct Torque Control (DTC) has been introduced and studied in middle of the 1980's. Several DTC-based strategies were developed in the last two decades, like voltage-vector selection using switching tables [7][16][53], direct self Control [6][57], and some techniques using space vector modulation [15][54]. For the system proposed in this dissertation, only methods with modulator are applicable (hardware structure).

The Multiple Reference Frame (MRF) theory has been applied to suppress torque (force) ripple, especially in PM machines with non-sinusoidal back *EMF* [55]. Cogging force shows always a well known frequency which is proportional to the speed. For this reason MRF can be used to reduce it. If more Harmonics must be eliminated, then the MRF requires a large computational effort for the coordinate transformation.

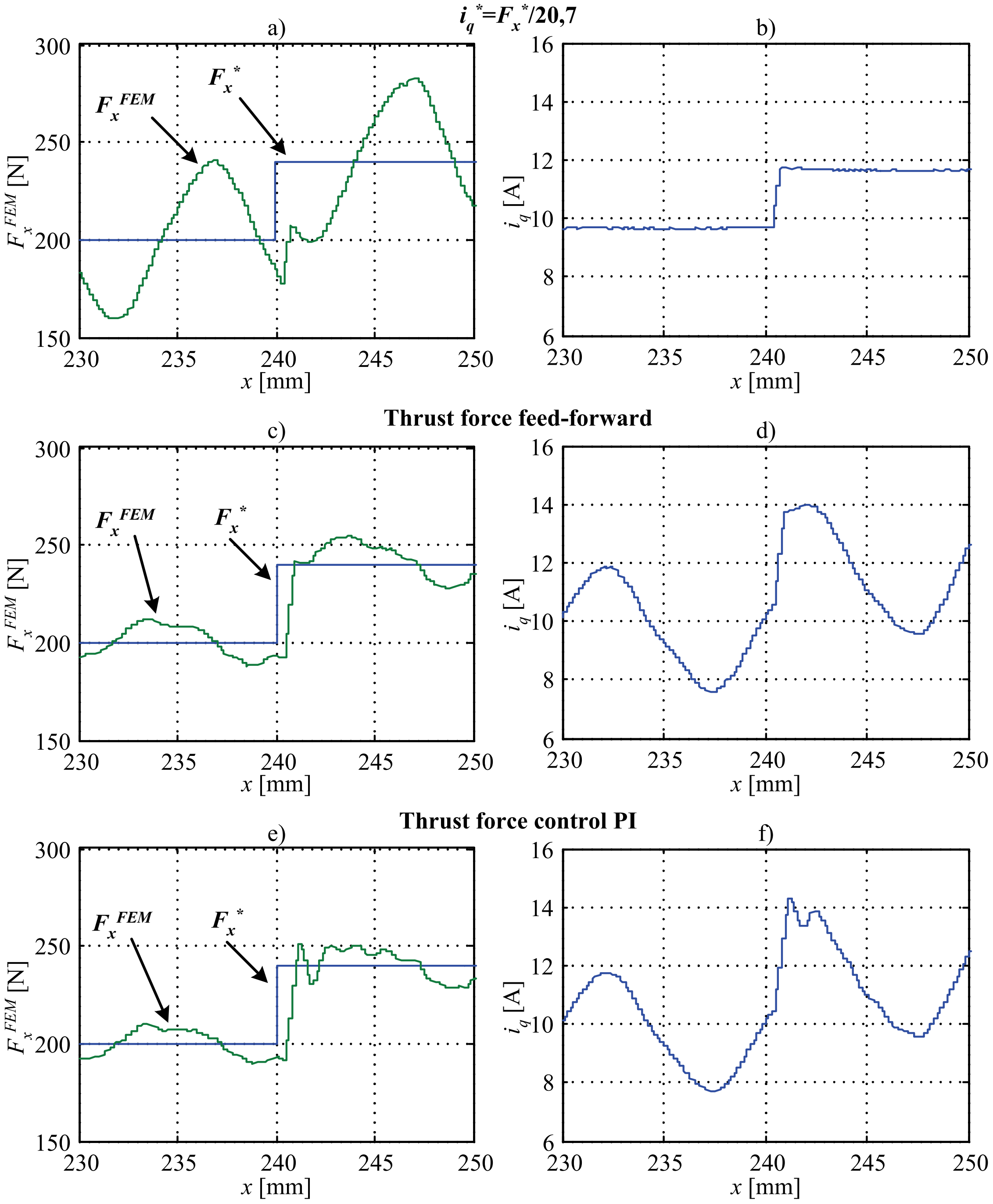

Figure 5.17: Step response for the three force controllers proposed: a), c), f) reference and calculated thrust force for the control methods with a step from 200 N to 240 N at $x = 240$ mm. b), d), f) actual current i_q. Experiment carried out at constant speed $v = 1{,}56$ m/s.

An alternative method to improve the dynamics of the system, is to use direct flux control [6][56], which is derived from direct self control. Figure 5.18 shows a block diagram of the control strategy, where, depending on the position of the switch S_1, a closed PI force controller loop or a feed-forward force-flux characteristic can be activated. The PI force control loop uses as feedback the force table F_x^{FEM} obtained from

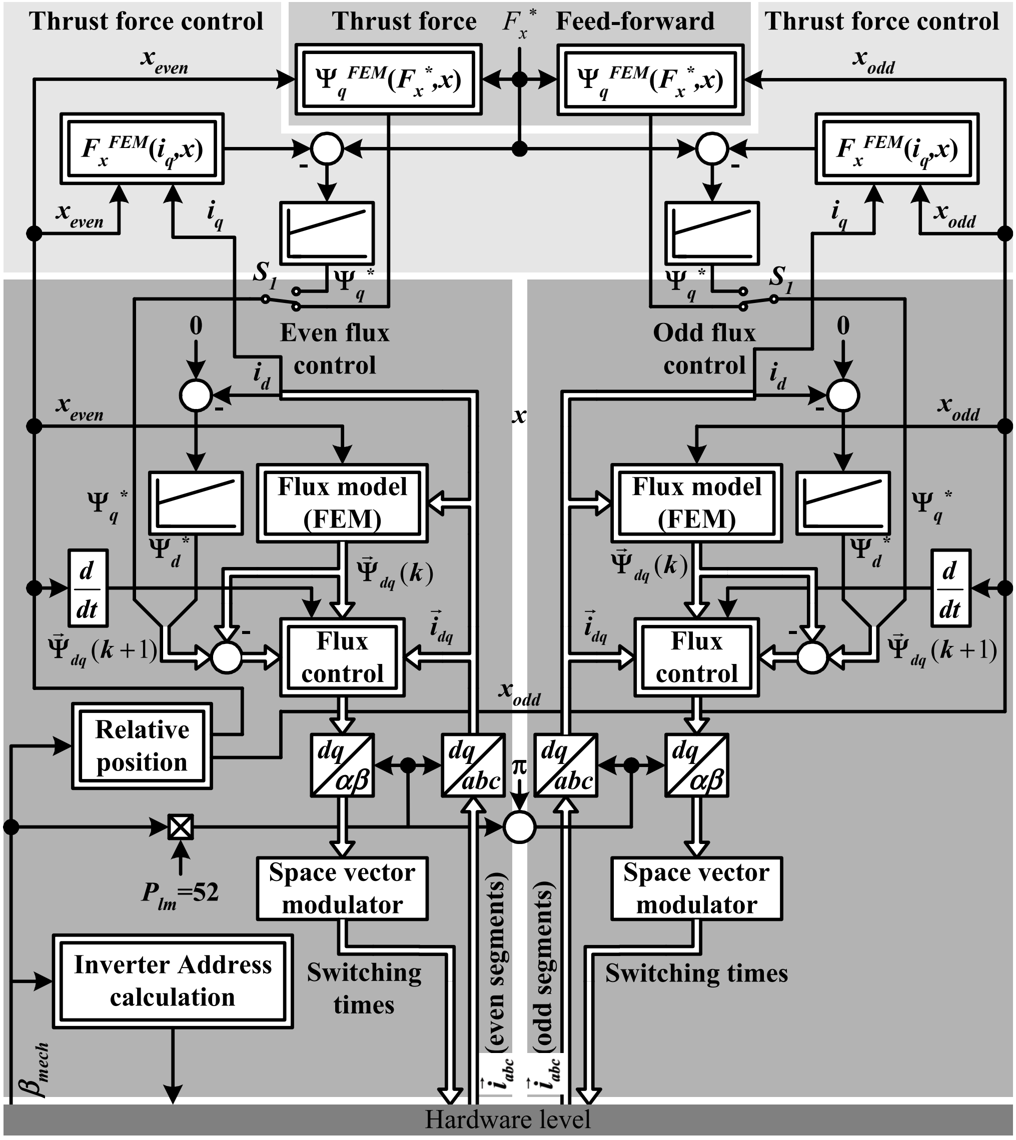

Figure 5.18: Control block diagram for a segmented linear motor using direct flux control.

FEM. The output of the force controller is the flux reference in the q-axis. A second controller is used to kept the current i_d to zero. The output of this controller is the flux reference in the d-axis. Then, the flux reference is compared with the actual flux and passed to the flux controller.

Instead of a flux observer, flux tables obtained by FEM (Figure 4.7 in chapter 4) are used with an additional dependence on the current i_d, simply modeled by a constant inductance (because i_d was not considered in the FEM simulation). Then, the linked fluxed Ψ_d and Ψ_q are now obtained as in (39) and (40) and implemented in the block “Flux model (FEM)” of Figure 5.18.

$$\Psi_d(i_d,i_q,x) = \Psi_d^{FEM}(i_q,x) + L_{dd}^{FEM}(i_q,x)\cdot i_d \tag{39}$$

$$\Psi_q(i_d,i_q,x) = \Psi_q^{FEM}(i_q,x) + \underbrace{L_{qd}^{FEM}\cdot i_d}_{\approx 0} \tag{40}$$

The flux controller uses the voltage equations (5) of the motor in *d-q* coordinate system to produce the voltage reference (41) and (42). For the sampling time "*k*", (5) is used to calculate the voltage that must be applied for the next interval k+1 to reach the desired linked flux $\vec{\Psi}_{dq}(k+1)$ [56]. The parameter K_{flux} in (41) and (42) are used to reduce the gain $1/T_s$ (10000), avoiding large changes in the output voltages, specially due to the tables inaccuracy and noise in the source signals (currents and position). Then, equations (41) and (42) are used in the block "flux control" of Figure 5.18. The inputs are the actual currents, calculated fluxes, actual speed and the desired flux variation. The dynamic change of the flux linkage is produced by the calculation of the difference of the reference and actual value divided by the sampling time and attenuated by K_{flux}.

$$u_d(k+1) = R\cdot i_d(k) + k_{flux}\cdot\frac{\Psi_d(k+1)-\Psi_d(k)}{T_s} - \frac{\pi}{\tau_p}\cdot\Psi_q(k)\cdot\frac{dx}{dt} \tag{41}$$

$$u_q(k+1) = R\cdot i_q(k) + k_{flux}\cdot\frac{\Psi_q(k+1)-\Psi_q(k)}{T_s} + \frac{\pi}{\tau_p}\cdot\Psi_d(k)\cdot\frac{dx}{dt} \tag{42}$$

When the mover enters a segment, the linked flux in the *d*-axis, Ψ_d increasing from zero to the nominal value, generating a ramp disturbance. Then, the PI current controller for the *d*-axis in Figure 5.18 must generate a ramp reference. PI controllers are not able to fully compensate this type of disturbances. To avoid this problem, the output of the controller must be the difference of the flux Ψ_d required to keep the current i_d=0. Then, equation (41) is rewritten as in (43), where $\Delta\Psi_d\big|_{i_d=0}$ is the output of the PI controller.

$$u_d(k+1) = R\cdot i_d(k) + k_{flux}\cdot\frac{\Delta\Psi_d\big|_{i_d=0}}{T_s} - \frac{\pi}{\tau_p}\cdot\Psi_q(k)\cdot\frac{dx}{dt} \tag{43}$$

Additionally, the over-modulation method is very important and determines the behavior of the system for a large step change of the input. For a large step, the modulator must apply the largest voltage vector in the direction that the flux should increase. The voltage limitation is given by the 6 active vectors of a three phase 2 levels inverter. The hexagon formed by the active vectors limits the available voltage. The edges of the hexagon are given by switching exclusively the active vectors. Inside of the hexagon,

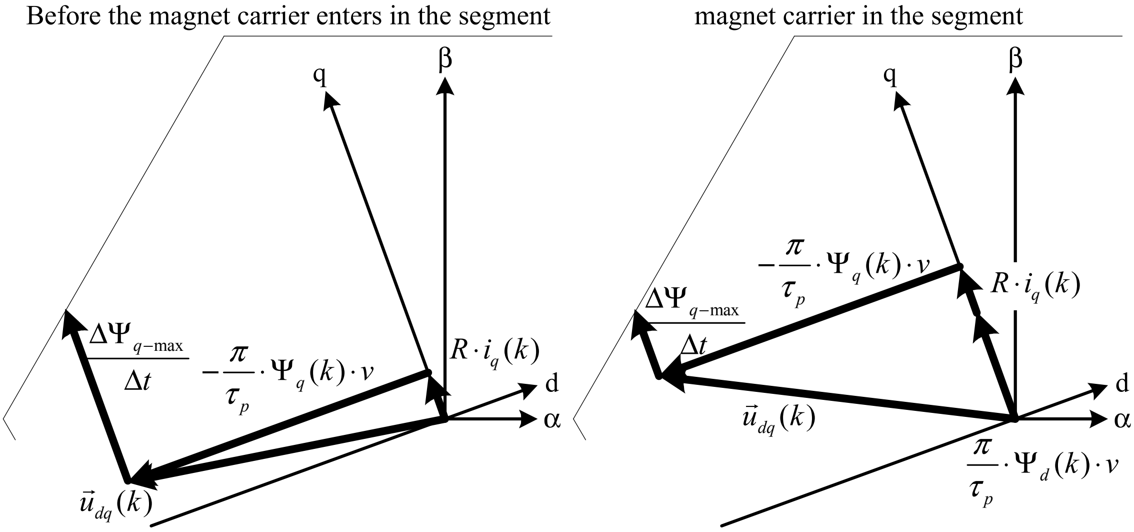

Figure 5.19: Vector diagram and over-modulation limits for a segment.

the zero vector must be applied. In the literature there are many approaches to limit the voltage inside of the hexagon [20][58].

In steady state $\vec{u}_{dq}$ is constant ($\vec{u}_{dq}(k+1)=\vec{u}_{dq}(k)$). Figure 5.19 shows the steady state vector diagram of a segment and the maximal flux Ψ_q variation possible in two cases, one when the magnet carrier is approaching the segment at constant speed v (segment powered-up), and the other, when the magnet carrier moves at constant speed v inside of a segment. In case that the voltage $\vec{u}_{dq}(k+1)$ is outside of the hexagon, the voltage is limited to the maximal $\Delta\Psi_q/\Delta t$ possible.

The feed forward table $\Psi_q^{FEM}(F_x,x)$ is obtained from FEM simulations. Figure 5.20 shows $\Psi_q^{FEM}(F_x,x)$ with an asymmetry between the first and last 150 mm in the move-

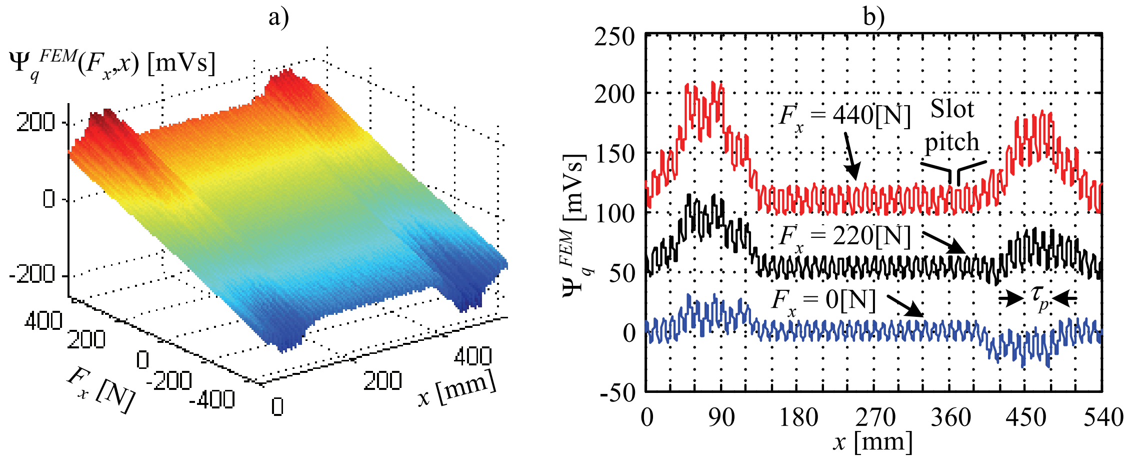

Figure 5.20: Feed forward table $\Psi_q^{FEM}(F_x,x)$ for direct flux control.

ment of the vehicle. This asymmetry is produced by the winding distribution of the stator and the odd number of poles of a segment.

In order to determine experimentally the parameter k_{flux}, a step in the flux reference Ψ_q^* of 0,05 Vs is applied (no saturation of the modulator is reached) and then k_{flux} is adjusted to reach an overshot less than 10%. With k_{flux} = 0,5 the flux controller shows the desired behavior (Figure 5.21).

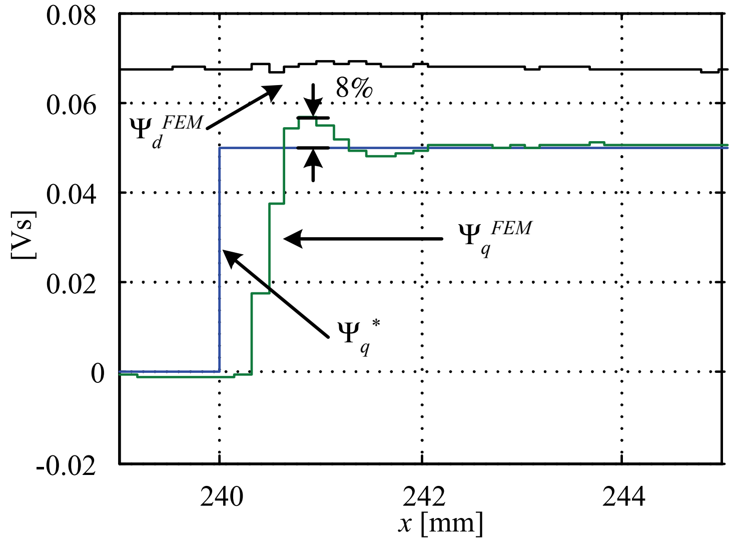

Figure 5.21: flux controller behavior for a step 0.05 Vs in the reference. Experiment carried out at constant speed v = 1,56 m/s and k_{flux} = 0,5.

The PI force controller is tuned considering the inner flux control loop as a first order system with an equivalent time constant $T_{eq\text{-flux}}$. As in section 0 (force-current controller), the force control loop is simplified as shown in Figure 5.23. For the second order closed loop transfer function again the AO criteria is used to tune the controller parameters k_p (45) and T_i (44) [13](appendix A.5).

$$T_i = \frac{\sqrt{2} \cdot T_{eq-flux}\omega_c - 1}{T_{eq-flux}\omega_c^2} \tag{44}$$

$$k_p = \frac{\sqrt{2} \cdot T_{eq-flux}\omega_c - 1}{k_\Psi} \tag{45}$$

The same cut-off frequency ω_c is selected as for the force-current control, i.e $\omega_c = 1 \big/ \left(2\sqrt{2} - 1\right) T_D$.

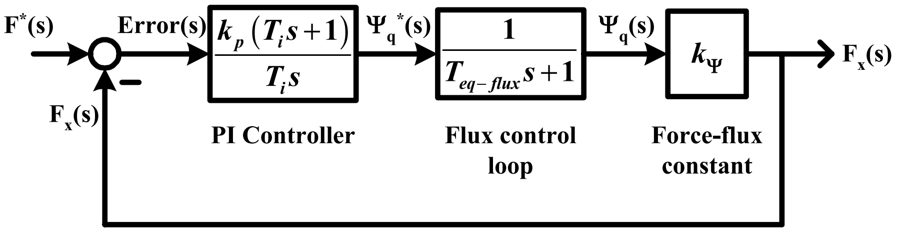

Figure 5.23: Simplified thrust force control loop.

To analyze the behavior of the force-flux control, the linear machine is moved at constant speed v = 1,56 m/s (half turn to the annulus per second) by the load machine. This is the same condition as was used for the experiment in the previous section. Again, the investigation is focused to the transition area, i.e. –30 mm < x < 180 mm. The reference force F_x^* is set to 200 N. For a speed of 1,56 m/s there are a total of 1346 samples in the transition area. The fundamental frequency of the current i_q is 26 Hz and the frequency of the slot harmonics is 156 Hz.

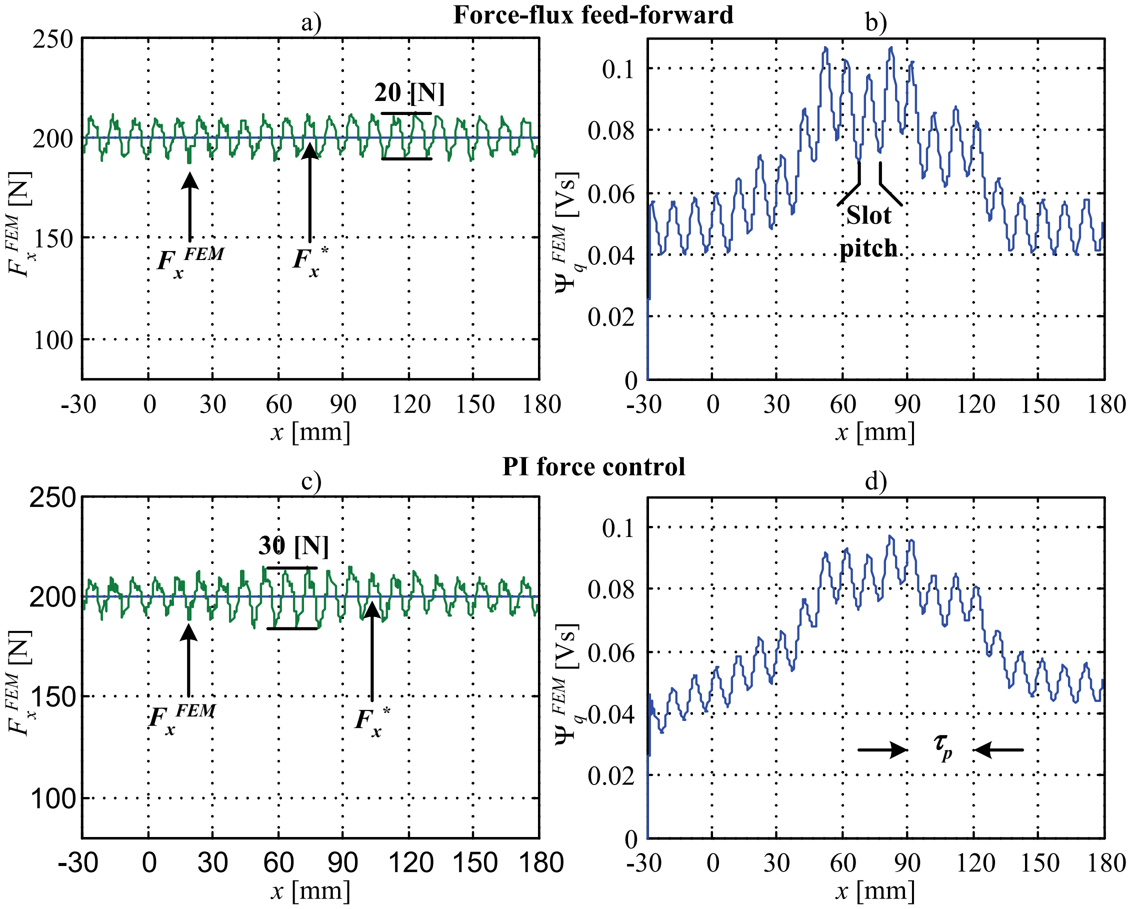

Figure 5.22: Direct flux control experimental measurements. a), b) Reference force F_x^*, actual force calculated by FEM tables F_x^{FEM} and flux Ψ_q^{FEM} for direct flux control using the force-flux characteristic of Figure 5.20. c) d) as in a) and b) with a PI force controller. Experiment carried out at constant speed v = 1.56 m/s.

Figure 5.22a-b shows the experimental measurements of the control variables for the force-flux feed-forward control loop using the table from Figure 5.20. The force F_x^{FEM} follows the reference without problems during the entire transition. There remains a constant ripple of 20 N peak to peak. For the superimposed force-flux controller, the force F_x^{FEM} increases the ripple in the middle of the transition to 30 N peak to peak (Figure 5.20c). Figure 5.20b-d shows the fluxes Ψ_q^{FEM} necessary to reach the force behavior in Figure 5.20a-c respectively.

In Figure 5.24 the dynamic behavior of the feed-forward force-flux controller (a and b) and of the PI force-flux controller (c and d) is shown. At position x = 240 mm a step in the force reference F_x^* from 200 N to 240 N is applied (no saturation in the controller). For the feed-forward force-flux characteristic, the dynamics is determined by the flux controller and it reaches the reference after 3-4 sampling periods. The PI force-flux controller involves the dynamic of the flux controller and also the PI force controller. It

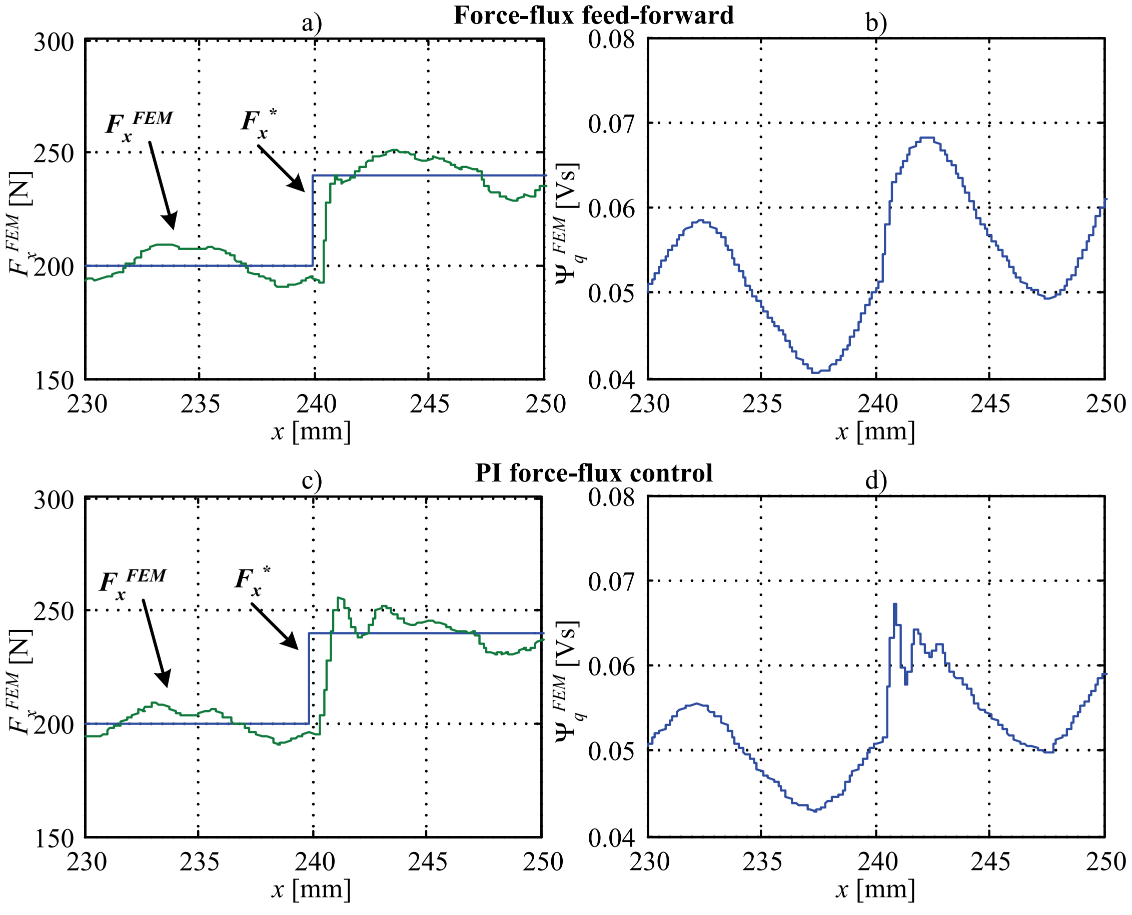

Figure 5.24: Step response for the feed-forward and PI force controllers proposed: a), c) reference and calculated thrust force for the control methods with a step from 200 N to 240 N at x = 240 mm. b), d) actual linked flux Ψ_q. Experiment carried out at constant speed v = 1,56 m/s.

reaches the reference after 4-5 sampling periods and has overshot.

5.3. Resonant control

In the standard field oriented control, the PI controller is not able to reject harmonics, producing steady state errors. In the previous sections, superimposed force-current and force-flux control respectively are not able to reject totally the detent force. To aid the PI controller, in this chapter a resonant element is added in parallel. The complete analysis of the stability and optimizations must be done for the entire system.

Two configurations of resonant controllers were studied in previous research [59][60], well known as P+Sine (46) transformed resonant element and P+Cosine (47) transformed resonant element. Another resonant element was develop in [51] (48) by integrating the two aforementioned types of resonant elements.

$$C_{P+\sin}(s) = k_p + \frac{k_{r-\sin}\omega_{res}^2}{s^2+\omega_{res}^2} \tag{46}$$

$$C_{P+\cos}(s) = k_p + \frac{k_{r-\cos}\omega_{res}s}{s^2+\omega_{res}^2} \tag{47}$$

$$C_{P+\sin+\cos}(s) = k_p + \frac{k_{r-\cos}\omega_{res}s + k_{r-\sin}\omega_{res}^2}{s^2+\omega_{res}^2} = \frac{k_{r2}s^2 + k_{r1}\omega_{res}s + k_{r0}\omega_{res}^2}{s^2+\omega_{res}^2} \tag{48}$$

The resonant controller of (48) can be improved adding a damping factor *d* to limit the gain at ω_{res} and increasing the width of the resonance peak. This improves the controller in case of deviation of the resonance frequency. The resulting transfer function for the controller is described by (49) and its frequency and phase response is shown in

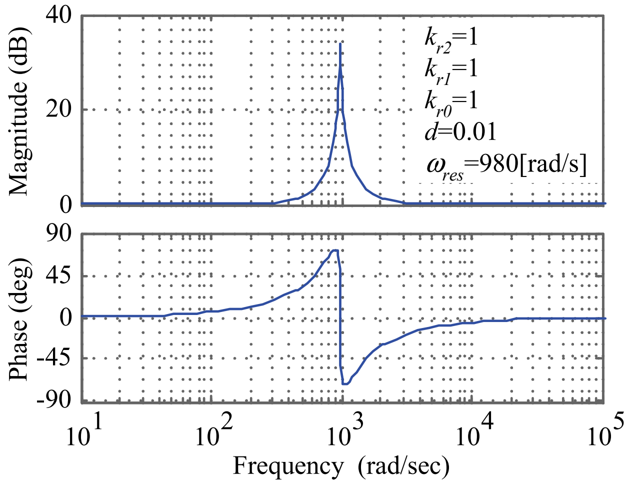

Figure 5.25: Bode diagram for the resonant controller $C_{res}(s)$ at ω_{res} = 156 Hz.

Figure 5.25.

$$C_{res}(s) = \frac{k_{r2}s^2 + k_{r1}\omega_{res}s + k_{r0}\omega_{res}^2}{s^2 + 2d\,\omega_{res}s + \omega_{res}^2} \tag{49}$$

The FEM simulation delivers a pulsating thrust force which is used as feedback in the control loop of the machine. This eliminates the sag in the force when the vehicle travels between two consecutive segments. Figure 5.26 shows a standard field oriented control structure in the rotor *d-q* coordinate system for the segmented linear drive with F_x^* as input, one current loop for the *d*-axis with a resonant element, and one force loop for the *q*-axis with a resonant element too, all for odd and even segments. In fact, a resonant element in the *d*-axis is not necessary, but it helps to suppress harmonics from the *EMF*.

The resonant controller $C_{res}(s)$ is in parallel to a PI controller. The parameters of the PI and resonant controller must be tuned for the entire closed loop transfer function. Figure 5.27 shows a simplified linear model of the controller, considering the inverter

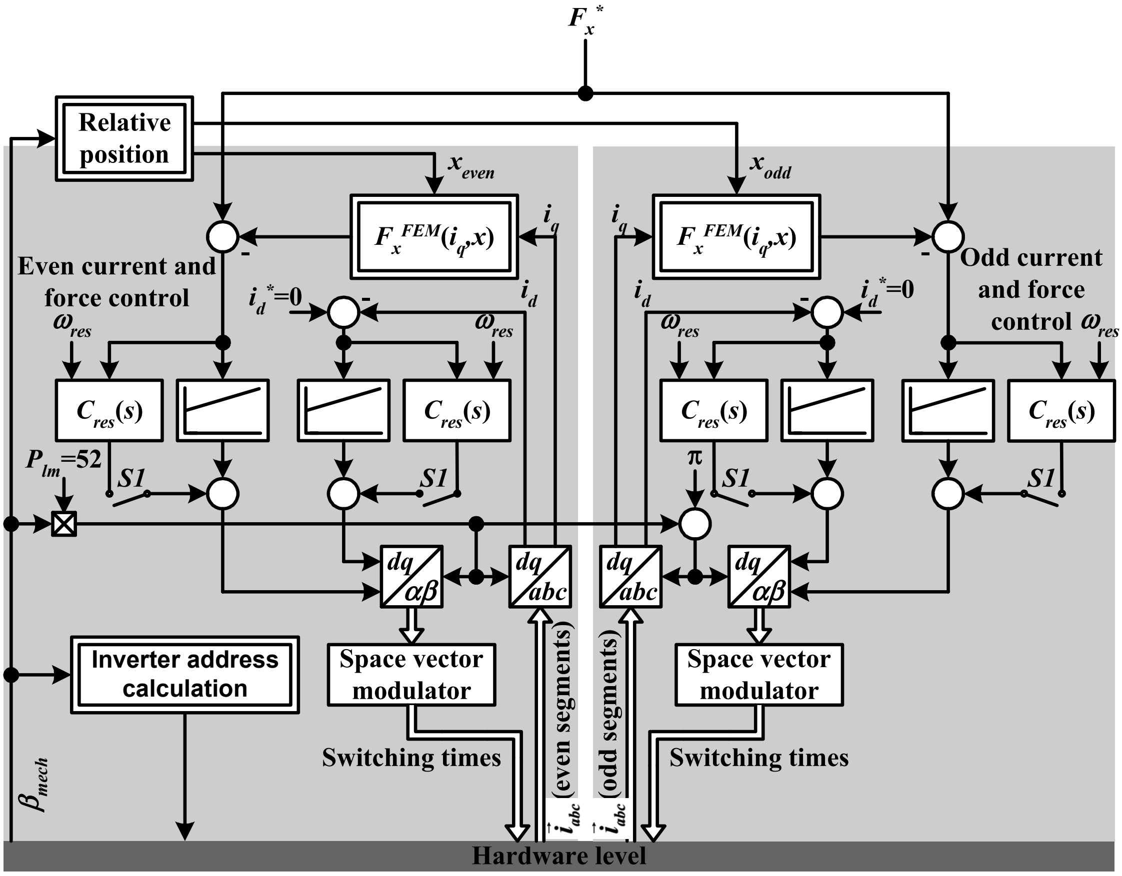

Figure 5.26: control block diagram for the segmented linear drive with resonant controller.

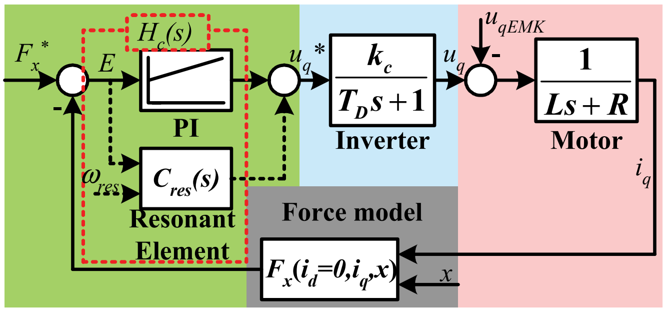

Figure 5.27: Simplification of the resonant controller and the plant for the q-axis.

dynamics and the motor. T_D and k_c are the control time delay and inverter gain respectively. L and R denote the inductance and the resistance of the motor segment respectively.

To obtain the open loop transfer function it is necessary to simplify the force model to an equivalent gain k_f. The ripple introduced by the force model must be rejected by the resonant controller and it is not necessary to consider it in tuning. Equation (50) shows the transfer function $H_c(s)$ of the entire controller (PI+$C_{res}(s)$) and (51) the plant $H_p(s)$ (Inverter + Motor + Force model).

$$H_c(s) = \underbrace{k_p\left(1+\frac{1}{T_i s}\right)}_{PI} + \underbrace{\frac{k_{r2}s^2 + k_{r1}\omega_{res}s + k_{r0}\omega_{res}^2}{s^2 + 2d\omega_{res}s + \omega_{res}^2}}_{C_{res}(s)} = \frac{N_c(s)}{D_c(s)} \tag{50}$$

$$H_p(s) = \frac{k_c k_f}{(Ls+R)(T_D s+1)} \tag{51}$$

At first the electric pole of the plant can be eliminated with one zero of the controller, i.e. the numerator of $H_c(s)$ must be factorized by (Ls+R). Using $N_{cd}(s)$ (52) as the desired polynomial for the numerator of the controller $H_c(s)$, it is possible to rewrite it as (53).

$$N_{cd}(s) = \left(Ls+R\right)\left(b_2 s^2 + b_1 s + 1\right) \tag{52}$$

$$H_c(s) = \frac{\left(Ls+R\right)\left(b_2 s^2 + b_1 s + 1\right)}{T_i s\left(s^2 + 2d\omega_{res}s + \omega_{res}^2\right)} \tag{53}$$

The benefit of using (52) is the order reduction in the closed loop transfer function $H_{close}(s)$. By matching the numerator of (49) with polynomial (52), k_{r1}, k_{r2}, k_{r3} and k_p are defined now as function of b_2, b_1, T_i, d, and ω_{res} (54)(55)(56)(57).

$$k_{r2} = \frac{b_2 L}{T_i} - \frac{R}{\omega_{res}^2} \tag{54}$$

$$k_{r1} = \frac{b_1 L \omega_{res}^2 + R\left(b_2 \omega_{res}^2 - 2dT_i \omega_{res} - 1\right)}{T_i \omega_{res}^3} \tag{55}$$

$$k_{r0} = \frac{\omega_{res}\left(L + R\left(b_1 - T_i\right)\right) - 2dR}{T_i \omega_{res}^3} \tag{56}$$

$$k_p = \frac{R}{\omega_{res}^2} \tag{57}$$

The pole assignment technique aims, by designing the controller, to place the poles of the closed loop system at desired locations. The poles of the closed loop transfer function $H_{close}(s)$ (58) are now described by a fourth order polynomial. A desired characteristic polynomial $D_{close}(s)$ (59) is obtained using the principle of the “double ratios” [13]. In (59) τ is a parameter for the position of the poles (Appendix A.6).

$$H_{close}(s) = \frac{H_c(s)H_p(s)}{1 + H_c(s)H_p(s)} \tag{58}$$

$$D_{close}(s) = \frac{\tau^4}{64}s^4 + \frac{\tau^3}{8}s^3 + \frac{\tau^2}{2}s^2 + \tau s + 1 \tag{59}$$

The solution of the equation system for the coefficients of the denominator of (58) with the coefficients of (59) delivers the parameters b_2 (60), b_1 (61), T_i (62) and τ (63).

$$b_2 = \frac{32T_D^2\left(1 + 2T_D^2\omega_{res}^2\left(2d^2 - 1\right)\right)}{\left(1 + 2dT_D\omega_{res}\right)^4} \tag{60}$$

$$b_1 = \frac{8T_D\left(1 + 6dT_D\omega_{res} - 8T_D^2\omega_{res}^2 + 12d^2T_D^2\omega_{res}^2 + 8d^3T_D^3\omega_{res}^3\right)}{\left(1 + 2dT_D\omega_{res}\right)^4} \tag{61}$$

$$T_i = \frac{64k_c k_f T_D^3}{\left(1 + 2dT_D\omega_{res}\right)^4} \tag{62}$$

$$\tau = \frac{8T_D}{1 + 2dT_D\omega_{res}} \tag{63}$$

The damping factor d must be smaller than $1/\sqrt{2}$ in order to achieve resonance. For example, in Figure 5.25 the damping factor d is 0.01, i.e. τ is limited to (64). Then, the dynamic of the closed loop is less dependent on the resonant frequency ω_{res}, and it is limited to the poles described by (65). The Root Locus of the open loop transfer function $H_c(s)H_p(s)$ in Figure 5.28 confirm the above mentioned.

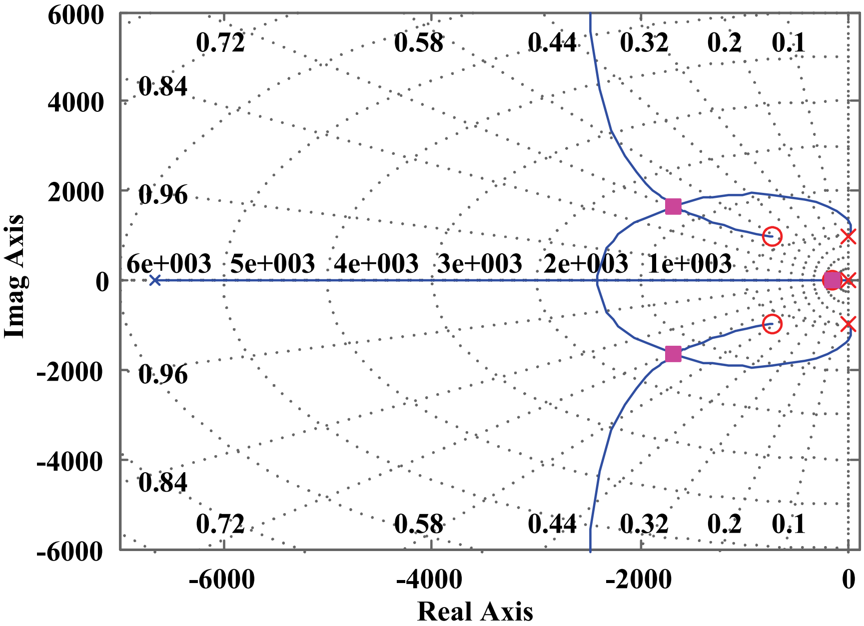

Figure 5.28: Root-locus of the open loop transfer function $H_c(s)H_p(s)$ for ω_{res}=156Hz.

$$\tau = \frac{800T_D}{100+2T_D\omega_{res}} \approx 0,0012 \tag{64}$$

$$s_{1,2,3,4} = -\frac{2 \pm j2}{\tau} \approx -1666 \pm j1666 \tag{65}$$

To increase the degrees of freedom in the closed loop transfer function, it is necessary to add a derivative part in the PI controller, i.e. a PID. The new transfer function of the controller $H_{c1}(s)$ is described by (66), and the desired numerator function $N_{cd1}(s)$ is given by (67). The resulting controller transfer function using $N_{cd1}(s)$ is described by (68).

$$H_{c1}(s) = \underbrace{k_p\left(1+\frac{1}{T_i s}+T_d s\right)}_{PID} + \underbrace{\frac{k_{r2}s^2+k_{r1}\omega_{res}s+k_{r0}}{s^2+2d\omega_{res}s+\omega_{res}^2}}_{C_{res}(s)} = \frac{N_{c1}(s)}{D_{c1}(s)} \tag{66}$$

$$N_{cd1}(s) = \left(Ls+R\right)\left(b_3s^3+b_2s^2+b_1s+1\right) \tag{67}$$

$$H_{c1}(s) = \frac{\left(Ls+R\right)\left(b_3s^3+b_2s^2+b_1s+1\right)}{T_i s\left(s^2+2d\omega_{res}s+\omega_{res}^2\right)} \tag{68}$$

The PID controller adds a ZERO in the numerator of the open loop transfer function of the system, adding a degree of freedom for the poles in the closed loop. Again k_{r1}, k_{r2}, k_{r3} T_d, and k_p (69)(70)(71)(72)(73) are obtained from (66) and (68).

$$k_{r2} = \frac{b_2 L + b_3 \left(R - 2dL\omega_{res}\right)}{T_i} - \frac{R}{\omega_{res}^2} \tag{69}$$

$$k_{r1} = \frac{R\left(b_2\omega_{res}^2 - 2dT_i\omega_{res} - 1\right) + L\omega_{res}^2\left(b_1 - b_3\omega_{res}^2\right)}{T_i\omega_{res}^3} \tag{70}$$

$$k_{r0} = \frac{\omega_{res}\left(L + R\left(b_1 - T_i\right)\right) - 2dR}{T_i\omega_{res}^3} \tag{71}$$

$$T_d = \frac{b_3 L\omega_{res}^2}{RT_i} \tag{72}$$

$$k_p = \frac{R}{\omega_{res}^2} \tag{73}$$

The desired characteristic polynomial for the closed loop $D_{close}(s)$ (59) does not change, because the order for the denominator is the same as in (58) using $H_{c1}(s)$ instead of $H_c(s)$. The parameters b_3 (74), b_2 (75), b_1 (76), and T_i (77) are obtained by solving the equations for the coefficients.

$$b_3 = -\frac{\tau^3\left(\tau - 8T_D + 2d\tau T_D\omega_{res}\right)}{64T_D} \tag{74}$$

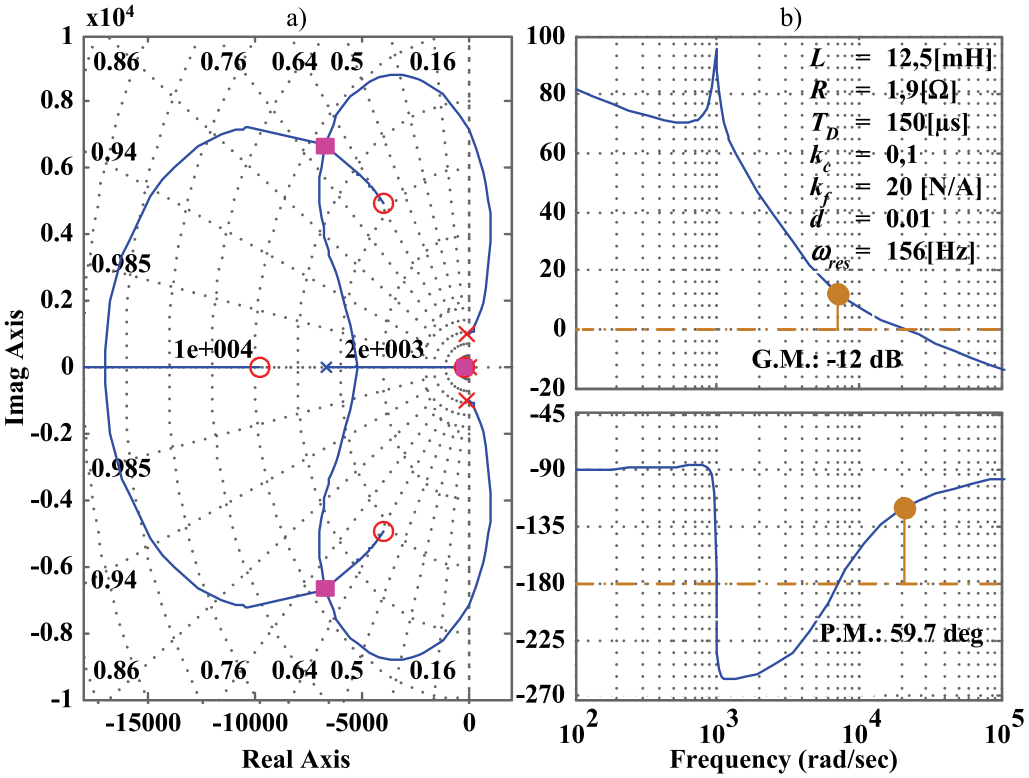

Figure 5.29: Root Locus (a) and Bode diagram (b) of the open loop for a PID+Res controller.

$$b_2 = \frac{32\tau^2 T_D - \tau^4 \omega_{res}\left(2d + T_D \omega_{res}\right)}{64T_D} \tag{75}$$

$$b_1 = \tau - \frac{\tau^4 \omega_{res}^2}{64T_D} \tag{76}$$

$$T_i = \frac{k_c k_f \tau^4}{64T_D} \tag{77}$$

Now, the closed loop poles (65) can be chosen at a desired position. To achieve the dynamics of a second order system tuned with the amplitude optimum criteria, the real part of the poles must be placed in -1/2T_D. This condition determines τ (78) and the poles of the closed loop (79).

$$\tau = 2T_D = 0{,}0003 \tag{78}$$

$$s_{1,2,3,4} = \frac{-2 \pm j2}{\tau} = -6666{,}7 \pm j6666{,}7 \tag{79}$$

Figure 5.29a shows the Root Locus for the system with the four poles in the closed loop in the desired position (79). In Figure 5.29b, the resonance peak in the Bode dia-

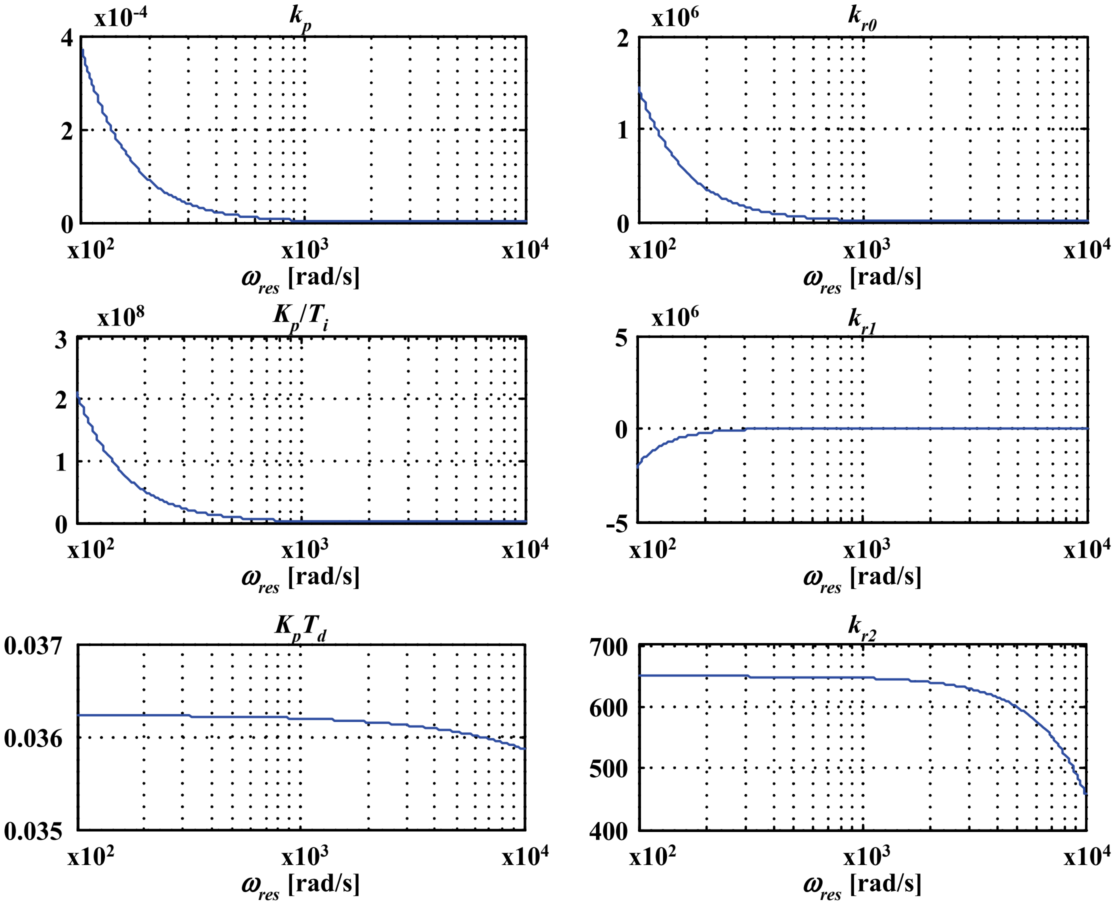

Figure 5.30: Parameter for the PID+Res controller for frequencies from 100 to 10000 rad/s.

gram of the open loop transfer function can be clearly appreciated.

In order to guaranty stability at low speed, for frequencies under 100 rad/s (i.e. 16 Hz) the resonant controller and the derivative part is disconnected and the PI take the parameter given by the amplitude optimum criteria (32)(33).

T_i is the only parameter that does not depend on ω_{res} and has a constant value determined by τ. Under the condition of (78), T_i takes the value $1{,}75\text{x}10^{-12}$. With a damping factor of 0.01 and replacing (74), (75) and (76) into (69), (70) and (71), the controller parameters are obtained as function of the resonance frequency ω_{res}. Figure 5.30 shows the parameters of the controller for frequencies from 100 to 10000rad/s. However, the large variation for the integral component k_p/T_i and the resonant parameter k_{r1} and k_{r0}, destabilize the closed loop.

A practical solution is to preserve the PI controller tuned with the Amplitude Optimum (AO) Criteria and add only a sine resonant element $C_{sin}(s)$ ((46) page 74) or a cosine resonant element $C_{cos}(s)$ ((47) page 74).

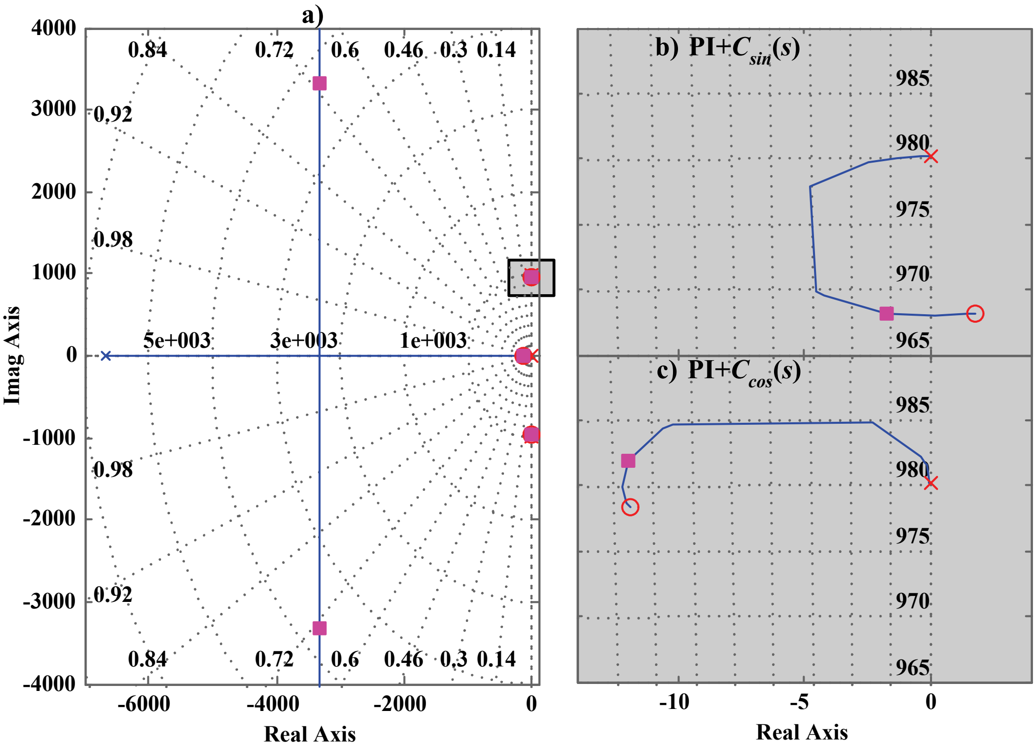

Figure 5.31: Root Locus diagram of the open loop for a PI+$C_{sin}(s)$ (a)(b) and a PI+$C_{cos}(s)$ (C) controller. The PI controller is tuned with the AO criteria. K_r is set to 1. the resonance frequency is set to 156 Hz.

From the literature it is known that the phase margin of $C_{cos}(s)$ is 90° higher than that of $C_{sin}(s)$. Therefore $C_{sin}(s)$ has a poorer phase margin. Poor phase margin can cause a highly under-damped behavior [61] of the system. In case of a PI+$C_{sin}(s)$ or a PI+$C_{cos}(s)$, the number of poles and zeros of the controller does not change, i.e. there is no effect concerning the phase of the system. Figure 5.31 shows the Root Locus diagram for the open loop $H_c(s)H_p(s)$ for both resonant controllers, tuning the PI according to the AO criteria. Roughly, there are no differences between both controllers (Figure 5.31a) but looking in detail around the resonant pole, the sine resonant element shows a zero on the right-half s-plane (Figure 5.31b), i.e. the system has non-minimum-phase zeros. Even so, both controllers will be analyzed and applied to the force control loop.

To demonstrate the behavior of the PI+$C_{sin}(s)$ (and PI+$C_{cos}(s)$) controller, two experiments are carried out. At first, the linear machine is moved at constant speed $v = 1.56$ m/s. The force reference F_x^* is set to 200 N. At the beginning, the switch $S1$ is open (Figure 5.26), i.e. only the PI controller is active. Then, at position $x = 240$ mm, the switch $S1$ is closed. Figure 5.32 shows the poor behavior of the $C_{sin}(s)$ controller, which needs more than five cycles of the force ripple to begin to suppress it. On the other hand, the controller $C_{cos}(s)$ needs only one cycle of the detent force to begin the suppression of the ripple. For an extended traveling distance, Figure 5.33 shows the force F_x^{FEM} along 3 segments. The resonant controller $C_{sin}(s)$ is more affected in the transition area than the $C_{cos}(s)$. In general, for all positions the cosine variant of the resonant element shows a better behavior and ripple rejection.

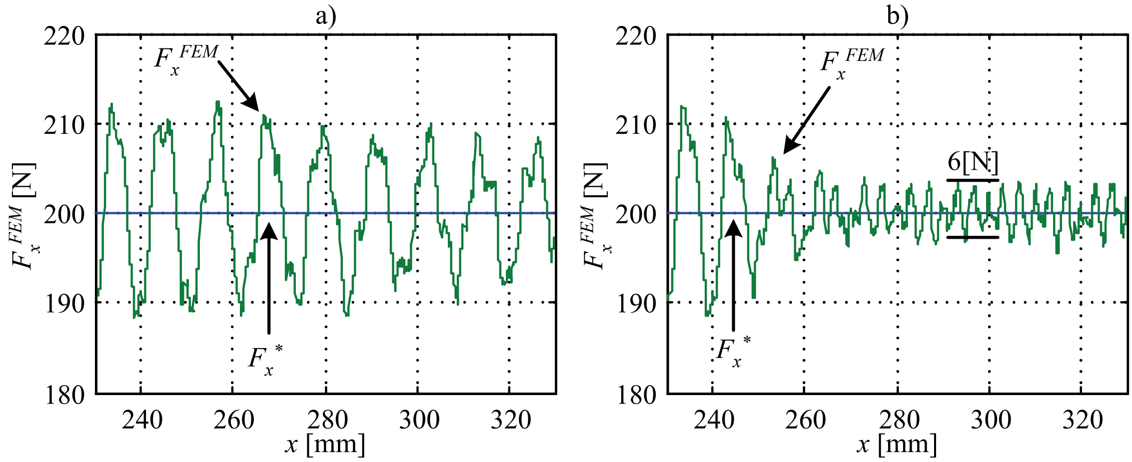

Figure 5.32: Comparison of PI+$C_{sin}(s)$ (a) and PI+$C_{cos}(s)$ (b) activated at position $x = 240$ mm for the force control. Force reference $F_x^* = 200$ N. Experiment carried out at constant speed $v = 1.56$ m/s. Time windows: ≈ 64 ms for 100 mm.

In order to investigate the dynamic effect of the resonant element added to the loop, a second experiment was carried out. With the same conditions as the previous experiment, the cosine resonant element was always activated. Then, at position $x = 240$ mm a step in the command force F_x^* from 200 N to 240 N is applied. Figure 5.34 shows the command force F_x^* and the calculated force F_x^{FEM}. There are nearly no differences comparing the dynamic behavior of the superimposed force-flux control loop as shown in Figure 5.24 and the behavior of the force+resonant controller in Figure 5.34, but in the steady state the force ripple is considerably reduced.

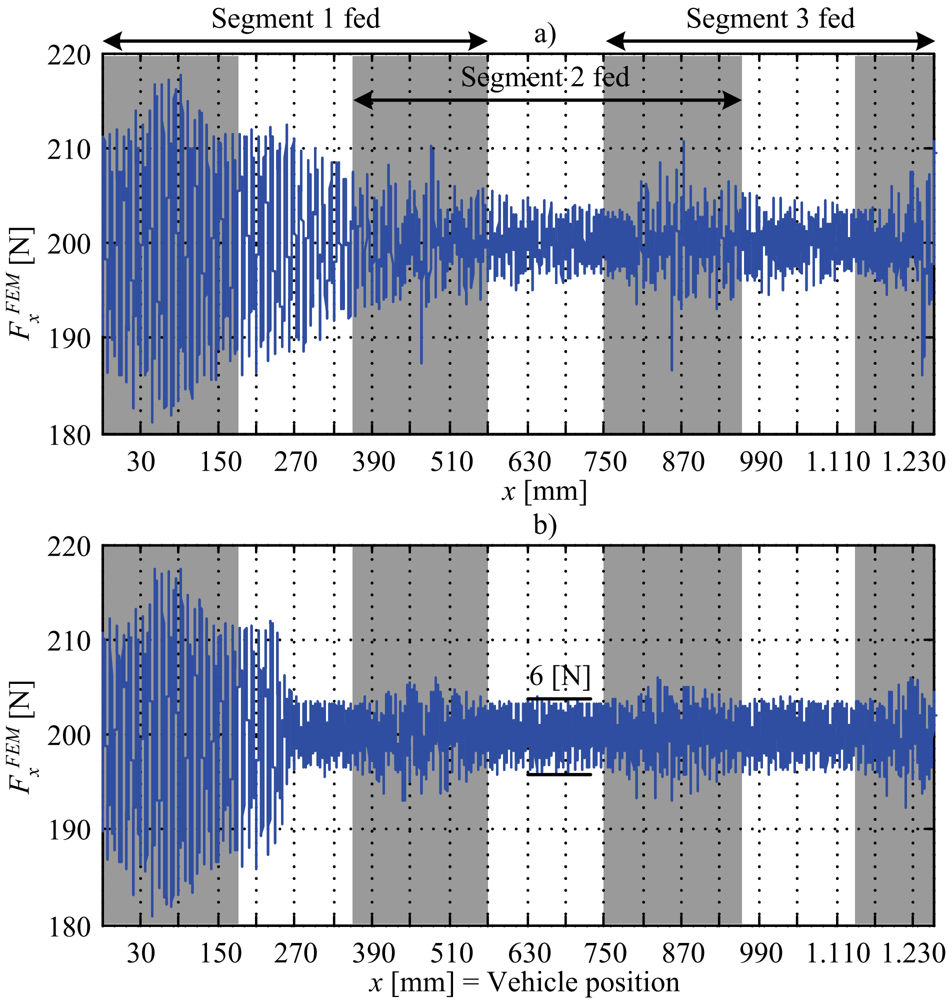

Figure 5.33: Extension of the force measurement F_x^{FEM} for 3 segments. The resonant element $C_{sin}(s)$ (a) and $C_{\cos}(s)$ (b) is activated at $x = 240$ mm respectively. Experiment carried out at constant speed $v = 1.56$ m/s and constant reference force F_x^*.

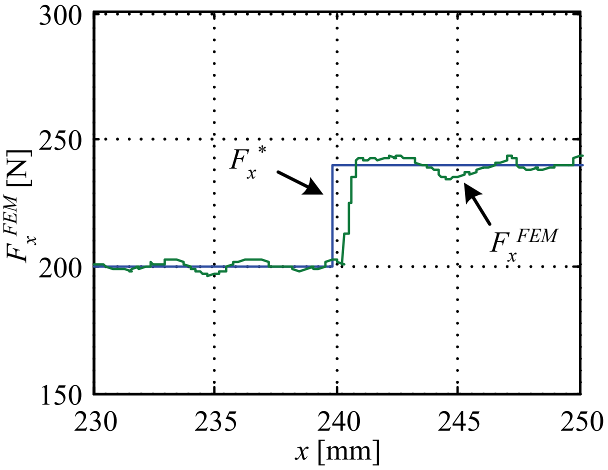

Figure 5.34: Force step response of a PI+Ccos(s) controller. Command step from 200 N to 240 N at position x = 240 mm. Experiment carried out at constant speed v = 1.56 m/s.

6. Conclusions

The main results of the investigation concerning the control methods for Segmented Long-Stator Linear motors will be resumed and concluded in the following chapter.

6.1. Summary

In this thesis a new perspective of application for linear drives was considered, focusing on the application for industrial material handling. Different topologies are reviewed in chapter 2, where the aspect of supply, control and communication was analyzed. A segmented Long-Stator LPMSM with light weight moving part (vehicle) is considered as a good solution to achieve the dynamic demands of such a system. An experimental set-up was build based on a segmented Long-Stator LPMSM forming a closed path (annulus). This experimental machine is a donation from an industrial company. A centralized power supply with a self developed communication system was implemented. The experimental set-up an its characteristics were described in chapter 3.

This segmented long-stator PM linear motor shows some electric properties and force profile which must be considered in the control algorithm. If a smooth force profile is essential along the whole track, then a precise electromagnetic (and mechanic) model will help to achieve it. Chapter 4 describes the electric model of the machine, specially oriented to determine the effect in the force characteristic of iron saturations (current dependent), field harmonics (position dependent) and segment transitions.

A Finite Element Model was build to obtain more information of the motor. With help of the software "Maxwell 2D" magneto-static simulations for 50 positions inside of a pole pitch and 20 currents inside of the rated range oriented in the q-axis were carried out. A total of 7 poles was covered, including the transition between segments. All this information was incorporated as feed-forward (in form of tables) in the control loop. Three main control structures based on classical strategies were adapted to the segmented long stator linear motor, basically oriented to perform a smooth and high dynamic force profile overall the track. During transition between stator segments, the position dependent force is produced by controlling two inverters simultaneously. The average value of the force is kept at its reference value during transition between stator segments using a position and current dependent force F_x^{FEM} obtained by FEM.

The force profile obtained by FEM simulation was validated by a static force measurement. A force transducer from the company “ ME Systeme” was used to obtain an analog voltage proportional to the force. This voltage was sampled by the control PC and stored. In order to measure the force for different positions, the transducer was fixed with a spindle in one point to the frame of the machine, and at the other side to the mover (appendix 0). The measurement was carried out for different positions and current in such a way that it can be compared with the profile obtained by FEM. The comparison shown in Figure 4.10 verifies the shape of the force profile and delivers a deviation of around 7,4% for the force value at rated current. The difference is mainly explained due to the simplifications in the model, especially because iron loses and eddy currents are not considered. Additionally, a trade off between meshing and simulation time must be found to reach an acceptable accuracy of the results. The cogging force measured shows an amplitude of 28N (Figure 4.10b), and the FEM calculation 37N. this difference is highly dependent of the air gap considered in the simulation. The motor has a large cogging force, which reaches 4,2% of the rated thrust force.

A coarse validation of the inductances obtained by FEM is done. Previous works (in the institute) used parameter identification with FEM tools. In this thesis the mathematic procedure and inaccuracies of the FEM method are not discussed in detail.

The main goal of the work was to achieve a smooth and high dynamic force profile overall the track. Three control strategies adapted to segmented long stator linear drives, supported by FEM information, were investigated:

- Field oriented control
- Direct flux control
- Resonant control

Each one of these strategies were designed to control two consecutive segments at the same time (within the same control interrupt task) when a vehicle moves between two segments. The implementation is based on a flexible hardware and software that allows to fulfill such demands. From the hardware side, a proprietary communication protocol was developed and implemented, specially to allow a vehicle controller (Industrial PC) to communicate with two inverters (assigned to a segment of the track) within a time slot of 10 µs. The actual modulation times and the actual currents are interchanged via this bus. The software was implemented in such a way that, depending on the position of the vehicle, the controller is enabled to address up to two inverters within the time slot of 10 µs.

The corresponding control block diagrams for each of the three control strategies were presented in chapter 5.

Three main force disturbances were identified in the model of the machine:

- Non sinusoidal *EMF* distribution, which is a result of the winding distribution and the magnetic field harmonics (produced by the magnet) in the air-gap.
- Cogging force, which is the effect of the attraction of the magnet and teeth.
- Magneto motive force weakening between segments, which appears only in distributed three phase windings. (end of the segment).

All the above mentioned disturbances, were partially (and almost totally) suppressed by injecting appropriate currents.

The control strategies can be classified according information demand (information used from FEM) and performance. **Table V** and Figure 6.1 show a summary of the control strategies analyzed in chapter 5. Current controllers use a voltage model of the motor based on FEM-calculations to reject the disturbances introduced by the non sinusoidal back *EMF*. This means, it needs more information than the other controllers. The direct flux controllers requires less information than the feed forward strategy used by field oriented current control. The force controller (without inner current or flux loop) uses only the force feedback from the FEM. The best performance in force ripple suppression is achieved by the PI+resonant controller, which requires less information of the machine. Necessary condition is the knowledge of the resonance frequency.

As conclusion, a simple resonant element together with only the force profile of the motor, provides the best performance in force ripple suppression.

6.2. Future work

In this thesis, the feasibility of hardware and software to control a Long-Stator LPMSM with a smooth force profile overall the track was demonstrated. Speed and position control were not analyzed, but a necessary condition to achieve a good per-

Table V: Summary of the control methods applied to long stator linear drives.

Control method	FEM information required	Performance
Force-current feed-forward control	$F_x^{FEM}(i_q,x)$, $i_q(F_x,x)$, $\partial\vec{\Psi}_{dq}/\partial x(iq,x)$, $\vec{\Psi}_{dq}(iq,x)$, $L_{dq}^{dif}(i_q,x)$	20 N ripple
PI force-current control	$F_x^{FEM}(i_q,x)$, $\partial\vec{\Psi}_{dq}/\partial x(iq,x)$, $\vec{\Psi}_{dq}(iq,x)$, $L_{dq}^{dif}(i_q,x)$	30 N ripple
Force-flux feed-forward control	$F_x^{FEM}(i_q,x)$, $\Psi_q(F_x,x)$, $\vec{\Psi}_{dq}(iq,x)$	20 N ripple
PI force-flux control	$F_x^{FEM}(i_q,x)$, $\vec{\Psi}_{dq}(iq,x)$	30 N ripple
PI force control	$F_x^{FEM}(i_q,x)$	35 N ripple
PI resonant force control	$F_x^{FEM}(i_q,x)$	6 N ripple

formance for those superimposed control loops, is to have a fast and accurate inner force controller.

As future work, the implementation of a multi vehicle system should be considered, where the demand on hardware and control coordination is predominant. The controller distributed topology described in chapter 2 opens an interesting alternative to avoid the limitation given by the Inverter-Bus. The best hardware combination and complexity of the application will determine the future of Long-Stator LPMSM in applications for material handling. Always a global design of the system will deliver the best result in investment and benefit, but first the technical tools must be developed.

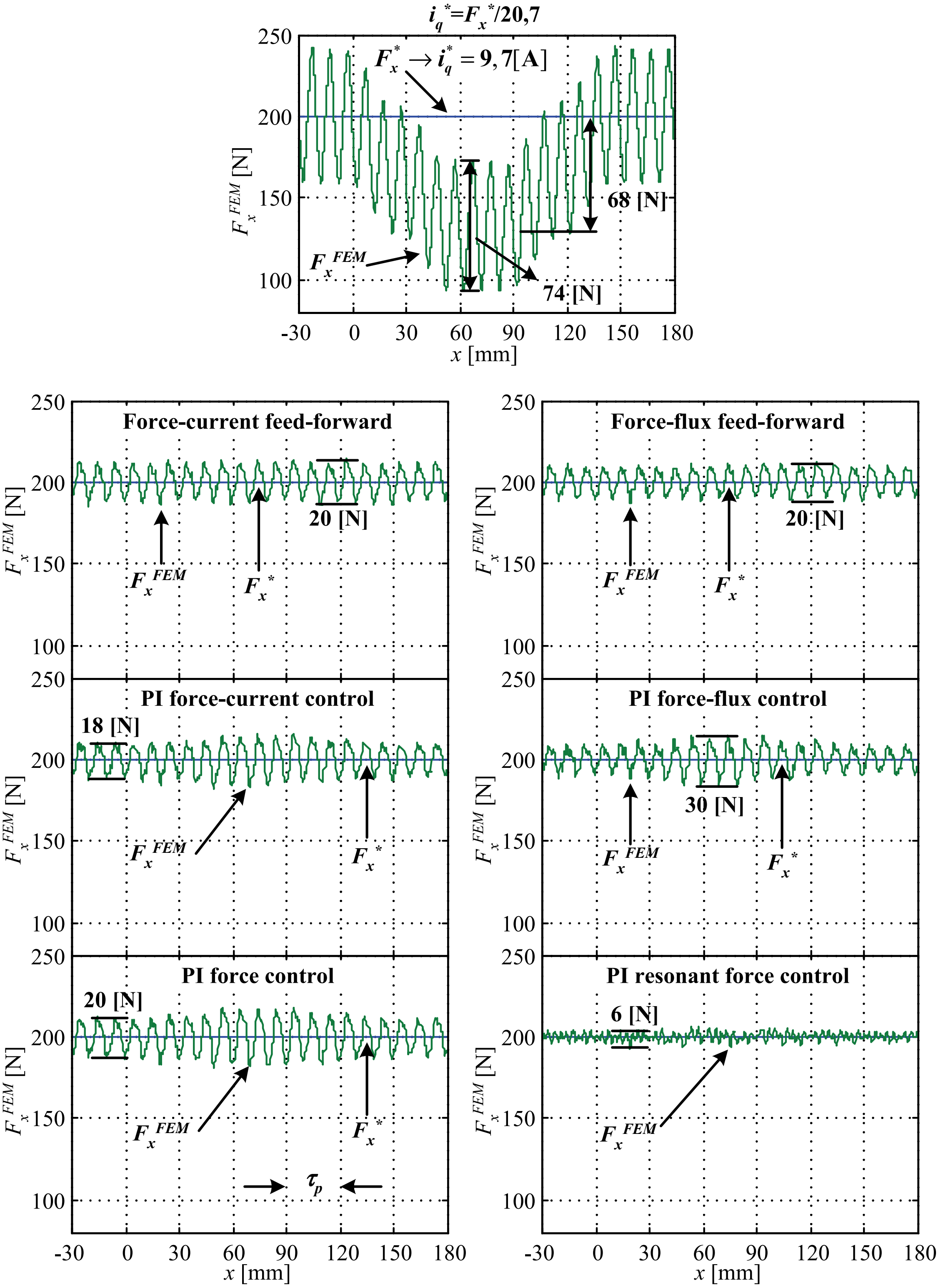

Figure 6.1: Comparison of the control methods for segmented long-stator linear motors. Summary of experimental measurement. Special case for the transition between two segments. All experiments were carried out at constant speed $v = 1.56$ m/s.

Bibliography

[1] Mutschler P., Canders W.-R., Mosebach H., Weigel J., Lamsahel H., Shi Z.; "Neue Funktionalitäten von Linearantrieben"; Forschungsvereinigung Antriebstechnik e.V.; Forschungsheft 692; 2003

[2] Henning U., Kamp P., Hochleitner J.; "Langstator- Synchronmotorantrieb des TRANSRAPID"; eb-Elektrische Bahnen 93; 1995 Heft 7; S.230-235

[3] Hut E.,Canders W.-R., Mosebach H.; "Linear Motor Transfer Technology (LMTT) for Container Terminals", LDIA'98; Tokyo

[4] Studer C., Keyhani A., Sebastian T., Murthy S.K.; "Study Of Cogging Torque in Permanent Magnet Machines"; IEEE Proceedings IAS 1997; New Orleans

[5] Bodika N., Cruise R., Jeans C., Landy C.; "Methods of Detent Force Reduction in Linear Synchronous Motors"; International Conference on Electric Machines and Drives, IEMD '99; May 1999 pp.437-439

[6] Depenbrock M.; "Direkte Selbstregelung (DSR) für hochdynamisch Drehfeldantriebe mit Stromrichterspeisung"; etz Archiv Band 7; 1985

[7] Zhong L., Rahman M.F.; "Analysis of Direct Torque Control in Permanent Magnet Synchronous Motor Drives"; IEEE Transactions on Power Electronics; Vol.12 No.3; May 1997

[8] Weigel J., Mutschler P.; "Modelling and Control of a Permanent Magnet Linear Synchronous Motor featuring Unbalance and Saturation including Cross-Saturation"; Power Electronics Specialists Conference PESC'04; Aachen 2004

[9] Kazmierkowski M.P., Malesani L.; "Special Section on PWM Converter Current Control"; IEEE Transactions on industrial Electronics, Vol.45 No.5; October 1998; pp.689-703

[10] Springob L., Holtz J.; "High-Bandwidth Current Control for Torque-Ripple Compensation in PM Synchronous Machines"; IEEE Transactions on Industrial Electronics, Vol.45 No.5; October 1998; pp.713-721

[11] Weigel, J., Mutschler, P., "Acquisition of a permanent magnet linear synchronous motor's electrical parameters and dead beat current control considering saturation" IEEE Electric Machines and Drives Conference, IEMDC'03., Vol.2 , June 2003, pp.791 –797

[12] Boldea I.; Linear Electromagnetic Actuators and Their Control: a review; EPE-PEMC 2002; 2002;

[13] Schröder D.; "Elektrische Antriebe 2"; Springer-Verlag Berlin Heidelberg New York; 1995; ISBN 3-540-57610-X

[14] Mutschler P.; "Control of Drives"; Vorlesungsskript TU Darmstadt 2007

[15] Llor A.M., Retif J.M., Lin-Shi X., Arnalte S., Allard B.; “Novel Fixed Frequency Direct Torque Control Technique For A Permanent Magnet Synchronous Machine”; EPE 2003, Toulouse

[16] Zolghadri M.R., Diallo D., Roye D.; “Direct Torque Control for Synchronous Machine”; EPE 1997; Toulouse; Volume3 ; pp.694ff.

[17] Matlab user manual: Matlab – The Language of Technical Computing, Version 7 Release 2006b; Mathworks; 2006

[18] Holtz J., Springob L.; “Identification and Compensation Of Torque Ripple in High-Precision Permanent Magnet Motor Drives”; IEEE Transactions on Industrial Electronics, Vol.43, No.2; 1996; pp.309-320

[19] Grčar B. et al; “Pulsating Torque Reduction for Permanent Magnet AC Motors”; Proceedings on the Conference on Control Applications; September 2001 Mexico City; 2001; pp.288-293

[20] Pahlke D.; “Implementierung einer direkten Stromregelung”; Studienarbeit 1283; Institut für Stromrichtertechnik und Antriebsregelung, TU Darmstadt; Januar 2001

[21] Boldea I., Nasar Syed A.; “Linear Electric Actuators and Generators”; Cambridge University Press 1997; ISBN 978-0-521-02032-9

[22] Gieras J., Piech Z.; “Linear Synchronous Motors, Transportation and Automation Systems”; CRC Press LLC 2000; ISBN 0-8493-1859-7

[23] Chevailler S.; “Comparative Study and Selection Criteria of Linear Motors”; Dissertation École Polytechnique Fédérale de Lausanne; 2006

[24] Lorenz R.D., Jansen P.L., Li L.J., Werner B.; “An Integrated Vehicle and Electromagnetic Propulsion Unit for a High-Speed Material Transport System”; Industry Applications Society Annual Meeting, 1992. 4-9 Oct. 1992 pp.1945-1952 vol.2

[25] Duffi N.A., Lorenz R.D., Sanders J.L.; “High performance LIM based material transfer.” Proc. of the NSF Design and Manufacturing Systems Conf., Atlanta, GA, Jan 8-10, 1992, S.1027-1030

[26] Abdou G.H., Sherif S.A.; “Theoretical and Experimental Design of LIM in Automated Manufacturing Systems”; IEEE Transactions on Industry Applications, Vol27, No2, March/April 1991

[27] Sieber B., Breil J.; “New Developments for a Linear Motor System with Multiple Carriers”; The 4th International Symposium on Linear Drives for Industry Applications; 8-10 September2003, Austin Court, Birmingham, UK.; pp.125-128

[28] "MagneTrak®. Paradigmenwechsel im Material-handling. Elektromagnetische Technologie für komplexe Materialflusssysteme", http://www.translift.ch/

[29] Mutschler P.; “Comparison of Topologies for Linear Drives in Industrial Material Handling and Processing Applications”; 7th International Conference on Power Electronics, ICPE 07, Daegu, Korea

[30] Banerjee A.; “Design and Prototype Construction of a Low Cost Inverter Tailored for a Segmented Linear Motor Using Intelligent Power Modules” Master Thesis, Institut für Stromrichtertechnik und Antriebsregelung, TU Darmstadt 2007

[31] Benavides R.; “Entwurf und Realisierung eines RS-485-basierten Multimasterbussystems”; Studienarbeit Nr.: 1307, Institut für Stromrichtertechnik und Antriebsregelung, TU Darmstadt, 2003

[32] Texas Instrument; “The RS-485 design guide” application notes

[33] Siemens; “Simodrive Projectierungsanleitung Umrichter”; Ausgabe 08.02 Vorab 27.08.2002

[34] Racciu G., Mantegazza P.; “RTAI User Manual 3.4”; October 2006; rev 0.3

[35] Mohan N.; “Electric Drives, an Integrative Approach”; MNPERE Minneapolis USA; ISBN 0-9663530-1-3

[36] Schröder D.; “Elektrische Antriebe-Grundlagen”; Zweite Auflage; Springer-Verlag Berlin Heidelberg New York 2000; ISBN 3-540-66846-2

[37] Weigel J.; “Modellbildung und parameteradaptive hoch-dynamische Regelung eines permanenterregten Synchronlinearmotors”; Dissertation TU Darmstadt; 2004

[38] Kost A.; “Numerische Methoden in der Berechnung elektromagnetischer Felder”; Springer-Verlag Berlin Heidelberg New York 1994; ISBN 3-540-55005-4

[39] Leonard W.; “Regelung elektrischer Antriebe”; Springer-Verlag Berlin Heidelberg New York 2000; ISBN 3-540-67179-X

[40] Kazmierkowski M.P., Tunia H.; “Automatic Control of Converter-Fed Drives”; Elsevier Amsterdam-London-New York-Tokyo; Polish Scientific Publishers PWN Ltd. Warszawa 1994

[41] Astrom K.J., Wittenmark B.; “Computer Controlled Systems, Theory and Design”; Second edition; Prentice-Hall, INC. 1990

[42] Geitner G.H.; “Entwurf digitaler Regler für elektrische Antriebe”; VDE-Verlag Berlin und Offenbach 1996; ISBN 3-8007-1847-2

[43] Brahms U.; “Regelung von Lineardirektantrieben für Werkzeugmaschinen”; VDI Fortschrittberichte Nr. 735; VDI Verlag; Düsseldorf 1998

[44] Jahns T. M., Soong W. L.; “Pulsating Torque Minimization Techniques for Permanent Magnet AC Motors Drives-A Review”; IEEE Transactions on Industrial Electronics, Vol. 43, No. 2, April 1996

[45] Tärnhuvud T. M.; “Beitrag zur Lösung des Fehler- und Genauigkeitsproblems der Methode der finiten Elemente für elektromagnetische Felder”; Dissertation ETH Nr.9218; Zürich 1990

[46] Jean-Luc Guermond A. E.; “Theory and Practice of Finite Elements”; Springer-Verlag New York 2004; ISBN 0-387-20574-8

[47] Benavides, R.; Mutschler, P.; “Controlling a system of linear drives”, IEEE 36th Power Electronics Specialist Conference, PESC; June 2005, pages 1587-1593.

[48] Maxwel online help system; Maxwell 2D; Ansoft; http://www.ansoft.com/products/em/maxwell/

[49] Benavides R.; Mutschler P.; “Detent force compensation in Segmented Long Stator Permanent Magnet Linear Drives using Finite Element Models”, 12th European Conference on Power Electronics and Applications, Aalborg, Denmark.

[50] Benavides R.; Mutschler P.; “Compensation of Disturbances in Segmented Long Stator Linear Drives using Finite Element Models”, International Symposium on Industrial Electronics, 9-13 July 2006, Montréal, Canada, Volume 3, page(s): 2445 – 2449.

[51] J. Zeng, X. Guillaud, P. Degobert, “Control of AC machines with Multi-frequency Resonant controller”, the 11th International Power Electronics and Motion Control Conference, Riga, Latvia, Sept. 2004.

[52] Schönfeld R.; “Digitale Regelung elektrischer Antriebe”; Hüthig Buch Verlag Heidelberg 1990; ISBN 3-7785-1904-2

[53] I. Takahashi and T. Noguchi, “A new quick-response and high-efficiency control strategy of an induction motor”, IEEE Trans. Ind. Application, vol. 22, pp. 820-827, Sept/Oct 1986.

[54] T. G. Habetler and F. Profumo, “Direct torque control of induction machines using space vector modulation”, IEEE Trans. Ind. Application, vol. 28, pp. 1045-1052, Sept./Oct. 1992.

[55] P. L. Chapman, S.D. Sudhoff, “Optimal control of permanent-magnet AC machine drives with a novel multiple reference frame estimator/regulator”, IEEE Industry Application Conference, Vol. 4, pp. 2567-2573, Oct. 1999.

[56] Giuseppe S., Kazmierkowski M. P.; “Direct Torque Control of PWM Inverter-Fed AC Motors- A Survey”; IEEE Transaction in Industrial Electronics, Vol. 51; N0. 4; August 2004

[57] J. Oswald, T. Maier, J. Teigelkötter, D. Schmitt, „Direktantriebe mit permanenterregten Synchron-maschinen“ ETG. Elektrisch-mechanische Antriebssysteme, 6. – 7. Oktober 2004, Fulda, Deutschland.

[58] Seok J. K., Kim J. S., Choi J. W., Sul S. K.; “Overmodulation Strategy for high Performance Torque Control”; Power Electronics Specialist Conference 1996; Vol. 2; pp.1549-1554

[59] Y. Sato, T. Ishizuka, K. Nezu, T. Kataoka, “A new control strategy for voltage-type PWM rectifiers to realize zero steady-state control error in input current”, IEEE Trans. Ind. Application, Vol. 34, Issue 3, May-June 1998, pp. 480-486.

[60] D.N. Zmood, D.G. Holmes, G.H. Bode, “Frequency-domain analysis of three-phase linear current regulators”, IEEE Trans. Ind. Application, Vol. 37, pp. 601-610, 2001.

[61] Lenwari W., Sumner M., Zanchetta P., Culea M.; “A High Performance Harmonic Current Control for Shunt Active Filters Based on Resonant Compensators”; IEEE, IECON 2006 - 32nd Annual Conference on Industrial Electronics Nov. 2006 Page(s):2109 – 2114

[62] Zhao F.; "Entwicklung und Erprobung einer Interface-Karte am PCI-Bus für die Datenkommunikation und Echtzeitverarbeitung"; Diplomarbeit Nr. ; Institut für Stromrichtertechnik und Antriebsregelung, TU Darmstadt 2005

[63] ME-Meßsystem GmbH. Force sensor catalog.

http://www.me-systeme.de/de/manuals/cat-200.pdf

Appendix

A.1 Voltage equation transformations

For each phase of the machine, the terminal voltage is described by (80) and (81) in matrix form and vectorial form respectively.

$$\begin{bmatrix} u_a \\ u_b \\ u_c \end{bmatrix} = \begin{bmatrix} R_a & 0 & 0 \\ 0 & R_b & 0 \\ 0 & 0 & R_c \end{bmatrix} \cdot \begin{bmatrix} i_a \\ i_b \\ i_c \end{bmatrix} + \begin{bmatrix} \dfrac{d\Psi_a}{dt} \\ \dfrac{d\Psi_b}{dt} \\ \dfrac{d\Psi_c}{dt} \end{bmatrix} \tag{80}$$

$$\vec{u}_{abc} = \mathbf{R_{abc}} \cdot \vec{i}_{abc} + \frac{d\vec{\Psi}_{abc}}{dt} \tag{81}$$

The linear transformation (82) allows to represent the three phase system in a two-phase stator *α-β-0* coordinate system.

$$\vec{u}_{\alpha\beta 0} = \underbrace{\frac{2}{3} \begin{bmatrix} 1 & -\frac{1}{2} & -\frac{1}{2} \\ 0 & \frac{\sqrt{3}}{2} & -\frac{\sqrt{3}}{2} \\ \frac{1}{2} & \frac{1}{2} & \frac{1}{2} \end{bmatrix}}_{\mathbf{T_{abc}}} \cdot \vec{u}_{abc} \quad \vec{u}_{abc} = \underbrace{\begin{bmatrix} 1 & 0 & 1 \\ -\frac{1}{2} & \frac{\sqrt{3}}{2} & 1 \\ -\frac{1}{2} & -\frac{\sqrt{3}}{2} & 1 \end{bmatrix}}_{\mathbf{T_{abc}^{-1}}} \cdot \vec{u}_{\alpha\beta 0} \tag{82}$$

The star connection of the windings with isolated neutral point allows to eliminate the zero sequence. Additional disturbances, like high frequency common mode currents due to capacitive coupling between the stator windings and the case, are neglected. (82) reduces to (83).

$$\vec{u}_{\alpha\beta} = \underbrace{\frac{2}{3} \begin{bmatrix} 1 & -\frac{1}{2} & -\frac{1}{2} \\ 0 & \frac{\sqrt{3}}{2} & -\frac{\sqrt{3}}{2} \end{bmatrix}}_{\mathbf{T_{abc}}} \cdot \vec{u}_{abc} \qquad \vec{u}_{abc} = \underbrace{\begin{bmatrix} 1 & 0 \\ -\frac{1}{2} & \frac{\sqrt{3}}{2} \\ -\frac{1}{2} & -\frac{\sqrt{3}}{2} \end{bmatrix}}_{\mathbf{T_{abc}^{-1}}} \cdot \vec{u}_{\alpha\beta} \tag{83}$$

(83) transforms (81) in (84)

$$\vec{u}_{\alpha\beta} = \underbrace{\mathbf{T_{abc}} \cdot \mathbf{R_{abc}} \cdot \mathbf{T_{abc}^{-1}}}_{\mathbf{R_{\alpha\beta}}} \cdot \vec{i}_{\alpha\beta} + \mathbf{T_{abc}} \cdot \frac{d\left(\mathbf{T_{abc}^{-1}} \cdot \vec{\Psi}_{\alpha\beta}\right)}{dt}$$

$$\vec{u}_{\alpha\beta} = \mathbf{R_{\alpha\beta}} \cdot \vec{i}_{\alpha\beta} + \frac{d\vec{\Psi}_{\alpha\beta}}{dt} \tag{84}$$

$$\mathbf{R_{\alpha\beta}} = \begin{bmatrix} \frac{1}{3}\left(2R_a + \frac{1}{2}\left(R_b + R_c\right)\right) & \frac{1}{2\sqrt{3}}\left(R_c - R_b\right) \\ \frac{1}{2\sqrt{3}}\left(R_c - R_b\right) & \frac{1}{2}\left(R_b + R_c\right) \end{bmatrix} \tag{85}$$

The introduction of the rotative *d-q* coordinate system (86) transform (84) to (88).

$$\vec{u}_{dq} = \begin{bmatrix} u_d \\ u_q \end{bmatrix} = \underbrace{\begin{bmatrix} \cos(\theta) & \sin(\theta) \\ -\sin(\theta) & \cos(\theta) \end{bmatrix}}_{\mathbf{T_{dq}}} \cdot \vec{u}_{\alpha\beta} \quad \vec{u}_{\alpha\beta} = \underbrace{\begin{bmatrix} \cos(\theta) & -\sin(\theta) \\ \sin(\theta) & \cos(\theta) \end{bmatrix}}_{\mathbf{T_{dq}^{-1}}} \cdot \vec{u}_{dq} \tag{86}$$

with $\theta = \frac{\pi}{\tau_p} \cdot x$, and τ_p the pole pitch of the linear motor.

$$\vec{u}_{dq} = \underbrace{\mathbf{T_{dq}} \cdot \mathbf{R_{\alpha\beta}} \cdot \mathbf{T_{dq}^{-1}}}_{\mathbf{R_{dq}}} \cdot \vec{i}_{dq} + \mathbf{T_{dq}} \cdot \frac{d\left(\mathbf{T_{dq}^{-1}} \cdot \vec{\Psi}_{dq}\right)}{dt}$$

$$\vec{u}_{dq} = \mathbf{R_{dq}} \cdot \vec{i}_{dq} + \mathbf{T_{dq}} \cdot \left(\frac{d\mathbf{T_{dq}^{-1}}}{dt} \cdot \vec{\Psi}_{dq} + \mathbf{T_{dq}^{-1}} \cdot \frac{d\vec{\Psi}_{dq}}{dt} \right) \tag{87}$$

$$\vec{u}_{dq} = \mathbf{R_{dq}} \cdot \vec{i}_{dq} + \frac{d\vec{\Psi}_{dq}}{dt} + \mathbf{T_{dq}} \cdot \frac{\partial \mathbf{T_{dq}^{-1}}}{\partial x} \cdot \frac{\pi}{\tau_p} \cdot \frac{dx}{dt} \cdot \vec{\Psi}_{dq}$$

$$\vec{u}_{dq} = \mathbf{R_{dq}} \cdot \vec{i}_{dq} + \frac{d\vec{\Psi}_{dq}}{dt} + \frac{\pi}{\tau_p} \cdot \begin{bmatrix} 0 & -1 \\ 1 & 0 \end{bmatrix} \cdot \vec{\Psi}_{dq} \cdot \frac{dx}{dt} \tag{88}$$

The linked flux vector $\vec{\Psi}_{dq}$ is a function of $\vec{i}_{dq}$ and *x*. Then, the derivative can be rewritten as in (89).

$$\frac{d\vec{\Psi}_{dq}}{dt} = \frac{\partial \vec{\Psi}_{dq}}{\partial \vec{i}_{dq}} \cdot \frac{d\vec{i}_{dq}}{dt} + \frac{\partial \vec{\Psi}_{dq}}{\partial x} \cdot \frac{dx}{dt}$$

$$\text{With } \frac{\partial \vec{\Psi}_{dq}}{\partial \vec{i}_{dq}} = \begin{bmatrix} \frac{\partial \Psi_d}{\partial i_d} & \frac{\partial \Psi_d}{\partial i_q} \\ \frac{\partial \Psi_q}{\partial i_d} & \frac{\partial \Psi_q}{\partial i_q} \end{bmatrix} = \mathbf{L_{dq}^{diff}} \tag{89}$$

Introducing (89) in (88), the voltage equation of the motor is rewritten as in (90).

$$\vec{u}_{dq} = \mathbf{R_{dq}} \cdot \vec{i}_{dq} + \mathbf{L_{dq}^{diff}} \cdot \frac{d\vec{i}_{dq}}{dt} + \underbrace{\left(\frac{\partial \vec{\Psi}_{dq}}{\partial x} + \frac{\pi}{\tau_p} \cdot \begin{bmatrix} -\Psi_q \\ \Psi_d \end{bmatrix} \right) \cdot \frac{dx}{dt}}_{EMF} \tag{90}$$

A.2 Linked flux equation transformation

The flux linkage $\vec{\Psi}_{\alpha\beta}$ is a function of the currents i_α, i_β, and the position x (91).

$$\vec{\Psi}_{\alpha\beta} = \mathbf{L_{\alpha\beta}}(\vec{i}_{\alpha\beta}, x) \cdot \vec{i}_{\alpha\beta} + \vec{\Psi}_{\alpha\beta PM}(x) = \begin{bmatrix} L_{\alpha\alpha} & L_{\alpha\beta} \\ L_{\beta\alpha} & L_{\beta\beta} \end{bmatrix} \cdot \begin{bmatrix} i_\alpha \\ i_\beta \end{bmatrix} + \begin{bmatrix} \Psi_{\alpha PM} \\ \Psi_{\beta PM} \end{bmatrix} \tag{91}$$

The inductance matrix $\mathbf{L_{\alpha\beta}}$ depends on saturation and is a function of the current and the position. The flux linkage $\vec{\Psi}_{\alpha\beta PM}(x)$ represents the flux produced by the magnets. Applying transformation (82) in (91), we get (92).

$$\begin{aligned} \vec{\Psi}_{dq} &= \underbrace{\mathbf{T_{dq}} \cdot \mathbf{L_{\alpha\beta}} \cdot \mathbf{T_{dq}^{-1}}}_{\mathbf{L_{dq}}} \cdot \vec{i}_{dq} + \mathbf{T_{dq}} \cdot \mathbf{T_{dq}^{-1}} \cdot \vec{\Psi}_{dqPM}(x) \\ \vec{\Psi}_{dq} &= \mathbf{L_{dq}} \cdot \vec{i}_{dq} + \vec{\Psi}_{dqPM}(x) \end{aligned} \tag{92}$$

The linked flux vector $\vec{\Psi}_{dq}$ is a function of $\vec{i}_{dq}$ and x. Then, the derivative can be rewritten as in (89). The firs term of (89) is expand in (93)

$$\frac{\partial \vec{\Psi}_{dq}}{\partial \vec{i}_{dq}} = \begin{bmatrix} \dfrac{\partial \Psi_d}{\partial i_d} & \dfrac{\partial \Psi_d}{\partial i_q} \\ \dfrac{\partial \Psi_q}{\partial i_d} & \dfrac{\partial \Psi_q}{\partial i_q} \end{bmatrix} = \mathbf{L_{dq}^{diff}} \tag{93}$$

$$\begin{aligned} \Psi_d &= L_{dd} \cdot i_d + L_{dq} \cdot i_q + \Psi_{dPM} \\ \Psi_q &= L_{qd} \cdot i_d + L_{qq} \cdot i_q + \Psi_{qPM} \end{aligned} \tag{94}$$

$$\begin{aligned} \frac{\partial \Psi_d}{\partial i_d} &= \frac{\partial L_{dd}}{\partial i_d} \cdot i_d + L_{dd} + \frac{\partial L_{dq}}{\partial i_d} \cdot i_q \\ \frac{\partial \Psi_d}{\partial i_q} &= \frac{\partial L_{dd}}{\partial i_q} \cdot i_d + L_{dq} + \frac{\partial L_{dq}}{\partial i_q} \cdot i_q \\ \frac{\partial \Psi_q}{\partial i_q} &= \frac{\partial L_{qd}}{\partial i_d} \cdot i_d + L_{qd} + \frac{\partial L_{qq}}{\partial i_d} \cdot i_q \\ \frac{\partial \Psi_q}{\partial i_q} &= \frac{\partial L_{qd}}{\partial i_q} \cdot i_d + L_{qq} + \frac{\partial L_{qq}}{\partial i_q} \cdot i_q \end{aligned} \tag{95}$$

Introducing (95) in (93), the differential inductances are defined in terms of the inductances and currents.

$$\frac{\partial\vec{\Psi}_{dq}}{\partial\vec{i}_{dq}}=\begin{bmatrix}\frac{\partial\Psi_d}{\partial i_d} & \frac{\partial\Psi_d}{\partial i_q}\\ \frac{\partial\Psi_q}{\partial i_d} & \frac{\partial\Psi_q}{\partial i_q}\end{bmatrix}=\begin{bmatrix}\frac{\partial L_{dd}}{\partial i_d}\cdot i_d+\frac{\partial L_{dq}}{\partial i_d}\cdot i_q & \frac{\partial L_{dd}}{\partial i_q}\cdot i_d+\frac{\partial L_{dq}}{\partial i_q}\cdot i_q\\ \frac{\partial L_{qd}}{\partial i_d}\cdot i_d+\frac{\partial L_{qq}}{\partial i_d}\cdot i_q & \frac{\partial L_{qd}}{\partial i_q}\cdot i_d+\frac{\partial L_{qq}}{\partial i_q}\cdot i_q\end{bmatrix}+\begin{bmatrix}L_{dd} & L_{dq}\\ L_{qd} & L_{qq}\end{bmatrix} \tag{96}$$

$$\frac{\partial\vec{\Psi}_{dq}}{\partial\vec{i}_{dq}}=\begin{bmatrix}\frac{\partial L_{dd}}{\partial i_d}\cdot i_d & \frac{\partial L_{dd}}{\partial i_q}\cdot i_d\\ \frac{\partial L_{qd}}{\partial i_d}\cdot i_d & \frac{\partial L_{qd}}{\partial i_q}\cdot i_d\end{bmatrix}+\begin{bmatrix}\frac{\partial L_{dq}}{\partial i_d}\cdot i_q & \frac{\partial L_{dq}}{\partial i_q}\cdot i_q\\ \frac{\partial L_{qq}}{\partial i_d}\cdot i_q & \frac{\partial L_{qq}}{\partial i_q}\cdot i_q\end{bmatrix}+\begin{bmatrix}L_{dd} & L_{dq}\\ L_{qd} & L_{qq}\end{bmatrix}=\mathbf{L}_{\mathbf{dq}}^{\mathbf{diff}} \tag{97}$$

A.3 Angle synchronisation

In the experimental set-up the position measurement is done using an incremental encoder, attached to the load machine. The incremental encoder generates 2048 periods of sine and cosine signals per turn, and also one reference pulse per turn. Interpolation based on the arc-tangent evaluation of the sine / cosine- signals with 12-bit AD-converters is used to increase the resolution. But there is a lot of elasticity and backlash between the rotary encoder of the load machine and the vehicle, which strongly reduces the quality of the position and speed measurement. A separate encoder board connected to the ISA bus in the PC is used to evaluate the sine and cosine signals. The evaluation of the position is triggered by the control interrupt.

The encoder board has a free A/D input channel for multipurpose measurement. The induced voltage of the phase *a*, previous signal adaptation, is connected to the A/D channel and sampled together with the position. Figure A3.1 shows the measurement of the normalized induced voltage of phase *a* e_a/v, in which the linear motor is moved at constant speed $v = 1.56$ m/s by the load machine.

The electrical angle β_m is synchronized in such a way that the induced voltage of phase *a* has a zero crossing from positive to negative at $\beta_m = 0°$. From Figure A3.1 can be clearly observed that the position *x* is synchronized to $x = 0$ mm one pole before the magnet carrier enters the segment.

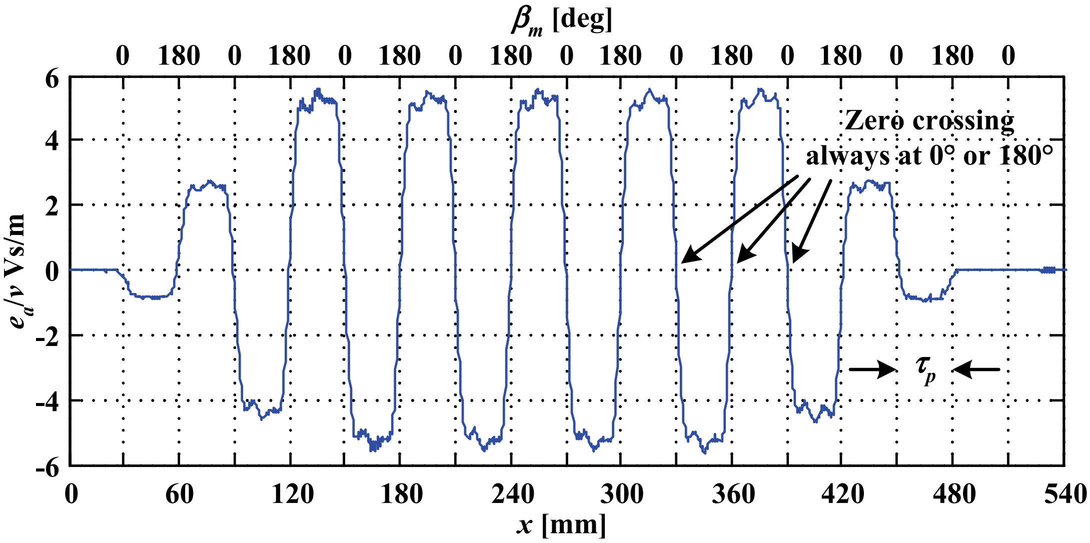

Figure A3.1: Induced voltage measurement of the phase *a*, synchronized with the position measurement.

A.4 Amplitude Optimum in the current loop

The amplitude optimum criteria aims to keep the unity gain of the closed loop for a wide range of frequencies.

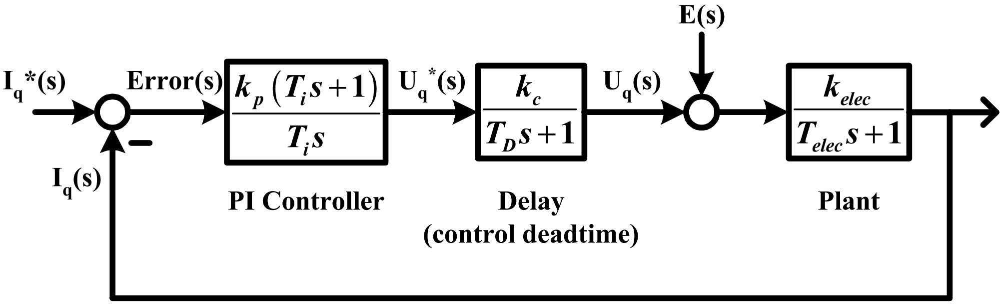

Figure A4.1: Simplified current control loop

In the particular case of the current loop of a motor (Figure A4.1), the zero of the controller is adjusted to cancel the electric pole, i.e. $T_i = T_{elec}$. The open loop transfer function is given by (98) and the closed loop by (99).

$$L_o(s) = \frac{k_p k_c k_{elec}}{T_{elec} s (T_D s + 1)} \tag{98}$$

$$L_c(s) = \frac{L_o}{1 + L_o} = \frac{k_p k_c k_{elec}}{T_D T_{elec} s^2 + T_{elec} s + k_p k_c k_{elec}} \tag{99}$$

A second order lag element reaches its maximum bandwidth at the critical damping, i.e. when the poles are at 45° from the origin. The critical damping in (100) is given by $d=1/\sqrt{2}$.

$$pT2=\frac{1}{\frac{1}{\omega^2}s^2+\frac{2d}{\omega}s+1} \tag{100}$$

(99) and (100) produces two equations with two variables, ω and k_p.

$$\frac{1}{\omega^2}=\frac{T_D T_{elec}}{k_p k_c k_{elec}} \tag{101}$$

$$\frac{\sqrt{2}}{\omega}=\frac{T_{elec}}{k_p k_c k_{elec}} \tag{102}$$

Solving the equation system (101) and (102), ω and k_p are obtained.

$$k_p=\frac{T_{elec}}{2k_c k_{elec} T_D} \tag{103}$$

$$\omega=\frac{1}{\sqrt{2}T_D} \tag{104}$$

with $T_{elec}=L/R$ and $k_{elec}=1/R$ reduces k_p to (103).

$$k_p=\frac{L}{2k_c T_D} \tag{105}$$

Applying k_p into $L_c(s)$ (99) we obtain the closed loop transfer function (104). The equivalent first order lag element has a time constant $T_{eq}=2T_D$.

$$L_c(s)=\frac{1}{2T_D^2 s^2+2T_D s+1}\approx\frac{1}{T_{eq}s+1} \tag{106}$$

The cutoff frequency of the loop is given by ω.

A.5 Amplitude Optimum criteria applied to the force loop

The PI force controller is tuned considering the inner current control loop as a first order lag element with an equivalent time constant T_{eq} (106). The force control loop can be strongly simplified as shown in Figure A5.1. Again, the amplitude optimum (AO) is used to tune the controller parameters k_p and T_i. The open loop transfer function is given by (107) and the closed loop by (108)

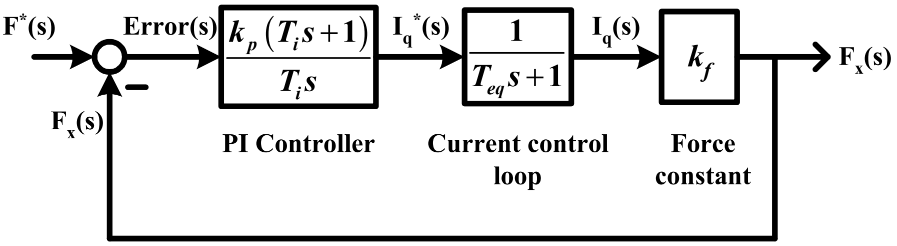

Figure A5.1: Simplified thrust force control loop.

$$L_o(s) = \frac{k_p k_f (T_i s + 1)}{T_i s (T_{eq} s + 1)} \tag{107}$$

$$L_c(s) = \frac{L_o}{1 + L_o} = \frac{k_p k_f}{T_i T_{eq} s^2 + (1 + k_p k_f) T_i s + k_p k_f} \tag{108}$$

Considering the critical damping from a second order system, two equations for the parameters are derived, (109) and (110) (previous appendix).

$$\frac{1}{\omega^2} = \frac{T_i T_{eq}}{k_p k_f} \tag{109}$$

$$\frac{\sqrt{2}}{\omega} = \frac{(1 + k_p k_f) T_i}{k_p k_f} \tag{110}$$

Solving the equation system (109) and (110) T_i and k_p are obtained as function of the frequency ω. ω is the cutoff frequency of the transfer function (108).

$$T_i = \frac{\sqrt{2} \cdot T_{eq} \omega - 1}{T_{eq} \omega^2} \tag{111}$$

$$k_p = \frac{\sqrt{2} \cdot T_{eq} \omega - 1}{k_f} \tag{112}$$

A.6 Double-ratios tuning method

The “double-ratios” tuning method is a more general approach to determine the control parameters. For a *n*-order linear control loop, the transfer function (113) is given.

$$H(s) = \frac{1}{D(s)} = \frac{1}{a_0 + a_1 s + a_2 s^2 + \cdots + a_n s^n} \tag{113}$$

The denominator of H(s) results from the homogeneous differential equation of the system. Hence it is responsible of the damping. From the denominator the coefficient ratios r_i are defined as in (114).

$$r_i = \frac{a_i}{a_{i-1}} \qquad i\text{=1,……,n} \tag{114}$$

The first and last ratio have special characteristics given by (115) and (116).

$$r_1 = \frac{a_1}{a_0} = T_{eq} \qquad \text{i.e. } H(s) \approx \frac{1}{T_{eq}s+1} \tag{115}$$

$$r_n = \frac{a_n}{a_{n-1}} = T_{sys} \tag{116}$$

From the coefficient ratios, the double ratios are defined as in (117)

$$D_i = \frac{r_i}{r_{i-1}} = \frac{a_i a_{i-2}}{a_{i-1}^2} \tag{117}$$

The optimal damping characteristic is achieved when all D_i's are 0,5. With this condition is possible to determine the controller parameters.

A.7 Ampere's law

The equation that the magnetostatic field solver computes (122) is derived from Ampere's law, which is:

$$\nabla \times \vec{H} = \vec{J} \tag{118}$$

Since H is given by (119), (118) is rewritten as in (120).

$$\vec{H} = \frac{\vec{B}}{\mu_r \mu_0} \tag{119}$$

$$\nabla \times \left(\frac{\vec{B}}{\mu_r \mu_0} \right) = \vec{J} \tag{120}$$

From the definition of the magnetic vector potential in (121) is obtained (122).

$$\vec{B} = \nabla \times \vec{A} \tag{121}$$

$$\nabla \times \left(\frac{1}{\mu_r \mu_0} \nabla \times \vec{A} \right) = \vec{J} \tag{122}$$

In a 2-D field simulation, both $\vec{J}$ and $\vec{A}$ are vectors. However, $\vec{J}$ is assumed to only have a *z*-component. A consequence of this is that $\vec{A}$ only has a *z*-component as well. This can be demonstrated starting from $\vec{A}(x,y) = \left(0,0,A_z(x,y)\right)$ and introducing it in (121). Then, the magnetic field density $\vec{B}$ is calculated (123)(124).

$$\vec{B} = \nabla \times \vec{A} = \left(\frac{\partial}{\partial x}, \frac{\partial}{\partial y}, \frac{\partial}{\partial z} \right) \times \left(0,0,A_z(x,y)\right) = \begin{vmatrix} \hat{x} & \hat{y} & \hat{z} \\ \frac{\partial}{\partial x} & \frac{\partial}{\partial y} & \frac{\partial}{\partial z} \\ 0 & 0 & A_z(x,y) \end{vmatrix} \tag{123}$$

$$\vec{B} = \left(\frac{\partial A_z(x,y)}{\partial y}, -\frac{\partial A_z(x,y)}{\partial x}, 0 \right) \tag{124}$$

With (124) in (119) the magnetic field $\vec{H}$ is obtained (125). Then, the current density field $\vec{J}$ is calculated from (118).

$$\vec{H} = \frac{1}{\mu_r \mu_0} \left(\frac{\partial A_z(x,y)}{\partial y}, -\frac{\partial A_z(x,y)}{\partial x}, 0 \right) \tag{125}$$

$$\vec{J} = \nabla \times \vec{H} = \frac{1}{\mu_r \mu_0} \left(\frac{\partial}{\partial x}, \frac{\partial}{\partial y}, \frac{\partial}{\partial z} \right) \times \left(\frac{\partial A_z(x,y)}{\partial y}, -\frac{\partial A_z(x,y)}{\partial x}, 0 \right) \tag{126}$$

$$\vec{J} = \frac{1}{\mu_r \mu_0} \begin{vmatrix} x & y & z \\ \frac{\partial}{\partial x} & \frac{\partial}{\partial y} & \frac{\partial}{\partial z} \\ \frac{\partial A_z(x,y)}{\partial y} & -\frac{\partial A_z(x,y)}{\partial x} & 0 \end{vmatrix} = \frac{1}{\mu_r \mu_0} \left(0, 0, -\frac{\partial^2 A_z(x,y)}{\partial x^2} - \frac{\partial^2 A_z(x,y)}{\partial y^2} \right) \tag{127}$$

In (127), the current density field $\vec{J}$ has only a *z*-component.

A.8 Force sensor

The static force measurement of the motor was done using the force sensor KD40s (S form) from the company ME-Meßsysteme. The sensor is dimensioned to cover a range of ±1000N. The amplifier GSV-1A with a bandwidth of 2.5 kHz (ME-Meßsysteme) is used to preprocess the analog signal of the sensor and connect to the PC. The sampling of the signal is done in the encoder board. Technical specifications are in [63]. The force sensor was fixed with a spindle in one point at the frame of the machine, and at the other side at the mover. This allows to make measurements for different positions of the vehicle. Figure A8.1 shows the experimental set-up, specially the mounting of the force sensor.

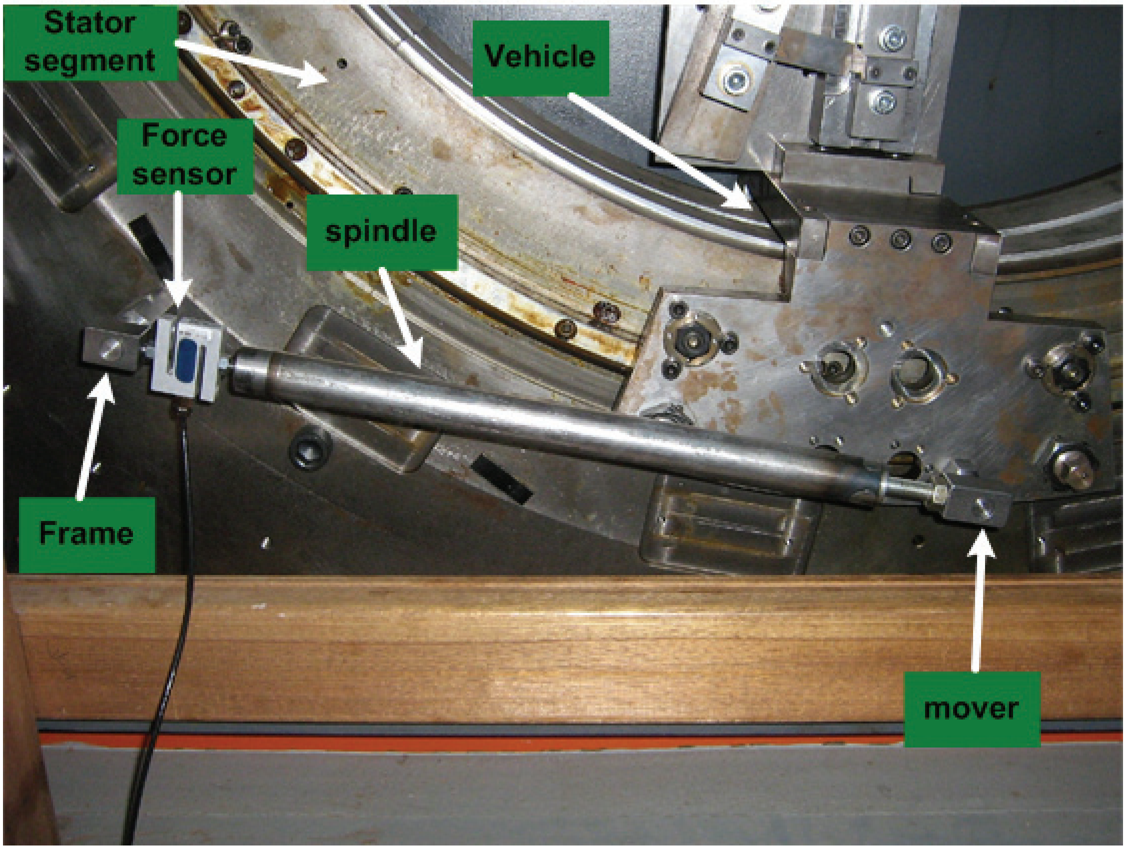

Figure A8.1: Force sensor.

Curriculum Vitae

Rodrigo Benavides Oswald

Born in Osorno, Chile, 24.11.1975

Married

Since 2003	Working as assistant and PhD project at the Department of Power Electronics and Control of drives, Darmstadt University of Technology, Germany.
2000 – 2002	Assistant at the Department of electronics, Power electronic group, Universidad Técnica Federico Santa María, Chile.
1994 – 1999	Study of Electronic Engineering at Universidad Técnica Federico Santa María, Chile.
1990 – 1993	High school Colegio San Mateo, Osorno, Chile.